Structural Optimisation of Diffusion-Driven Degradation Processes

Dissertation

Navina Waschinsky

Structural Optimisation of Diffusion-Driven Degradation Processes

von der Fakultät Architektur und Bauingenieurwesen
der Technischen Universität Dortmund
zur Verleihung des akademischen Grades
Doktor-Ingenieur (Dr.-Ing.)
genehmigte Dissertation

von
Navina Waschinsky

Dortmund, Juni 2021

Kontakt

M. Sc. Navina Waschinsky
Lehrstuhl Statik und Dynamik
Fakultät Architektur und Bauingenieurwesen
Technische Universität Dortmund
August-Schmidt-Str. 8, D-44227 Dortmund
Email: navina.waschinsky@tu-dortmund.de

Prüfungskommission

Vorsitz:	Prof. Dr.-Ing. Ingo Münch
1. Gutachter:	Prof. Dr.-Ing. habil. Franz-Joseph Barthold
2. Gutachter:	Prof. Dr.-Ing. habil. Andreas Menzel

Tag der Einreichung:	08.04.2021
Tag der mündlichen Prüfung:	16.06.2021

Vorwort

Die vorliegende Arbeit entstand während meiner wissenschaftlichen Tätigkeit am Lehrstuhl Statik und Dynamik der Fakultät Architektur und Bauingenieurwesen der Technischen Universität Dortmund.

An dieser Stelle möchte ich allen beteiligten Personen meinen großen Dank für die Unterstützung bei der Anfertigung meiner Dissertation aussprechen.

Mein ganz besonderer Dank gilt meinem Doktorvater Professor Franz-Joseph Barthold für die ausgezeichnete Betreuung, enorme Unterstützung und Möglichkeit zur Umsetzung meiner Dissertation. Insbesondere der regelmäßige Austausch auf fachlicher und persönlicher Ebene war eine große Hilfe und Motivation. Ein weiterer Dank richtet sich an Professor Andreas Menzel für die Übernahme des Zweitgutachtens, die inspirierenden Diskussionen sowie die wissenschaftliche Betreuung.

Außerdem möchte ich mich bei allen ehemaligen und derzeitigen Kollegen für ihre Unterstützung und regen Austausch bedanken. Vielen Dank für die freundschaftliche Arbeitsatmosphäre und den Rückhalt auch in schwierigen Zeiten. Weiterhin möchte ich mich bei Professor Tim Ricken für die Inspiration zu Beginn meiner wissenschaftlichen Tätigkeit bedanken.

Meiner Familie und meinen Freunden möchte ich ganz besonders herzlich danken für die vielseitige und liebevolle Unterstützung, Ermutigung sowie Motivation. Danke für den großen Rückhalt in jeglichen Lebenslagen.

Dortmund, Juni 2021 Navina Waschinsky

Kurzfassung

Im Bereich des konstruktiven Ingenieurbaus werden Bauwerke entwickelt und berechnet. Dabei werden die aus mechanischen Lasten resultierenden Spannungen und Verformungen ermittelt und die Tragwerke dimensioniert, um die Tragfähigkeit, Gebrauchstauglichkeit und Dauerhaftigkeit gemäß internationaler Normen zu gewährleisten. Die Anwendung der Strukturoptimierung ermöglicht die Erstellung von effizienten und ökonomischen Bauwerksentwürfen, welche maximal zulässige Spannungen ausschöpfen können. Allerdings werden bei genormten Berechnungen Umwelteinflüsse, wie zum Beispiel ein chemischer Angriff, nur über sogenannte Expositionsklassen und daraus resultierenden Tragfähigkeitsgrenzen berücksichtigt. Detaillierte Berechnungen zum Einfluss der Spannungen und Verformungen der Bauteile werden häufig vernachlässigt. Insbesondere können zum Beispiel die aus der Optimierung resultierenden ausgeschöpften Spannungsrestriktionen überschritten werden.

Diese Arbeit stellt ein numerisches Programm vor, welches eine effiziente Optimierung mechanischer Strukturen ermöglicht, die aufgrund diffuser Konzentrationen zusätzlich von Degradationsprozessen belastet sind. Dafür wird ein mechanisch-chemisch-degradations gekoppeltes Modell entwickelt. Im Rahmen der klassischen Strukturmechanik ist das entwickelte Materialverhalten unter Berücksichtigung von modifizierten physikalischen Grundlagen der Kontinuumsmechanik zur Beschreibung von mechanisch-chemisch-degradations gekoppelte Prozessen vorgestellt. Mithilfe der Grundlagen der Finiten Elemente Methode (FEM) ist die Lösung des nichtlinearen Problems detailliert ausgearbeitet. Weiterhin ist die entwickelte Strukturanalyse in einem mathematischen Algorithmus einer gradientenbasierten Strukturoptimierung eingebettet. Die Optimierung ermöglicht eine tiefergehende Analyse und Reduktion der schädlichen Auswirkungen infolge von Einflüssen aus einwirkenden chemischen Konzentrationen. Die Anwendung eines variationellen Zugangs zur Strukturoptimierung liefert die gleichzeitige Integration einer analytisch aufbereiteten Sensitivitätsanalyse mit der Strukturanalyse zur Einbettung der kontinuumsmechanischen Formulierungen. Damit ist eine effiziente Strukturoptimierung des eingeführten mechanisch-chemisch-degradations Modells umfassend dargestellt, die numerische Umsetzung mit den benötigten Ableitungen sowie Diskretisierungen dokumentiert und in einem computerbasierten Modell umgesetzt.

Abstract

In the field of structural engineering, structures are developed and calculated. The stresses and deformations resulting from mechanical loads are determined, and the structures are dimensioned to ensure load-bearing capacity, usability and durability in accordance with standards. The application of structural optimisation algorithms enables the development of more efficient and economical building structures, whereby maximum permissible stresses can be exhausted. However, standardised calculations take environmental influences, such as chemical impact, only via so-called exposure classes and resulting material properties into account. Detailed calculations on the influence of stresses and deformations of the structures, especially due to the long-term chemical influence and resulting material degradation, are often neglected. For example, specific stress constraints may be exceeded.

Within the scope of the present work, a numerical programme is developed, enabling an efficient optimisation of mechanical structures that are additionally burdened by degradation processes due to diffusive concentrations. For this purpose, a mechanical-chemical-degradation coupled model is developed. Within the framework of classical structural mechanics, the developed material behaviour is presented, taking into account modified physical principles of continuum mechanics to describe a mechanical-chemical-degradation coupled processes. With the help of the fundamentals of the Finite Element Method (FEM), the solution of the non-linear problem is outlined in detail. Furthermore, the developed structural analysis is embedded in a mathematical algorithm of gradient-based structural optimisation. The optimisation allows a deeper analysis and reduction of the harmful effects due to the influence of acting chemical concentrations. A variational approach to structural optimisation provides the simultaneous integration of analytically prepared sensitivity analysis with the structural analysis for embedding the continuum mechanical formulations. Thus, efficient structural optimisation of the introduced mechanical-chemical-degradation model is comprehensively presented. The mathematical model with the required derivations as well as discretisation is documented and implemented in a computer-based model.

Contents

Nomenclature

This section provides an overview of frequently used abbreviations. The references to the listed abbreviations are noted in the respective sections.

Abbreviations for Latin expressions

cf.	*confer*	compare
e.g.	*exempli gratia*	for example
i.e.	*id est*	that is
et al.	*et alii*	and others
vs.	*versus*	against

Abbreviations within the continuum model and optimisation framework

CAGD	Computer-Aided Geometric Design
FE	Finite Element
FEM	Finite Element Method
FEA	Finite Element Analysis
KKT	Karush–Kuhn–Tucker
SQP	Sequential Quadratic Programming
BFGS	Broyden-Fletcher-Goldfarb-Shanno
FDM	Finite Difference Method

Abbreviations within the mathematical solver

n_s	number of design parameters
n_m	number of material parameters
m_h	number of equality constraints
m_g	number of inequality constraints
m_j	number of objective functions

Abbreviations within the numerical investigations

nel	total number of elements
nn	number of nodes per element
edof	number of degrees of freedom per element
dof	global number of degrees of freedom
dofm	global number of mechanical degrees of freedom
dofc	global number of chemical degrees of freedom
dofs	global number of design parameters
dofp	global number of material parameters

1. Introduction

In this section, the motivation for this thesis is highlighted, and the objectives are presented. An overview of the sections, respectively, the outline of this work, serves as an orientation for the reader.

1.1. Motivation

In this thesis, an optimisation algorithm is presented, which contributes to preventing premature failure, damage to building structures and the strengthening of durability. The focus lies on structures contaminated by chemical substances, having strong destructive effects on the material. A mathematical algorithm is developed to optimise a structure exposed to chemical influences and assure the static load capacity. Therefore, a coupled mechanical-chemical-degradation approach is embedded in a Finite Element (FE) framework. A time-efficient optimisation algorithm is developed to provide a helpful simulation tool that reduces long-term material degradation.

Engineering structures are dimensioned according to standards. The maximum existing stresses are evaluated and the material load-bearing capacity is examined, whereby environmental influences are only marginally considered. However, negative influences can also change the material composition and the mechanical load-bearing capacity over time. Most changes in the internal structure of materials are associated with diffusion processes. Examples in civil engineering where diffusion-driven degradation processes occur are, among others, the long-term effect of calcium leaching into concrete. Whereby „pure water generates concentration gradients, which lead to the diffusion of Ca-ions from the pore water and the subsequent degradation of the underground concrete“ [32]. Alternatively, the sulfuric acid attack, where „degradation is dominated by the diffusion rate of the acid“ [143]. Moreover, a numerical method model for simulating cementitious materials' degradation under external sulphate attack is presented in [116]. The focus is on providing a holistic model to describe the degradation process, considering ionic diffusion, chemical equilibrium and the influence on the change of mechanical properties. Further details are discussed in [117] and the usefulness of sensitivity analysis for the detection of damaging factors in the context of sulphate attack and calcium leaching is presented. The focus is on providing a holistic model to describe the degradation process, taking into account ionic diffusion, chemical equilibrium and the influences on changes in mechanical properties. However, the model cannot produce a spatial resolution of complex structures, which is of particular interest for the concentrations' spatial dispersion. Diffusion-driven degradation processes can occur under different conditions, yet the general assumptions are similar. Thus, structure degradation with associated changes in material properties and the coupling of the chemical reaction and transport mechanisms must be addressed. For this reason, this work presents a spatially and temporally resolved FE-model that can be applied to various field applications so that environmental influences can be considered.

An essential point in civil engineering is the optimisation of load-bearing structures to achieve maximum efficiency. This performance can be achieved by reducing material, effort as well as money and still meet load-bearing behaviour requirements. Furthermore, optimisation processes can analyse the long-term development of a structure and anticipate possible damage. For degradation processes, in particular, predictions on the influences of various material parameters or changes in shape can lead to the reduction of long-term damage and the maintenance of load-bearing capacity despite long-term chemical exposure.

This work is based on continuum mechanics, which approximates the physical connections of a continuous and macroscopic body. The main aspects are therefore, the kinematic and kinetic description of a mathematical object as well as the balance equations for the qualification of the specific physical processes. On this basis, a coupled mechanical-chemical-degradation problem can be described mathematically as resulting in a set of partial differential equations. Permeable structures are applied, which allow gradient-based diffusion of concentrations. The chemical substances can cause material degradation and modification of material properties due to various chemical reactions. A mechanical degradation process is introduced that corresponds to negative growth, combining a constitutive and kinematic approach. Since this is a space and time-dependent problem, the material description is embedded in an FE-framework using an isoparametric concept for space discretisation and a Newmark-beta approach for time integration. In addition to the mechanical and physical conditions, continuum mechanics is based on differential geometry, which plays an important role in this thesis since an efficient structural optimisation framework can be integrated. By introducing a structural optimisation algorithm, it is possible to calculate an optimal geometry that considers the damage of long-term effects caused by environmental influences. In detail, the structural optimisation framework presents a shape optimisation with a gradient-based calculation, which contains information about the sensitivities of the parameters that influence the mechanical behaviour. Furthermore, a material parameter optimisation is developed to allow for the detection of harmful parameters and thus, preventing the degradation process.

With this work, a numerical model is available, simulating material degradation triggered by diffusion processes. The model contributes to the understanding, analysis and reduction of material degradation through optimisation procedures and ensures the long-term sustainability of structures under harmful environmental influences. It is a theoretical work illustrating the practical relevance with simple examples. The model is provided in such a way that different problems can be considered and integrated. The thesis presents a complete description of the structural analysis, sensitivity analysis, structural optimisation as well as numerical implementation with required variations and discretisation of a diffusion-driven degradation model.

1.2. Objectives

The objective of this work is the development of a simulation model for the optimisation of diffusion-driven degradation processes in a permeable structure. Hence, such a model's practical relevance is particularly evident in the context of civil engineering. Structures are tested for their stability, but yet gradually progressing environmental effects are neglected. Nevertheless, diffusion processes and chemical impact, for example, can strongly impair the material behaviour and thus, previously determined load-bearing capacities can no longer be maintained. The combined approach of a mechanical-chemical-degradation approach, which is embedded in an optimisation algorithm, makes it possible to consider diffusion processes and optimise geometry or material to avoid insidious long-term damage. The work serves as a basis and enables integrating specific chemical models to calculate problems, such as calcium leaching or chemical attacks.

Several numerical approaches deal with the simulation of chemical-induced degradation processes. In some cases, the chemical kinetics are in the foreground, others concentrate on the aspect of mechanical degradation, or some approaches serve to couple both. Including an optimisation concept is an essential step towards understanding and avoiding harmful processes. No work was discovered within the literature search that deals with combined structural optimisation of chemical-induced degradation comprehensively and above all time-efficient. A mathematical approach is chosen that embeds the kinematics of degradation with the common kinematic concept of structural optimisation. For structural optimisation, a parameter space is considered that ensures the representation of the material body independent of time or physical descriptions. Finally, a holistic approach for the simulation of coupled chemically induced mechanical degradation processes is provided, which also considers efficient optimisation algorithms.

Besides its practical relevance, the work mainly deepens general, theoretical research questions. Thus, the theoretical treatment of growth or degradation processes in continuum mechanics is an important objective. This work focuses on degradation processes, but the explanations can be applied equivalently to growth processes. Degradation processes are derived with a combined kinematic and constitutive approach. This aspect leads to the task; to create a comprehensive kinematic model within the framework of continuum mechanics. The model has to meet the requirements for structural mechanics and degradation processes. In addition to the kinematic approach, a constitutive approach is used to describe the degradation process. Chemical concentrations are introduced that trigger the material degradation. Another objective is the thermodynamic consistent evaluation of the continuum mechanical model, including chemical diffusion processes. This work provides an entirely consistent approach, considering mechanical and diffusion laws derived based on physical balance equations. With a further goal involving the numerical implementation of a coupled nonlinear and time-dependent problem, the structural analysis can be completed.

Furthermore, this thesis combines the mechanical-chemical model with a structural optimisation algorithm. Biology inspires the solution to how to prevent damaging material processes. In nature, evolutionary optimisation processes are pursued. For example, by reorienting the structure or changing the material's behaviour, a tree can prevent dying sections from jeopardising its existence. This idea is applied to engineering structures, thus, ensuring the load-bearing capacity despite negative environmental influences and, therefore, degradation processes. The goal demands an efficient and fast optimisation algorithm that combines optimisation with a degradation approach. This requirement is met by an approach of variational sensitivity analysis within structural optimisation. In particular, this approach's efficiency is highlighted and compared to conventional methods. A local convective parameter space supplements the kinematic to enable the variational approach, allowing a mathematical separation of displacements and geometry. On this basis, the continuous equations of the structural problem are established. Thus, within the sensitivity analysis scope, the required variations are related to a changeable design parameter (such as geometry parameters) can first be derived and then discretised. The order of first varying and then discretising allows advantages, especially for the mathematical approach to sensitivity analysis, see [6, 7]. The exact sequence is also used for the structural analysis. Furthermore, due to the geometry-dependency within the shape optimisation, a parameterised concept for meshing must be made possible. For this purpose, the software Gmsh is implemented and an automatic update of the design parameters is applied within the optimisation iteration.

The work requires an efficient implementation that reduces the numerical computational effort as much as possible and takes advantage of already existing, program-internal functions. This goal is realised by the combined use of MATLAB and developed FORTRAN functions. The numerical calculation program MATLAB, provided by Mathworks, enables fast calculations of matrix-based mathematics and provides efficient toolboxes for optimisation algorithms. It offers the possibility of embedding interfaces for functions formulated, for example, in the FORTRAN programming language. Thus, in the scope of this thesis, a MEX file is created, which contains a FORTRAN code that implements the derived element and material formulation of the mechanical-chemical-degradation approach. The numerical effort is reduced due to the embedded interfaces because the FORTRAN functions are mainly implemented via loop formulations known as a capacity bottleneck in the program MATLAB. Thus, the advantages of MATLAB can be exploited and the disadvantages of the slow programming environment for loop formulations can be avoided.

The work is divided into three different main fields. Firstly, the structural analysis and variation of a mechanical-chemical-degradation approach are established. Secondly, structural optimisation is introduced with consideration of shape and material optimisation for the derived continuum. In the third topic, the optimisation algorithm of the developed mechanical-chemical-degradation structural problem is presented and tested employing illustrative examples. The work's main research objectives can be assigned to these topics as follows.

1. Structural analysis of a mechanical-chemical-degradation model

- *Continuum model for a mechanical-chemical-degradation approach.*
- *Mechanical degradation with a combined kinematic and constitutive approach.*
- *Enhanced kinematics combining degradation and parameter space.*
- *Thermodynamically evaluation of a mechanical structure with chemical diffusion.*
- *FEM for a coupled single-phase solid mechanics and chemical concentrations.*

2. Structural optimisation of a mechanical-chemical-degradation model

- *Introduction of local convective parameter space.*
- *Variational sensitivity with an integrated continuum mechanical formulation.*
- *Efficient computational optimisation.*
- *Technical realisation of combining structural analysis with structural optimisation.*

3. Examples

- *Structural analysis examples, focusing on chemical-induced degradations.*
- *Structural optimisation examples, focusing on long-term degradation processes that can be prevented by optimised shape or fitted material parameters.*

1.3. Outline

An outline of the sections of the thesis is given. The topics addressed are briefly summarised and the reader is given an overview. In total, the thesis comprises eleven sections.

1 Introduction. In this first section, the structural optimisation of diffusion-driven degradation processes is introduced. Therefore, the motivation and objective of the work are highlighted.

2 Preliminaries and Notation. The numerical model derived in this work is based on tensor analysis's mathematical foundations. For this purpose, the basic notation and typography of the objects used are introduced. Furthermore, the applied program with interfaces for implementing the numerical model is presented.

3 Continuum Model. The continuum mechanical description is outlined for a permeable body with penetrating concentrations leading to material degradation. The classical continuum model of a body is extended by enhanced kinematics and additional material laws due to diffusive chemical concentrations and a degradation approach.

4 Structural Analysis. The classical Finite Element Method (FEM) is applied to the introduced continuum model. For this purpose, the weak formulations of the balance equations and the necessary variation for the solution of the nonlinear coupled problem are presented. The time integration method and spatial approximation concept are explained, and the numerical implementation is introduced.

5 Structural Optimisation. The basics of structural optimisation are outlined. In particular, the process of optimisation is demonstrated and the mathematical background of the constrained optimisation and nonlinear least-square problems are provided to address shape and material optimisation. Furthermore, geometric parameterisation requirements for the execution of shape optimisations are described.

6 Sensitivity Analysis. Sensitivity analysis is part of structural optimisation, where the sensitivities of the objective functions and constraints of the optimisation task based on the continuum mechanical quantities are calculated. In this thesis, the efficient variational sensitivity analysis is employed and the required variations are comprehensively presented.

7 Numerical Investigations. In this section, the implemented model for the optimisation of diffusion-driven degradation processes is tested by means of small examples. In particular, the variations derived analytically within the framework of the variational sensitivity analysis are compared with numerical approaches and the efficiency of the variational approach is highlighted. Furthermore, a convergence study is presented to control the time integration, and spatial approximations.

8 Examples of Structural Analysis. The developed continuum mechanical problem is introduced for a permeable body loaded with mechanical forces and chemical concentrations. Boundary value problems are set up for this purpose to simulate the material degradation and the resulting stress distributions in the body. Possible areas of application for the simulation of the presented problem in the context of civil engineering are shown.

9 Examples of Shape Optimisation. Shape optimisation is a fundamental task in the field of civil engineering to enable the efficient use of materials while ensuring load-bearing capacity. In this section, practical examples are presented to optimise the introduced geometries. Furthermore, the optimisation results based on analytically determined gradients are compared with numerical calculations and the efficiency of the optimisation method used is highlighted.

10 Examples of Material Parameter Optimisation. For further optimisation and, in particular, reduction of harmful degradation processes triggered by chemical concentrations, material optimisation is presented. Examples are outlined that highlight the added value of mathematical based structural optimisation applied to degradation processes.

11 Conclusion and Outlook. The final section summarises the work and highlights the objectives achieved. Furthermore, an outlook is given to proceed with the topic in the future and areas of application are suggested.

2. Preliminaries and Notation

This section gives an introduction to the applied mathematical notation for physical quantities. The general arithmetic operations between vectors and tensors of higher-order are listed. Furthermore, an overview of the software used to implement the derived problem follows.

2.0.1. Notation

Tensor algebra is an essential tool for the mathematical description of continuum mechanics and, thus, for the physical specification of a macroscopic body, such as geometry, the mapping between configurations or the stresses. The following Table 2.1 is introduced to distinguish between different tensors' orders with the notation used in this thesis.

Table 2.1.: Notation and typography.

Quantity	Typographic style	Examples
scalar	non-bold, italic	A, a, α
vector	bold, italic	$\boldsymbol{A}$, $\boldsymbol{a}$
tensor second-order	bold	$\mathbf{A}$, $\mathbf{a}$
tensor higher-order	blackboard	$\mathbb{A}$, $\mathbb{C}$
matrix, column matrix	bold, sans-serif	$\mathsf{\mathbf{A}}$, $\mathsf{\mathbf{a}}$
Voigt notation	bold, sans-serif, underline	$\underline{\mathsf{\mathbf{A}}}$, $\underline{\mathsf{\mathbf{a}}}$

Vectors $\boldsymbol{a} \in \mathcal{V}$, tensors $\mathbf{A} \in \mathcal{V} \otimes \mathcal{V}$ and tensor higher-order $\overset{n}{\mathbb{A}} \in \mathcal{V} \otimes \mathcal{V} \cdots \otimes \mathcal{V}$ (n-times) are introduced; $\mathcal{V}$ denotes the vector space. The index notation follows with

$$\boldsymbol{a} = a^i \, \mathbf{e}_i , \qquad \mathbf{A} = A^{ij} \, \mathbf{e}_i \otimes \mathbf{e}_j , \qquad \mathbb{A} = A^{ijk} \, \mathbf{e}_i \otimes \mathbf{e}_j \otimes \mathbf{e}_k \, , \tag{2.1}$$

where a finite sum in ordered pairs of vectors with the dyadic product of two vectors, denoting a higher-ordered tensor. The index notation deals with components or coordinates of vectors and tensors. The scalar product is illustrated by dots, a single contraction between two vectors by one dot and a double contraction between two second-order tensors by a colon, i.e.

$$\boldsymbol{a} \cdot \boldsymbol{b} \;=\; a_i\, b^i \qquad \mathbf{A} : \mathbf{B} \;=\; A_{ij}\, B^{ij} \,. \tag{2.2}$$

Furthermore, higher-ordered contraction between a fourth-order tensor and a second-order tensor are also represented by a colon with

$$\mathbb{A} : \mathbf{A} \;=\; A^{ijkl}\, A_{kl}\, \mathbf{e}_i \otimes \mathbf{e}_j \,. \tag{2.3}$$

2.0.2. Mathematical Background for Variations and Derivatives

For this work, variations and derivatives play an important role in structural and sensitivity analysis; further details on notation will follow in the corresponding sections. Nevertheless, the general mathematical description of variations and derivatives is introduced at this point.

First, the vector space $\mathcal{V}$ is introduced for all admissible state variables as well as their test functions and the vector space $\mathcal{S}$ contains all admissible design parameters. The Gateaux derivative for an arbitrary function $f(\boldsymbol{\nu}) : \mathcal{V} \to \mathbb{R}$ is a directional derivative of the differential function with respect to the variables $\boldsymbol{\nu} \in \mathcal{V}$, in the directions $\{\boldsymbol{\eta},\, \boldsymbol{\mu}\} \in \mathcal{V}$, as follows

$$\begin{aligned} f'_{\nu}(\boldsymbol{\nu};\boldsymbol{\eta}) \quad &:= \lim_{\epsilon\to 0}\frac{1}{\epsilon}\left[f(\boldsymbol{\nu}+\epsilon\,\boldsymbol{\eta}) - f(\boldsymbol{\nu})\right] &&= \frac{\mathrm{d}}{\mathrm{d}\epsilon} f(\boldsymbol{\nu}+\epsilon\,\boldsymbol{\eta})\bigg|_{\epsilon=0} \\ f''_{\nu,\nu}(\boldsymbol{\nu};\boldsymbol{\eta},\boldsymbol{\mu}) &:= \lim_{\epsilon\to 0}\frac{1}{\epsilon}\left[f'_{\nu}(\boldsymbol{\nu}+\epsilon\,\boldsymbol{\mu},\boldsymbol{\eta}) - f'_{\nu}(\boldsymbol{\nu};\boldsymbol{\eta})\right] &&= \frac{\mathrm{d}}{\mathrm{d}\epsilon} f'_{\nu}(\boldsymbol{\nu}+\epsilon\,\boldsymbol{\mu};\boldsymbol{\eta})\bigg|_{\epsilon=0} \,, \end{aligned} \tag{2.4}$$

wherein $f'_{\nu}(\boldsymbol{\nu};\boldsymbol{\eta})$ is the first directional derivative, which is linear with respect to $\boldsymbol{\eta}$. And $f''_{\nu,\nu}(\boldsymbol{\nu};\boldsymbol{\eta},\boldsymbol{\mu})$ is the second directional derivative, which is linear with respect to $\boldsymbol{\eta}$ and $\boldsymbol{\mu}$. The variation of the function $f(\bullet)$ is equal to the directional derivative

$$\delta_{\nu} f(\boldsymbol{\nu};\delta\boldsymbol{\nu}) \;=\; f'_{\nu}(\boldsymbol{\nu};\delta\boldsymbol{\nu}) \,, \tag{2.5}$$

this notation is used within this work. If the function depends on a second nonlinear function $\tilde{\boldsymbol{s}} \in \mathcal{S}$, so that $f(\boldsymbol{\nu},\tilde{\boldsymbol{s}}) : \mathcal{V} \times \mathcal{S} \to \mathbb{R}$, the total variation of the function reads

$$\delta f \;=\; \delta_{\nu} f(\boldsymbol{\nu},\tilde{\boldsymbol{s}};\delta\boldsymbol{\nu}) \;+\; \delta_{\tilde{s}} f(\boldsymbol{\nu},\tilde{\boldsymbol{s}};\delta\tilde{\boldsymbol{s}}) \,, \tag{2.6}$$

wherein $\delta_{\nu} f(\boldsymbol{\nu},\tilde{\boldsymbol{s}};\delta\boldsymbol{\nu})$ and $\delta_{\tilde{s}} f(\boldsymbol{\nu},\tilde{\boldsymbol{s}};\delta\tilde{\boldsymbol{s}})$ are the partial variations. In case of a direct dependency of the parameters, e.g. $\nu(\tilde{\boldsymbol{s}})$, the total partial variation is defined as follows

$$D_{\tilde{s}} f(\boldsymbol{\nu}(\tilde{\boldsymbol{s}}), \tilde{\boldsymbol{s}}) = \frac{\partial f}{\partial \tilde{\boldsymbol{s}}} + \frac{\partial f}{\partial \boldsymbol{\nu}} \frac{\mathrm{d}\boldsymbol{\nu}}{\mathrm{d}\tilde{\boldsymbol{s}}} \,. \tag{2.7}$$

2.0.3. Software

This section outlines the technical implementation of the mathematical derived material description for the mechanical-chemical-degradation approach, which is solved within the framework of FEM and embedded in an optimisation algorithm. For this purpose, a general overview of the programmatic implementation is given without details of the equations. The final purpose is to develop a numerical program that can solve the following problem:

„Optimisation of a boundary value problem coupled with mechanical and chemical influences lead to material degradation.“

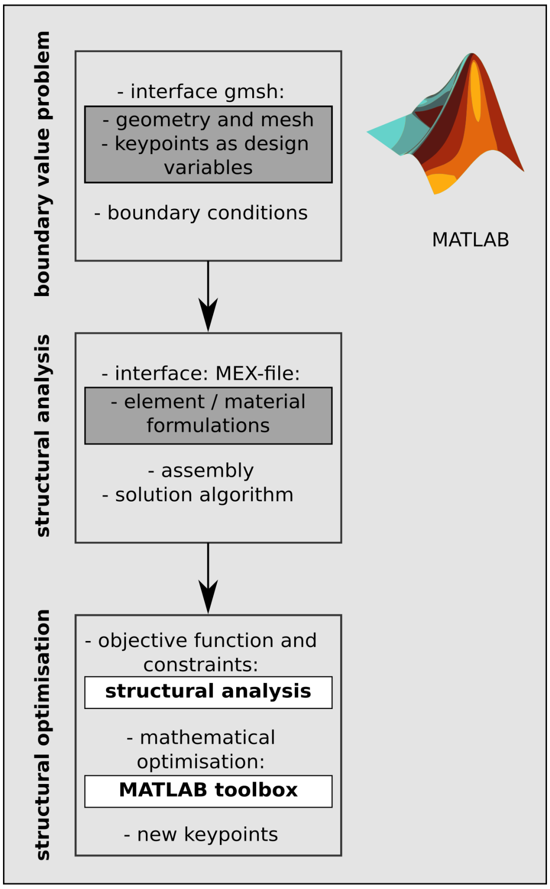

Figure 2.1.: Illustration of the algorithmic framework.

The program can essentially be divided into formulations for the element and global level. Firstly, the structural analysis is addressed. Therefore, a boundary value problem is generated, i.e. the finite mesh is created, the assembly of elements is implemented and the solution algorithm is performed. The solution algorithm is implemented globally in the MATLAB environment, wherein matrix formulations are applied. Secondly, mathematical optimisation is also performed globally, accessing the practical MATLAB toolboxes. The element level, in turn, contains the developed coupled differential equations for the description of a represented problem: the variational formulations with the discrete weak forms and the derived gradients. Information on the element level is implemented via the MEX interface, integrated into the MATLAB environment in a FORTRAN function. In summary, the global program runs in MATLAB, while the information from the element level is implemented in a FORTRAN code and embedded via MEX interfaces. The open software Gmsh is integrated into the global program via a second interface. Gmsh is used to generate the geometry and FE-mesh for the boundary value problem. The technical implementation of the program, taking into account the interfaces mentioned above, is illustrated in Figure 2.1.

MATLAB

The presented program is implemented and tested in MATLAB R2019b, wherein the operating system is LINUX. The main code to be executed is the developed SOP3DP (Structural Optimisation Program for Diffusion-Driven Degradation Process) and contains all necessary sub-functions and interfaces. The solution process for calculating the structural analysis is implemented in MATLAB, whereby the theoretical description is given in Sec. 4. The optimisation algorithm is integrated into MATLAB; the algorithm applies the MATLAB optimisation toolbox. Two different optimisation strategies are performed. The first is the optimisation of non-linear constraints, where a defined objective function is minimised under geometry change. In the second case, parameter optimisation is used to adapt the material parameters to a given objective function with a least-square problem. For the first optimisation strategy, the *fmincon* solver provided in the MATLAB optimisation toolbox is used. For the second strategy, the MATLAB function *lsqnonlin* is utilised to solve the least-squares problem. The preparation of the required objective functions, constraints, derivatives as well as Hessian matrices are specified in section 5. Further details on program implementation can be found in [92].

ParaView

„ParaView is an open-source, multi-platform scientific data analysis and visualisation tool that enables analysis and visualisation of extremely large datasets“ [105]. In this thesis, ParaView is utilised to post-process the structural and optimisation analysis. The calculation data produced by MATLAB are transferred into ParaView via the VTK format and can be displayed as contour images, videos, or other graphics.

Gmsh

The program Gmsh is an open-source program for the generation of FE-meshes. It can be used for 2D and 3D meshes by creating geometries with a CAGD (Computer-Aided Geometric Design) built-in engine and automatically meshing. Within the scope of this work, Gmsh is used due to its easy handling, the possibility to integrate it into the MATLAB code as well as the parametric input of the data. Overall, it enables the application of the modules geometry, mesh, solver and post-processing. For more information, see [54].

Program Interfaces

Interface: MEX file

The element and material formulations are implemented in the FORTRAN 77 programming language. Various subfunctions provide the discrete element formulations for the derived stiffness matrix, the pseudo-load matrix and other necessary derivatives. The theoretical background of the deduced equations is presented in this thesis, cf. Sec. 4. MATLAB uses a created gateway routine finterface.F as the entry point to the developed FORTRAN functions. Thus, the embedded MEX files are generated by the MATLAB command MEX, whereby the FORTRAN code is compiled with the GFortran compiler from [1].

Interface: Gmsh

The geometry is defined based on the CAGD approach. Points, lines and areas are used to create a geometry. The external program Gmsh combines the CAGD-based features with an automatic mesh generation. In this thesis, Gmsh is used and accessed via MATLAB to create a parameterised and structural mesh. To this effect, the program is applied via ASCII text files using Gmsh’s programming language via .geo files to generate geometries and meshes. The theoretical details are provided in Sec. 5.4.

3. Continuum Model

This section outlines the development of a coupled mechanical-chemical-degradation continuum problem. In addition to introducing the fundamental assumptions and equations for the continuum model, the primary literature is provided. In particular, the challenges of this work are highlighted. The kinematic and the physical properties of a mechanical-chemical-degradation problem are presented based on the balance equations and a thermodynamically consistent evaluation.

3.1. Introduction to the Continuum Model

In this thesis, an approach for calculating a coupled mechanical-chemical-degradation process is presented. One focus of this work is the mechanical growth, respectively degradation, which is approached by combining a kinematic and a constitutive strategy. On the one hand, the kinematic approach serves a multiplicative decomposition of the deformation into an elastic and a degradation contribution. Thereby, the split of the deformation is similar to the procedure for elastoplastic materials or similar damage mechanisms, see e.g. [40, 122, 125, 98, 96, 57]. With the extended kinematic concept, the mapping processes of a degraded continuum is represented. On the other hand, a constitutive formulation of the mass exchange is formulated. For this purpose, a chemical concentration is introduced as an additional degree of freedom that triggers the mass degradation of the material body. The physical behaviour of the coupled mechanical-chemical-degradation problem is derived, whereby, in particular, the properties of an open system must be fulfilled. Thereby, both the mechanical impulse and the conservation of mass, including diffusion processes, must be ensured. Coupled, nonlinear and partial differential equations arise, which are solved within the framework of structural mechanics. The energy process depends on the elastic strain and chemical concentrations. This work provides access to a fully thermodynamically consistent evaluation of entropy inequality; thus, physical laws for stress, mass sink and mass flux are derived.

In addition to the derivation of the continuum, the following section prepares the mathematical fundamentals for an inverse geometric approach. For this purpose, a parameter space is applied within the framework of kinematics. Thus, this work represents an enhanced kinematic approach that combines classical kinematics with a complementary parameter space as introduced in [6, 7] and furthermore, integrates degradation kinematics. The parameter space allows a description of the continuum independent of the geometry and displacement and provides better access to variations of continuum mechanical quantities. This access serves the basic for an efficient structural sensitivity approach in the framework of an optimisation algorithm.

Model Assumptions

The model considers a body, allowing the diffusion of concentrations due to its permeable structure. The body's mass exchange only takes place via so-called sink terms, which reduce the mass of the body. A mass flow of the macroscopic body is not considered. The concentrations are assumed to have a sufficiently small mass contribution, so they do not directly affect the density of the body. Indirectly, the concentrations trigger the mass degradation of the body, i.e. the mass sink term of the macroscopic body is calculated via the concentrations.

Body related assumptions

- *Open system*
- *Permeable body*
- *Chemical triggered degradation*
- *No in or out flux of mass*
- *Slow progression of degradation*
- *No consideration of acceleration terms*
- *No consideration of gravity forces*
- *Isothermal processes*

Concentrations related assumptions

- *Sufficiently small mass*
- *Gradient-based flow*
- *Single concentration considered*

3.2. State-of-the-Art for Presumptions on Continuum Model

3.2.1. Kinematics

The kinematics applied in this work are based on general definitions for the deformation of a material body. Reference is made here to the standard literature, [2, 110, 56]. However, in this thesis, two challenges are highlighted in the context of kinematics:

- *Growth processes,*
- *Local convective approach,*

which are sorted into the state-of-the-art in the following.

Remark: In this section, the term 'growth' is mainly used. It is a common term in the literature because 'growth' and 'degradation' only differ by an algebraic sign from a kinematic point of view.

Growth processes are of particular importance in the field of biomechanics. Thomsen shows already in 1917, that both the essential physical understanding and mathematical models for growth processes, are influenced by observations of nature, see [132]. Menzel et al. summarise in [97] growth and remodelling models for living structures. Mechanical growth and remodelling can be modelled either with a constitutive approach, a kinematic approach or a combination of both. Growth processes can be described by evaluating the time-dependent change in mass, density or volume of a structure. On the one hand, the constitutive approach concentrates on a thermodynamically consistent evaluation of the mass source, respectively mass sink and the mass flux, which enables the calculation of change in mass or density, see for instance [35, 61, 41, 80, 94]. The kinematic approach, on the other hand, allows the calculation of the variable mass or volume by applying a multiplicative decomposition of the deformation gradient, as applied in [114, 28, 3, 55, 95]. A useful alternative is the combination of the constitutive and kinematic approach, one example for this combination is presented by Ganghoffer in [45], where the calculation of surface growth in biological tissue is presented. He uses the multiplicative decomposition of the deformation gradient, as initially presented by [114], and applies a thermodynamically consistent approach to establish an evolutionary law for growth velocity. The multiplicative decomposition of the deformation gradient leads to a “growth tensor describing the local addition of material and an elastic tensor characterizing the reorganization of the body”, cf. [47]. Therefore, the development of the growth tensor, the so-called transplant tensor, is introduced as a state variable in the framework of finite elasticity. The numerical growth processes presented in biomechanics can be applied in the same way to any kind of mechanical structure. For example, in [29] growth is calculated as swelling and squeezing of an elastomeric gel in a continuum mechanical framework. Furthermore, in [78] is the reduction of the structural stiffness or strength in concrete structures due to chemical substances applied. In this thesis, the combination of the constitutive and kinematic approach is followed.

Barthold introduces in [6, 7] the *local convective approach* of local coordinates to access inverse geometry problems. This approach is based on fundamental concepts of the material body with Noll's intrinsic concept, presented in [102] respectively ongoing in [19, 58]. With the local convective approach, a kinematic separation of geometry and displacement occurs, which is especially helpful in the context of sensitivity analysis, see [13, 9, 7], to determine the required variations. This background is used to establish the extended kinematic framework in this work.

3.2.2. Coupled Problems

Within the framework of continuum mechanics, physical conservation laws are relevant. These material-independent balance equations establish the connection between changes in a physical quantity, such as mass or momentum, and the flux over the boundary of the body as well as internal production terms. To describe the full physical behaviour, besides the material-independent equations, the material-dependent equations are required, which are established in the context of thermodynamic evaluations. The introduction to the balance equations and extension of the thermodynamic evaluation is part of the standard-based procedure for the deformation of a continuum since 1960, presented in [133, 70, 34], among others. Furthermore, reference is made to the standard literature on continuum mechanics [15, 2, 110]. In principle, different, independent degrees of freedom can occur; for example, electric, plastic, magnetic, mechanical or chemical fields can be described as single-field problems or as coupled multi-field problems, cf. [20, 78]. In particular multi-field problems, resulting in more complex numerical models. Thus, the particular challenges of this work relate to:

- *Mechanical-chemical coupling,*
- *Thermodynamic evaluation for open systems.*

In this thesis, the multi-field phenomenon is considered in the extended environment of structural mechanics as a result of a *mechanical-chemical coupling.* Comparative approaches that address mechanical-chemical coupling are numerous [79, 134, 50, 16]. In particular, flux and production terms play an important role for mass exchange in the continuum, see [79, 78]. Furthermore, with the balance equations' extension, the influence on thermodynamics and the resulting statements on energy balance and entropy must be considered. For instance, [46, 86, 29] present a thermodynamically consistent derivation of mechanical-chemical coupled processes.

The method of classical thermodynamics can no longer be applied as soon as the mass exchange is taken into account due to the fact, a closed system no longer exists. For this reason, strategies for the *thermodynamic evaluation of open systems* must be applied. The first approach to consider mass exchange for the description of bone remodelling was introduced in 1976 by Cowin and Hegedus [35]. Furthermore, [81] presents the mass and volume-related thermodynamic evaluation approach of open systems in general. A detailed summary of the thermodynamics of these complex systems is given in [109]. Access via open systems has many similarities with mixture theory (cf. Truesdell and Toupin [133], and Bowen [24]). With the mixture theory's help, the interaction and exchange of different materials can be described, whereby the components are locally superimposed at any point in space. This theory is applied, for example, in the context of the theory of porous media, which can be used to describe growth processes of multi-phasic materials, e.g. [113].

With this background, this work provides both a mechanical-chemical coupled system and an open system that can represent degradation processes. The continuum is regarded as a single-phase open system.

3.3. Kinematics

3.3.1. Kinematic Concept

In this thesis, a comprehensive kinematic framework, providing a representation of the continuum mechanical formulation based on differential geometry, is utilised and subsequently extended by embedding degradation kinematics. Furthermore, a complementary parameters space is considered to access a variational sensitivity analysis. A graphical illustration of the applied kinematic framework is presented in Figure 3.1. Therein, the infinitesimal volume elements $\mathrm{d}V$, $\mathrm{d}v$, $\mathrm{d}V_\theta$ and $\mathrm{d}v_d$ are assigned to a reference configuration, an actual configuration, a parameter space and a degradation space. The parameter space allows the representation of continuum mechanical quantities independent of geometry and displacement. Furthermore, the deformation state can be classified by a multiplicative decomposition into an elastic and a degradation part due to the different configurations. It is assumed that the mass density's temporal development takes place in the reference configuration. The positions are introduced in the reference configuration $\boldsymbol{X}$, in the actual configuration $\boldsymbol{x}$, in the degradation space $\boldsymbol{x}_d$ and in the parameter space θ^i, namely the convective coordinates. The Cartesian base $\boldsymbol{Z}_i$ represents the parameter vector space $\boldsymbol{\theta} \in \mathbb{Z}^3$. The mapping $\boldsymbol{\varphi}_t$ describes the connection between the reference particles $\boldsymbol{X}$ to their spatial position $\boldsymbol{x} = \boldsymbol{\varphi}_t(\boldsymbol{X}, \mathrm{t})$. Furthermore, the mappings $\boldsymbol{\kappa}$, $\boldsymbol{\mu}$ and $\boldsymbol{v}$ link the parameter points $\boldsymbol{\theta}$ to their position in the reference $\boldsymbol{X} = \boldsymbol{\kappa}(\boldsymbol{\theta})$, actual configuration $\boldsymbol{x} = \boldsymbol{\mu}(\boldsymbol{\theta}, \mathrm{t})$, or in the degradation space $\boldsymbol{x}_d = \boldsymbol{v}(\boldsymbol{\theta}, \mathrm{t})$, where t represents time. The partial derivative of the mappings in relation to the coordinate lines lead to convective tangent vectors $\boldsymbol{G}_i$, $\boldsymbol{g}_i$ and $\boldsymbol{h}_i$, i.e.

$$\boldsymbol{G}_i = \frac{\partial \boldsymbol{\kappa}}{\partial \theta^i} \qquad \boldsymbol{g}_i = \frac{\partial \boldsymbol{\mu}}{\partial \theta^i} \qquad \boldsymbol{h}_i = \frac{\partial \boldsymbol{v}}{\partial \theta^i}\,, \tag{3.1}$$

with $i = 1, 2, 3$. The contravariant basis vectors, that determine the dual basis, are defined by $\boldsymbol{G}_i \cdot \boldsymbol{G}^j = \delta_i^j$, $\boldsymbol{g}_i \cdot \boldsymbol{g}^j = \delta_i^j$ and $\boldsymbol{h}_i \cdot \boldsymbol{h}^j = \delta_i^j$. This introduces the important two-point tensors that allow transformations between objects in relation to the respective configurations, i.e. $\mathbf{K}$, $\mathbf{M}$, $\mathbf{G}$ and $\mathbf{F}$

$$\begin{array}{lcccccc} \text{local geometry gradient} & : & \mathbf{K} & = & \boldsymbol{G}_i \otimes \boldsymbol{Z}^i & = & \mathrm{GRAD}\,\boldsymbol{\kappa} \\ \text{local deformation gradient} & : & \mathbf{M} & = & \boldsymbol{g}_i \otimes \boldsymbol{Z}^i & = & \mathrm{GRAD}\,\boldsymbol{\mu} \\ \text{local degradation gradient} & : & \mathbf{G} & = & \boldsymbol{h}_i \otimes \boldsymbol{Z}^i & = & \mathrm{GRAD}\,\boldsymbol{v} \\ \text{deformation gradient} & : & \mathbf{F} & = & \boldsymbol{g}_i \otimes \boldsymbol{G}^i & = & \mathrm{Grad}\,\boldsymbol{\varphi}_t\,. \end{array} \tag{3.2}$$

The kinematic concept basics are introduced according to [6, 7]. Thus, the reference and actual configuration from classical mechanics are extended to include the parameter space and the gradients, i.e. the local geometry and local deformation gradient are set up according to the records of [6]. In this work, the kinematics are extended by a degradation space and the associated gradients are introduced. The local degradation gradient $\mathbf{G}$ connects the parameter space with the introduced degradation space.

Remark: The local degradation gradient $\mathbf{G}$*, with the corresponding mapping* $\boldsymbol{v}$ *and the following determinant* J_G*, respectively, are introduced in the context of kinematics for the sake of completeness and serve to clarify the transformations introduced. In the following mathematical explanations of this thesis, the gradient can be dispensed for the time being. However, the important role for further research is presented in the outlook, see Sec. 11.2.*

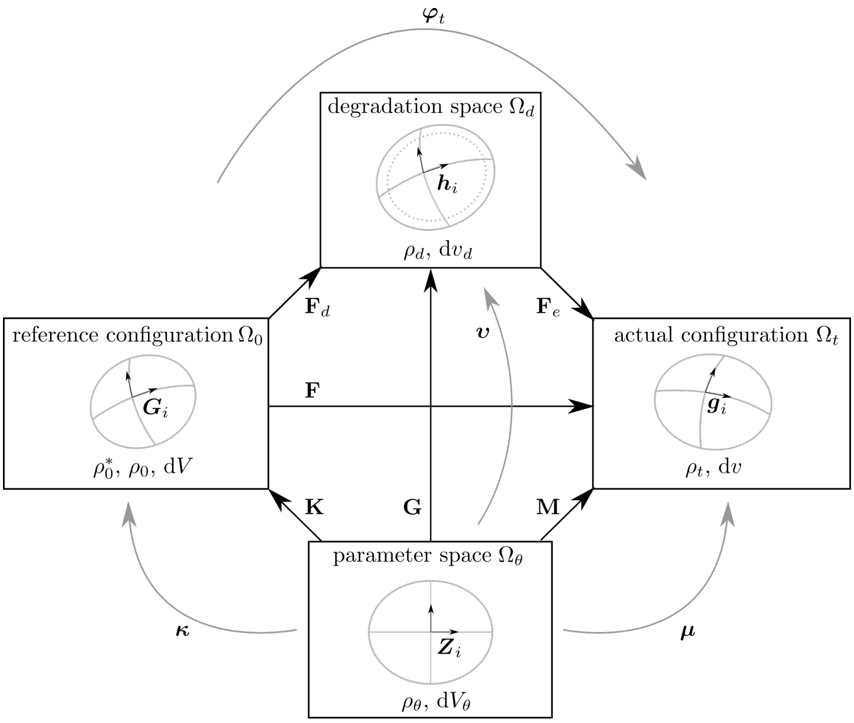

Figure 3.1.: Graphical illustration of the kinematic concept.

In general, the local gradients and divergence operators are described with GRAD and DIV as well as the referential quantities with Grad and Div and the spatial quantities with grad and div. The determinants of the introduced gradients follow straightforward, with

$$\begin{aligned} J &= \det(\operatorname{Grad}\boldsymbol{\varphi}_t) & J_M &= \det(\operatorname{GRAD}\boldsymbol{\mu}) \\ J_K &= \det(\operatorname{GRAD}\boldsymbol{\kappa}) & J_G &= \det(\operatorname{GRAD}\boldsymbol{\upsilon})\,. \end{aligned} \tag{3.3}$$

The commonly used deformation gradient $\mathbf{F}$ is related to the reference and actual configuration. Thus, mapping from reference to the actual configuration can be described by the composition $\boldsymbol{\varphi}_t := \boldsymbol{\mu} \circ \boldsymbol{\kappa}^{-1}$. Furthermore, local and referential gradients can be transformed by a local geometry gradient, respectively, deformation gradient. For an arbitrary transformed vector with $\tilde{\boldsymbol{t}}_X = \tilde{\boldsymbol{t}}_X(\boldsymbol{\kappa}(\boldsymbol{\theta})) = \tilde{\boldsymbol{t}}_\theta(\boldsymbol{\theta})$, respectively $\tilde{\boldsymbol{t}}_x = \tilde{\boldsymbol{t}}_x(\boldsymbol{\kappa}(\boldsymbol{\theta})) = \tilde{\boldsymbol{t}}_\theta(\boldsymbol{\theta})$, follows

$$\begin{aligned} \operatorname{Grad}\tilde{\boldsymbol{t}}_X &:= \frac{\partial \tilde{\boldsymbol{t}}_X}{\partial \theta^i} \otimes \boldsymbol{G}^i = \left(\frac{\partial \tilde{\boldsymbol{t}}_X}{\partial \theta^i} \otimes \boldsymbol{Z}^i\right)\left(\boldsymbol{Z}_j \otimes \boldsymbol{G}^j\right) = \operatorname{GRAD}\tilde{\boldsymbol{t}}_\theta\,\mathbf{K}^{-1} \\ \operatorname{grad}\tilde{\boldsymbol{t}}_x &:= \frac{\partial \tilde{\boldsymbol{t}}_x}{\partial \theta^i} \otimes \boldsymbol{g}^i = \left(\frac{\partial \tilde{\boldsymbol{t}}_x}{\partial \theta^i} \otimes \boldsymbol{Z}^i\right)\left(\boldsymbol{Z}_j \otimes \boldsymbol{g}^j\right) = \operatorname{GRAD}\tilde{\boldsymbol{t}}_\theta\,\mathbf{M}^{-1}\,, \end{aligned} \tag{3.4}$$

with the local gradient operator, i.e.

$$\mathrm{GRAD}\,\tilde{\boldsymbol{t}}_\theta := \frac{\partial \tilde{\boldsymbol{t}}_\theta}{\partial \theta^i} \otimes \boldsymbol{Z}^i\,. \tag{3.5}$$

A multiplicative decomposition of the deformation gradient $\mathbf{F}$ into an elastic part $\mathbf{F}_e$ and a degradation part $\mathbf{F}_d$ is applied.

$$\begin{aligned} &\text{Degradation gradient} &: \quad \mathbf{F}_d &= \boldsymbol{h}_i \otimes \boldsymbol{G}^i \\ &\text{Elastic deformation gradient} &: \quad \mathbf{F}_e &= \boldsymbol{g}_i \otimes \boldsymbol{h}^i\,. \end{aligned} \tag{3.6}$$

According to Lubarda and Hoger [87], an isotropic approach is used for the degradation contribution to the deformation gradient with the stretch ratio ν, to be specific

$$\begin{aligned} \mathbf{F} &= \mathbf{F}_e\,\mathbf{F}_d && \text{with} \\ \mathbf{F}_d &= \nu\,\mathbf{1} && \text{and} \qquad \nu = \sqrt[3]{\frac{\rho_0}{\rho_0^*}}\,, \end{aligned} \tag{3.7}$$

whereby $\mathbf{1}$ denotes the second-order identity tensors. Within the kinematic concept, the assumption is made that the density is maintained from the initial reference configuration to the degradation space, i.e.

$$\rho_0^* = \rho_d\,. \tag{3.8}$$

The mapping between the configurations, see Figure 3.1, leads to a change in volume, whereas mass is not influenced by such mappings, i.e. using Eq. (3.8)

$$\rho_0 = \rho_0^*\,J_d = \rho_d\,J_d = \rho_t\,J \quad ; \quad \rho_d = \rho_t\,J_e\,. \tag{3.9}$$

Moreover, $J_e = \det\mathbf{F}_e > 0$ denotes the determinant of the elastic part of the deformation gradient and $J = \det\mathbf{F} > 0$ as well as $J_d = \det\mathbf{F}_d = \dfrac{\rho_0}{\rho_0^*} > 0$, cf. Eq. (3.7), follows by analogy. With the introduced kinematics, the following line element yields with

$$\begin{aligned} \mathrm{d}\boldsymbol{X} &= \mathbf{K}\,\mathrm{d}\boldsymbol{\theta} \\ \mathrm{d}\boldsymbol{x} &= \mathbf{M}\,\mathrm{d}\boldsymbol{\theta} = \mathbf{F}\,\mathrm{d}\boldsymbol{X} = \mathbf{F}_e\,\mathrm{d}\boldsymbol{x}_d \\ \mathrm{d}\boldsymbol{x}_d &= \mathbf{G}\,\mathrm{d}\boldsymbol{\theta} = \mathbf{F}_d\,\mathrm{d}\boldsymbol{X}\,, \end{aligned} \tag{3.10}$$

the surface elements follow with

$$\begin{aligned}
\mathrm{d}\boldsymbol{A} &= \det \mathbf{K}\, \mathbf{K}^{-\mathrm{T}}\, \mathrm{d}\boldsymbol{A}_\theta \\
\mathrm{d}\boldsymbol{a} &= \det \mathbf{M}\, \mathbf{M}^{-\mathrm{T}}\, \mathrm{d}\boldsymbol{A}_\theta &= \det \mathbf{F}\, \mathbf{F}^{-\mathrm{T}}\, \mathrm{d}\boldsymbol{A} \;=\; \det \mathbf{F}_e\, (\mathbf{F}_e)^{-\mathrm{T}}\, \mathrm{d}\boldsymbol{a}_d \\
\mathrm{d}\boldsymbol{a}_d &= \det \mathbf{G}\, (\mathbf{G})^{-\mathrm{T}}\, \mathrm{d}\boldsymbol{A}_\theta &= \det \mathbf{F}_d\, (\mathbf{F}_d)^{-\mathrm{T}}\, \mathrm{d}\boldsymbol{A}\,,
\end{aligned} \tag{3.11}$$

and finally the volume elements follow with

$$\begin{aligned}
\mathrm{d}V &= \det \mathbf{K}\, \mathrm{d}V_\theta \\
\mathrm{d}v &= \det \mathbf{M}\, \mathrm{d}V_\theta &= \det \mathbf{F}\, \mathrm{d}V \;=\; \det \mathbf{F}_e\, \mathrm{d}v_d \\
\mathrm{d}v_d &= \det \mathbf{G}\, \mathrm{d}V_\theta &= \det \mathbf{F}_d\, \mathrm{d}V\,.
\end{aligned} \tag{3.12}$$

Table 3.1 shows exemplary the transformations for contravariant vectors $\{\tilde{\boldsymbol{t}}_x, \tilde{\boldsymbol{t}}_X, \tilde{\boldsymbol{t}}_\theta, \tilde{\boldsymbol{t}}_d\}$ and tensors $\{\tilde{\mathbf{T}}_x, \tilde{\mathbf{T}}_X, \tilde{\mathbf{T}}_\theta, \tilde{\mathbf{T}}_d\}$ using the previously introduced illustrations and two-field tensors.

Table 3.1.: Transformations for contravariant vectors and tensors with push-forward and pull-pack operations, cf. Barthold [6]; with extensions for the transformation from and to the degradation space.

From	To	Operation	Vector	Tensor
$\tilde{\mathbf{T}}_\theta$	$\tilde{\mathbf{T}}_X$	push-forward	$\tilde{\boldsymbol{t}}_X = \mathbf{K}\, \tilde{\boldsymbol{t}}_\theta$	$\tilde{\mathbf{T}}_X = \mathbf{K}\, \tilde{\mathbf{T}}_\theta\, \mathbf{K}^{\mathrm{T}}$
		pull-back	$\tilde{\boldsymbol{t}}_\theta = \mathbf{K}^{-1}\, \tilde{\boldsymbol{t}}_X$	$\tilde{\mathbf{T}}_\theta = \mathbf{K}^{-1}\, \tilde{\mathbf{T}}_X\, \mathbf{K}^{-\mathrm{T}}$
$\tilde{\mathbf{T}}_\theta$	$\tilde{\mathbf{T}}_x$	push-forward	$\tilde{\boldsymbol{t}}_x = \mathbf{M}\, \tilde{\boldsymbol{t}}_\theta$	$\tilde{\mathbf{T}}_x = \mathbf{M}\, \tilde{\mathbf{T}}_\theta\, \mathbf{M}^{\mathrm{T}}$
		pull-back	$\tilde{\boldsymbol{t}}_\theta = \mathbf{M}^{-1}\, \tilde{\boldsymbol{t}}_x$	$\tilde{\mathbf{T}}_\theta = \mathbf{M}^{-1}\, \tilde{\mathbf{T}}_x\, \mathbf{M}^{-\mathrm{T}}$
$\tilde{\mathbf{T}}_X$	$\tilde{\mathbf{T}}_x$	push-forward	$\tilde{\boldsymbol{t}}_x = \mathbf{F}\, \tilde{\boldsymbol{t}}_X$	$\tilde{\mathbf{T}}_x = \mathbf{F}\, \tilde{\mathbf{T}}_X\, \mathbf{F}^{\mathrm{T}}$
		pull-back	$\tilde{\boldsymbol{t}}_X = \mathbf{F}^{-1}\, \tilde{\boldsymbol{t}}_x$	$\tilde{\mathbf{T}}_X = \mathbf{F}^{-1}\, \tilde{\mathbf{T}}_x\, \mathbf{F}^{-\mathrm{T}}$
$\tilde{\mathbf{T}}_X$	$\tilde{\mathbf{T}}_d$	push-forward	$\tilde{\boldsymbol{t}}_d = \mathbf{F}_d\, \tilde{\boldsymbol{t}}_X$	$\tilde{\mathbf{T}}_d = \mathbf{F}_d\, \tilde{\boldsymbol{t}}_X\, \mathbf{F}_d^{\mathrm{T}}$
		pull-back	$\tilde{\boldsymbol{t}}_X = \mathbf{F}_d^{-1}\, \tilde{\boldsymbol{t}}_d$	$\tilde{\mathbf{T}}_X = \mathbf{F}_d^{-1}\, \tilde{\boldsymbol{t}}_d\, \mathbf{F}_d^{-\mathrm{T}}$
$\tilde{\mathbf{T}}_d$	$\tilde{\mathbf{T}}_x$	push-forward	$\tilde{\boldsymbol{t}}_x = \mathbf{F}_e\, \tilde{\boldsymbol{t}}_d$	$\tilde{\mathbf{T}}_x = \mathbf{F}_e\, \tilde{\boldsymbol{t}}_d\, \mathbf{F}_e^{\mathrm{T}}$
		pull-back	$\tilde{\boldsymbol{t}}_d = \mathbf{F}_d^{-1}\, \tilde{\boldsymbol{t}}_x$	$\tilde{\mathbf{T}}_d = \mathbf{F}_e^{-1}\, \tilde{\boldsymbol{t}}_x\, \mathbf{F}_e^{-\mathrm{T}}$
$\tilde{\mathbf{T}}_\theta$	$\tilde{\mathbf{T}}_d$	push-forward	$\tilde{\boldsymbol{t}}_d = \mathbf{G}\, \tilde{\boldsymbol{t}}_\theta$	$\tilde{\mathbf{T}}_d = \mathbf{G}\, \tilde{\boldsymbol{t}}_\theta\, \mathbf{G}^{\mathrm{T}}$
		pull-back	$\tilde{\boldsymbol{t}}_\theta = \mathbf{G}^{-1}\, \tilde{\boldsymbol{t}}_d$	$\tilde{\mathbf{T}}_\theta = \mathbf{G}^{-1}\, \tilde{\boldsymbol{t}}_d\, \mathbf{G}^{-\mathrm{T}}$

The transformations are applied to arbitrary vectors and tensors in the following form

$$\begin{aligned}
\tilde{\boldsymbol{t}}_x &= \tilde{t}^i\,\boldsymbol{g}_i & \tilde{\mathbf{T}}_x &= \tilde{T}^{ik}\,(\boldsymbol{g}_i \otimes \boldsymbol{g}_k)\\
\tilde{\boldsymbol{t}}_X &= \tilde{t}^i\,\boldsymbol{G}_i & \tilde{\mathbf{T}}_X &= \tilde{T}^{ik}\,(\boldsymbol{G}_i \otimes \boldsymbol{G}_k)\\
\tilde{\boldsymbol{t}}_\theta &= \tilde{t}^i\,\boldsymbol{Z}_i & \tilde{\mathbf{T}}_\theta &= \tilde{T}^{ik}\,(\boldsymbol{Z}_i \otimes \boldsymbol{Z}_k)\\
\tilde{\boldsymbol{t}}_d &= \tilde{t}^i\,\boldsymbol{h}_i & \tilde{\mathbf{T}}_d &= \tilde{T}^{ik}\,(\boldsymbol{h}_i \otimes \boldsymbol{h}_k)\,.
\end{aligned} \tag{3.13}$$

3.3.2. Deformations

In the previous section, the deformations are described with the introduced gradients. However, within the following continuum mechanical derivation, deformation measures are needed, which do not contain rigid body movements. For this reason, the right Cauchy Green tensor $\mathbf{C}$, respectively the left Cauchy Green tensor $\mathbf{B}$ as well as the inverses $\mathbf{C}^{-1}$ and $\mathbf{B}^{-1}$, are introduced with

$$\begin{aligned}
\mathbf{C} &= \mathbf{F}^{\mathrm{T}}\,\mathbf{F} = g_{ij}\,\boldsymbol{G}^i \otimes \boldsymbol{G}^j & \text{and} \qquad \mathbf{C}^{-1} &= g^{ij}\,\boldsymbol{G}_i \otimes \boldsymbol{G}_j\\
\mathbf{B} &= \mathbf{F}\,\mathbf{F}^{\mathrm{T}} = G^{ij}\,\boldsymbol{g}_i \otimes \boldsymbol{g}_j & \text{and} \qquad \mathbf{B}^{-1} &= G_{ij}\,\boldsymbol{g}^i \otimes \boldsymbol{g}^j\,.
\end{aligned} \tag{3.14}$$

Furthermore, the elastic right Cauchy Green tensor $\mathbf{C}_e$, respectively left Cauchy Green tensor $\mathbf{B}_e$ as well as the inverses $\mathbf{C}_e^{-1}$ respectively $\mathbf{B}_e^{-1}$ can be introduced with the elastic contribution to the deformation gradient as follows

$$\begin{aligned}
\mathbf{C}_e &= \mathbf{F}_e^{\mathrm{T}}\,\mathbf{F}_e = g_{ij}\,\boldsymbol{h}^i \otimes \boldsymbol{h}^j & \text{and} \qquad \mathbf{C}_e^{-1} &= g^{ij}\,\boldsymbol{h}_i \otimes \boldsymbol{h}_j\\
\mathbf{B}_e &= \mathbf{F}_e\,\mathbf{F}_e^{\mathrm{T}} = h^{ij}\,\boldsymbol{g}_i \otimes \boldsymbol{g}_j & \text{and} \qquad \mathbf{B}_e^{-1} &= h_{ij}\,\boldsymbol{g}^i \otimes \boldsymbol{g}^j\,.
\end{aligned} \tag{3.15}$$

The degradation part of the right Cauchy Green tensor $\mathbf{C}_d$, respectively left Cauchy Green tensor $\mathbf{B}_d$, follow in the same way with

$$\begin{aligned}
\mathbf{C}_d &= \mathbf{F}_d^{\mathrm{T}}\,\mathbf{F}_d = h_{ij}\,\boldsymbol{G}^i \otimes \boldsymbol{G}^j & \text{and} \qquad \mathbf{C}_d^{-1} &= h^{ij}\,\boldsymbol{G}_i \otimes \boldsymbol{G}_j\\
\mathbf{B}_d &= \mathbf{F}_d\,\mathbf{F}_d^{\mathrm{T}} = G^{ij}\,\boldsymbol{h}_i \otimes \boldsymbol{h}_j & \text{and} \qquad \mathbf{B}_e^{-1} &= G_{ij}\,\boldsymbol{h}^i \otimes \boldsymbol{h}^j\,.
\end{aligned} \tag{3.16}$$

Therein $G_{ij} = \boldsymbol{G}_i \cdot \boldsymbol{G}_j$, $G^{ij} = \boldsymbol{G}^i \cdot \boldsymbol{G}^j$, $g_{ij} = \boldsymbol{g}_i \cdot \boldsymbol{g}_j$, $g^{ij} = \boldsymbol{g}^i \cdot \boldsymbol{g}^j$, $h_{ij} = \boldsymbol{h}_i \cdot \boldsymbol{h}_j$ and $h^{ij} = \boldsymbol{h}^i \cdot \boldsymbol{h}^j$ are the metric coefficients. Finally, the strain tensors for use in the constitutive formulations are derived, again taking into account the decomposition into an elastic and degradation component.

The Green-Lagrange strain tensor $\mathbf{E}$ is introduced with

$$\mathbf{E} \,=\, \frac{1}{2}\,(\mathbf{C} \,-\, \mathbf{1}) \qquad \mathbf{E}_e \,=\, \frac{1}{2}\,(\mathbf{C}_e \,-\, \mathbf{1}) \qquad \mathbf{E}_d \,=\, \frac{1}{2}\,(\mathbf{C}_d \,-\, \mathbf{1})\,. \tag{3.17}$$

In addition, the Almansi strain tensor $\mathbf{A}$ is illustrated with

$$\mathbf{A} \,=\, \frac{1}{2}\,(\mathbf{1} \,-\, \mathbf{B}^{-1}) \qquad \mathbf{A}_e \,=\, \frac{1}{2}\,(\mathbf{1} \,-\, \mathbf{B}_e^{-1}) \qquad \mathbf{A}_d \,=\, \frac{1}{2}\,(\mathbf{1} \,-\, \mathbf{B}_d^{-1})\,, \tag{3.18}$$

and the Karni-Reiner strain tensor $\hat{\mathbf{K}}$ is stated as follows

$$\hat{\mathbf{K}} \,=\, \frac{1}{2}\,(\mathbf{B} \,-\, \mathbf{1}) \qquad \hat{\mathbf{K}}_e \,=\, \frac{1}{2}\,(\mathbf{B}_e \,-\, \mathbf{1}) \qquad \hat{\mathbf{K}}_d \,=\, \frac{1}{2}\,(\mathbf{B}_d \,-\, \mathbf{1})\,. \tag{3.19}$$

3.3.3. Selected Variations of Kinematics

The variations of the kinematic quantities relevant for this work are introduced in this section. Based on the presented configuration, which separates the geometry and displacement mapping, these partial variations and the total variations are derived. The partial variations of an arbitrary function f with respect to the virtual geometry field $\delta\boldsymbol{X}$ and with respect to the virtual displacement field $\delta\boldsymbol{u}$ follow with $\delta_X f$ and $\delta_u f$. Here, geometry $\boldsymbol{X}$ and displacement $\boldsymbol{u}$ are independent of each other. In addition to the kinematic quantities, concentrations c_γ are defined as independent degrees of freedom. The partial variation of a function depending on these concentrations $\delta_c f$ becomes relevant for the coupled problem. Thus, the total variation δf of an arbitrary function can be represented as the sum of the partial variations as follows

$$\delta f \,=\, \delta_X f \,+\, \delta_u f \,+\, \delta_c f\,. \tag{3.20}$$

Variation of the Gradients

The variations of the gradients in the parameter space and reference configuration are derived. First, the total variation of the local gradient operator applied on an arbitrary physical quantity in the parameter space $\tilde{\boldsymbol{t}}_\theta$ follows with

$$\delta(\mathrm{GRAD}\,\tilde{\boldsymbol{t}}_\theta) \,=\, \mathrm{GRAD}\,\delta\tilde{\boldsymbol{t}}_\theta\,. \tag{3.21}$$

The variation of the material gradient operator applied on a vector field in the reference configurations results in

$$\delta(\operatorname{Grad}\tilde{\boldsymbol{t}}_X) \;=\; \delta(\operatorname{GRAD}\tilde{\boldsymbol{t}}_\theta\,\mathbf{K}^{-1}) \;=\; \delta\operatorname{GRAD}\tilde{\boldsymbol{t}}_\theta\,\mathbf{K}^{-1} + \operatorname{GRAD}\tilde{\boldsymbol{t}}_\theta\,\delta\mathbf{K}^{-1}\,, \tag{3.22}$$

wherein Eq. (3.4) is applied. The following equations illustrate a connection between the local geometry gradient $\mathbf{K}$ and the identity tensor $\mathbf{1}$, i.e.

$$\begin{aligned} \mathbf{K}\,\mathbf{K}^{-1} &= \mathbf{1} \\ \delta(\mathbf{K}\,\mathbf{K}^{-1}) &= \mathbf{0} \\ \delta\mathbf{K}^{-1} &= -\mathbf{K}^{-1}\,\delta\mathbf{K}\,\mathbf{K}^{-1}\,, \end{aligned} \tag{3.23}$$

wherein, the relation being pointed out, that

$$\delta\mathbf{K}\,\mathbf{K}^{-1} \;=\; \delta\boldsymbol{G}_i \otimes \boldsymbol{G}^i \;= \operatorname{Grad}\delta\boldsymbol{X}\,. \tag{3.24}$$

Taking Eq. (3.4) and the relation described above into account, the total variation from Eq. (3.22) follows with

$$\delta(\operatorname{Grad}\tilde{\boldsymbol{t}}_X) \;=\; \operatorname{Grad}\delta\tilde{\boldsymbol{t}}_X \;-\; \operatorname{Grad}\tilde{\boldsymbol{t}}_X\operatorname{Grad}\delta\boldsymbol{X}\,. \tag{3.25}$$

It can be noticed that the gradient operator is constructed from two terms; one refers to the variation of the vector field $\tilde{\boldsymbol{t}}_X$ and the other to the corresponding contravariant basis $\boldsymbol{G}^i$. For this reason, the variation of the local gradient in Eq. (3.21) refers only to the vector field $\tilde{\boldsymbol{t}}_\theta$, as the basis $\boldsymbol{Z}^i$ is independent of geometry and displacement. Furthermore, the total variation $\delta(\operatorname{Grad}\tilde{\boldsymbol{t}}_X)$ can be split into the partial terms with

$$\begin{aligned} \delta_c(\operatorname{Grad}\tilde{\boldsymbol{t}}_X) &= \operatorname{Grad}\delta_c\tilde{\boldsymbol{t}}_X \\ \delta_u(\operatorname{Grad}\tilde{\boldsymbol{t}}_X) &= \operatorname{Grad}\delta_u\tilde{\boldsymbol{t}}_X \\ \delta_X(\operatorname{Grad}\tilde{\boldsymbol{t}}_X) &= \operatorname{Grad}\delta_X\tilde{\boldsymbol{t}}_X \;-\; \operatorname{Grad}\tilde{\boldsymbol{t}}_X\operatorname{Grad}\delta\boldsymbol{X}\,. \end{aligned} \tag{3.26}$$

Variation of the Deformation Gradient

Applying Eq. (3.26) on the deformation gradient $\mathbf{F} = \operatorname{Grad} \boldsymbol{x}$ results in

$$\begin{aligned} \delta_c(\operatorname{Grad} \boldsymbol{x}) &= \operatorname{Grad} \delta_c \boldsymbol{x} = \mathbf{0} \\ \delta_u(\operatorname{Grad} \boldsymbol{x}) &= \operatorname{Grad} \delta_u \boldsymbol{x} = \operatorname{Grad} \delta \boldsymbol{u} \\ \delta_X(\operatorname{Grad} \boldsymbol{x}) &= \operatorname{Grad} \delta_X \boldsymbol{x} - \operatorname{Grad} \boldsymbol{x} \operatorname{Grad} \delta \boldsymbol{X} = -\operatorname{Grad} \boldsymbol{u} \operatorname{Grad} \delta \boldsymbol{X} \,. \end{aligned} \tag{3.27}$$

Wherein the connection $\boldsymbol{x} = \boldsymbol{X} + \boldsymbol{u}$ is applied and the material displacement gradient is introduced with $\mathbf{H} = \operatorname{Grad} \boldsymbol{u} = \mathbf{F} - \mathbf{1}$. The concentrations are summarised in an independent degree of freedom; thus, the partial variation disappears for kinematic related quantities.

Variation of the Green-Lagrange Strain Tensor

Using the above described Eq. (3.27), the partial variations of the symmetric Green-Lagrange strain tensor $\mathbf{E}$ follows with

$$\begin{aligned} \delta_u \mathbf{E} &= \operatorname{sym}(\mathbf{F}^{\mathrm{T}} \operatorname{Grad} \delta \boldsymbol{u}) \\ \delta_X \mathbf{E} &= \operatorname{sym}(-\mathbf{F}^{\mathrm{T}} \operatorname{Grad} \boldsymbol{u} \operatorname{Grad} \delta \boldsymbol{X}) \,. \end{aligned} \tag{3.28}$$

Variations of the Determinants

For structural analysis, the partial variations of the determinant of the deformation gradient $J = \det \mathbf{F} = \det(\mathbf{C})^{1/2}$ are required, i.e.

$$\begin{aligned} \delta_u J &= \delta_E J : \delta_u \mathbf{E} = J \, \mathbf{C}^{-\mathrm{T}} : \delta_u \mathbf{E} \\ \delta_X J &= \delta_E J : \delta_X \mathbf{E} = J \, \mathbf{C}^{-\mathrm{T}} : \delta_X \mathbf{E} \,. \end{aligned} \tag{3.29}$$

In connection with the sensitivity analysis, the partial variation of the local geometry determinant $\delta_X J_K$ with respect to the virtual geometry field is applied. Again, the independence of the local base $\boldsymbol{Z}^i$ can be utilised and the relation $\delta_K \det \mathbf{K} = \det \mathbf{K} \, \mathbf{K}^{-\mathrm{T}}$ is used. Thus, it follows

$$\delta_X J_K = \det \mathbf{K} \, \mathbf{K}^{-\mathrm{T}} : \delta \mathbf{K} = \det \mathbf{K} \, \mathbf{1} : \operatorname{Grad} \delta \boldsymbol{X} = J_K \operatorname{Div} \delta \boldsymbol{X} \,, \tag{3.30}$$

wherein Eq. (3.24) is used.

Material Time Derivative

In addition to the kinematic quantities, which refer to local descriptions, time-dependencies are also used to calculate velocities. Therefore, the material time derivative of the elastic right Cauchy Green tensor from Eq. (3.15.1) is exemplary introduced at this point with $\dot{\mathbf{C}}_e$, i.e.

$$\dot{\mathbf{C}}_e = (\dot{\mathbf{F}}_e)^{\mathrm{T}}\,\mathbf{F}_e + \mathbf{F}_e^{\mathrm{T}}\,\dot{\mathbf{F}}_e = \mathbf{F}_e^{\mathrm{T}}\,\mathbf{l}^{\mathrm{T}}\;\mathbf{F}_e + \mathbf{F}_e^{\mathrm{T}}\,\mathbf{l}\;\mathbf{F}_e = 2\,\mathbf{F}_e^{\mathrm{T}}\mathbf{d}\,\mathbf{F}_e\,, \tag{3.31}$$

with

$$\dot{\mathbf{F}}_e = \mathbf{l}\,\mathbf{F}_e \quad \text{and} \quad \mathbf{d} = \frac{1}{2}\,(\mathbf{l}^{\mathrm{T}} + \mathbf{l})\,, \tag{3.32}$$

where $\mathbf{l} = \operatorname{grad}\dot{\boldsymbol{x}}$ represents the spatial velocity gradient with its symmetrical component $\mathbf{d}$. Further, necessary variations are listed in the course of the work.

3.4. Degradation Approach

The degradation model is based on combining a kinematic and constitutive approach. Therefore, the kinematic concept is presented in Sec. 3.3.1, where a decomposition of the deformation gradient represents the volume change of the material body into an elastic and a degradation part. The calculation of the degradation part $\mathbf{F}_d$ from Eq. (3.7.2) depends on the mass densities, on an initial mass density ρ_0^* and on the reference mass density ρ_0. The referential mass density is evaluated by the mass exchange in the reference configuration. Thus, the updated mass $\mathrm{d}m$ results from the initial mass $\mathrm{d}M$ and a mass sink term R_0 per unit volume, i.e.

$$\mathrm{d}m \;=\; \mathrm{d}M + \int\limits_{t_0}^{t} R_0\,\mathrm{d}t\,\mathrm{d}V\,. \tag{3.33}$$

This results in the time-dependent update of the initial mass density ρ_0^* to the resulting referential mass density ρ_0 with

$$\rho_0 \;=\; \rho_0^* + \int\limits_{t_0}^{\mathrm{t}} R_0\,\mathrm{d}t\,. \tag{3.34}$$

The equation for the mass sink term follows in the framework of the constitutive law, cf. Sec. 3.7. In principle, a connection between material degradation and concentrations is postulated. The concentrations c_γ are defined by corresponding molar density ρ_γ and molar mass M_γ, i.e.

$$c_\gamma \, = \, \frac{\rho_\gamma}{M_\gamma} \, . \tag{3.35}$$

Assuming that only one substance is considered, the degradation effect of the concentrations follows with

$$\rho_0 \, = \, \rho_0^* \, - \, c_\gamma \, M_\gamma \, , \tag{3.36}$$

whereby the Eq. (3.71) is anticipated. This thesis does not address more precise chemical processes to allow a wide range of applications. Nevertheless, the concentrations have to fulfil the balance of mass with

$$\int\limits_{\Omega_t} \dot{c}_\gamma \, \mathrm{d}v \, = \, -\int\limits_{\Gamma_t} \operatorname{grad} \boldsymbol{j}_\gamma \, \cdot \, \boldsymbol{n} \, \mathrm{d}a \, , \tag{3.37}$$

with the material time derivative of the concentrations $\dot{c}_\gamma$ and the flux of the concentrations $\boldsymbol{j}_\gamma$. The concentrations entering a structure Ω_t via a surface Γ_t are described by a time-dependent process, whereby $\boldsymbol{n}$ is a normal unit vector on the actual configuration. Therefore, the evolution of degradation depends on the history of the concentrations. In the course of this work, the concentrations are introduced as additional degrees of freedom within the framework of a coupled mechanical-chemical continuum model.

3.5. Stress Representations

Loads on the body lead to strain and stress; therefore, the stress is outlined below from a geometric perspective. First, the fundamental Cauchy stress tensor $\mathbf{T}$ is introduced, which refers to the actual configuration with

$$\mathbf{T} \, = \, T^{ij} \, \boldsymbol{g}_i \otimes \boldsymbol{g}_j \, , \tag{3.38}$$

wherein T^{ij} are the contravariant coefficients of the second-order tensor. Using the surface mapping from the actual configuration to the reference configuration, the so-called first Piola-Kirchhoff tensor $\mathbf{P}$, can be displayed, i.e.

$$\mathbf{P} \, = \, J \, \mathbf{T} \, \mathbf{F}^{-\mathrm{T}} \, = \, J \, T^{ij} \, \boldsymbol{g}_i \otimes \boldsymbol{G}_j \, . \tag{3.39}$$

The pull-back of the material first Piola-Kirchhoff tensor results in the second Piola-Kirchhoff tensor $\mathbf{S}_K$ with

$$\mathbf{S}_K \,=\, \mathbf{F}^{-1}\, J\, \mathbf{T}\, \mathbf{F}^{-\mathrm{T}} \,=\, \mathbf{F}^{-1}\, \mathbf{P} = \, J\, T^{ij}\, \boldsymbol{G}_i \otimes \boldsymbol{G}_j \,, \tag{3.40}$$

which refers entirely to the reference configuration. This tensor is helpful for numerical applications due to its symmetrical characteristics with $\mathbf{S}_K = \mathbf{S}_K^{\mathrm{T}}$.

The stress tensors can be displayed in all configurations using the introduced kinematic concept from Sec. 3.3.1. For example, the first Piola-Kirchhoff tensor $\mathbf{P}$ can be represented with the local geometry gradient $\mathbf{K}$ in the parameter space as follows

$$\mathbf{P}_\theta \,=\, J_K\, \mathbf{P}\, \mathbf{K}^{-\mathrm{T}} = \, J_M\, T^{ij}\, \boldsymbol{g}_i \otimes \boldsymbol{Z}_j \,. \tag{3.41}$$

3.5.1. First Principal Stress

For engineering complexities, such as maximum stress calculation, it often more logical to calculate the extreme values of the normal stresses using the principal stresses. Therefore, the first T_I, respectively second T_{II}, principal stress of the Cauchy stress tensor are introduced for a two-dimensional case as follows

$$T_{I,II} \,=\, \frac{I_T}{2} \pm \sqrt{\left(\frac{I_T}{2}\right)^2 - \, II_T} \,, \tag{3.42}$$

with the first and second scalar-valued invariant I_T, II_T and their variation with respect to the Cauchy stress tensor $\mathbf{T}$, i.e.

$$\begin{aligned} I_T &= \operatorname{tr} \mathbf{T} & \frac{\partial I_T}{\partial \mathbf{T}} &= \mathbf{1} \\ II_T &= \frac{1}{2}\,(I_T^2 \,-\, \operatorname{tr} \mathbf{T}^2) & \frac{\partial II_T}{\partial \mathbf{T}} &= I_T\, \mathbf{1} \,-\, \mathbf{T}^{\mathrm{T}} \,. \end{aligned} \tag{3.43}$$

3.5.2. Surface Stress

The overall stress contribution $\mathbf{F}^*$ of a body can be illustrated in the different configurations as follows

$$\mathbf{F}^* \,=\, \int\limits_{\Gamma_0} \boldsymbol{t}_X^*\, \mathrm{d}\boldsymbol{A} \,=\, \int\limits_{\Gamma_t} \boldsymbol{t}_x^*\, \mathrm{d}\boldsymbol{a} \,=\, \int\limits_{\Gamma_\theta} \boldsymbol{t}_\theta^*\, \mathrm{d}\boldsymbol{A}_\theta \,, \tag{3.44}$$

with the surface tensions $\boldsymbol{t}^*_X, \boldsymbol{t}^*_x, \boldsymbol{t}^*_\theta$ and the surfaces $\Gamma_0, \Gamma_t, \Gamma_\theta$. Applying the so-called Cauchy theorem, the surface stresses are connected via normal unit vectors $\boldsymbol{N}, \boldsymbol{n}, \boldsymbol{N}_\theta$ to the stress tensors, i.e.

$$\begin{aligned} \boldsymbol{t}^*_X &= \mathbf{P}\,\boldsymbol{N} && \forall && \boldsymbol{X} \in \Gamma_0 \\ \boldsymbol{t}^*_x &= \mathbf{T}\,\boldsymbol{n} && \forall && \boldsymbol{x} \in \Gamma_t \\ \boldsymbol{t}^*_\theta &= \mathbf{P}_\theta\,\boldsymbol{N}_\theta && \forall && \boldsymbol{\theta} \in \Gamma_\theta\,. \end{aligned} \tag{3.45}$$

3.6. Balance Equations

The balance equations are established for the coupled mechanical-chemical-degradation problem. Therefore, the classical balance equations are updated about additional terms caused by the mass exchange.

3.6.1. Balance of Mass

Due to the mass exchange of the material body via chemical concentrations, both the balance of mass for the macroscopic body and the balance of mass for the concentrations are introduced. The sink term of the mass in the reference configuration leads to a change of mass with $\mathrm{d}\dot{m} = R_0\,\mathrm{d}V$, see Eq. (3.33), and therefore, the balance of mass is referred to Eq. (3.34).

The balance of mass of the chemical concentrations contains the material time derivative of the concentrations $\dot{c}_\gamma$ and the flux of the concentrations $\boldsymbol{j}_\gamma$ is introduced in Eq. (3.37) and applies in the actual configuration with

$$\int\limits_{\Omega_t} (\dot{c}_\gamma + \operatorname{div}\boldsymbol{j}_\gamma)\,\mathrm{d}v = 0\,. \tag{3.46}$$

3.6.2. Balance of Linear Momentum

The balance of linear momentum is based on assuming that no volume forces act and no accelerations are considered. Therefore, the balance of linear momentum is only dependent on the Cauchy stress $\mathbf{T}$ with

$$\int\limits_{\Omega_t} \operatorname{div}\mathbf{T}\,\mathrm{d}v = \mathbf{0}\,, \tag{3.47}$$

in the actual configuration. Furthermore, it is emphasised that no additional momentum needs to be taken into account due to the mass exchange, as the degradation proceeds very slowly.

3.6.3. Balance of Moment of Momentum

The balance of moment of momentum, respectively angular momentum, is not listed. From this balance follows the statement that the Cauchy stress tensor $\mathbf{T}$ is symmetrical with

$$\mathbf{T} = \mathbf{T}^{\mathrm{T}} . \tag{3.48}$$

3.6.4. Balance of Energy

The energy balance is composed of the time derivative of the internal energy $\dot{E}$ and the kinetic energy $\dot{K}$, which correspond to the mechanical change $\mathrm{d}W$, the thermal change $\mathrm{d}Q$ and the chemical flux on the surface E_{c_γ}. Hence, the equation follows

$$\begin{aligned} \dot{E} + \dot{K} &= \mathrm{d}W + \mathrm{d}Q + E_{c_\gamma} \\ \int\limits_{\Omega_t} \dot{e}\,\mathrm{d}v &= \int\limits_{\Omega_t} (\mathbf{d} : \mathbf{T} + r - \operatorname{div}\boldsymbol{q})\,\mathrm{d}v - \int\limits_{\Gamma_t} \mu_\gamma\,\boldsymbol{j}_\gamma \cdot \mathrm{d}\boldsymbol{a} , \end{aligned} \tag{3.49}$$

with the derivative of the volume-specific internal energy $\dot{e}$, the volume-specific heat source r, the heat flux density $\boldsymbol{q}$, the chemical potential μ_γ and the spatial outward unit surface vector $\boldsymbol{n}$, which connects $\mathrm{d}\boldsymbol{a} = \boldsymbol{n}\,\mathrm{d}a$. The time derivative of the kinetic energy does not influence the balance of energy because the acceleration is neglected and the progression of the degradation is slow. Moreover, the surface part can be restated to the following

$$\int\limits_{\Gamma_t} \mu_\gamma\,\boldsymbol{j}_\gamma \cdot \mathrm{d}\boldsymbol{a} = \int\limits_{\Omega_t} \operatorname{div}(\mu_\gamma\,\boldsymbol{j}_\gamma)\,\mathrm{d}v , \tag{3.50}$$

with the connection

$$\operatorname{div}(\mu_\gamma\,\boldsymbol{j}_\gamma) = \boldsymbol{j}_\gamma \cdot \operatorname{grad}\mu_\gamma + \mu_\gamma \operatorname{div}\boldsymbol{j}_\gamma . \tag{3.51}$$

The local form of the balance of energy reads

$$-r + \operatorname{div}\boldsymbol{q} = -\dot{e} + \mathbf{d} : \mathbf{T} - \boldsymbol{j}_\gamma \cdot \operatorname{grad}\mu_\gamma + \mu_\gamma\,\dot{c}_\gamma , \tag{3.52}$$

using the balance of mass of the chemical concentrations as given in Eq. (3.46).

3.6.5. Balance of Entropy

Based on thermodynamics' second law, entropy never decreases in a closed system. This statement results in the requirement that entropy increases or remains constant. In this context, the entropy inequality follows with

$$\int_{\Omega_t} \dot{s}\,\mathrm{d}v \;\geq\; \int_{\Omega_t} \frac{1}{\Theta}\, r\,\mathrm{d}v \;-\; \int_{\Gamma_t} \frac{1}{\Theta}\,\boldsymbol{q}\,\cdot\,\mathrm{d}\boldsymbol{a}\,, \tag{3.53}$$

where $\dot{s}$ refers to the material time derivative of the volume-specific entropy and Θ denotes the absolute temperature. The surface part can be reformulated, i.e.

$$\int_{\Gamma_t} \frac{1}{\Theta}\,\boldsymbol{q}\,\cdot\,\mathrm{d}\boldsymbol{a} \;=\; \int_{\Omega_t} \operatorname{div}\left(\frac{1}{\Theta}\,\boldsymbol{q}\right)\mathrm{d}v\,, \tag{3.54}$$

and the following equation is converted to

$$\operatorname{div}\left(\frac{1}{\Theta}\,\boldsymbol{q}\right) \;=\; \boldsymbol{q}\,\cdot\,\operatorname{grad}\left(\frac{1}{\Theta}\right) \;+\; \frac{1}{\Theta}\operatorname{div}\boldsymbol{q} \;=\; -\,\frac{1}{\Theta^2}\,\boldsymbol{q}\,\cdot\,\operatorname{grad}\Theta \;+\; \frac{1}{\Theta}\operatorname{div}\boldsymbol{q}\,. \tag{3.55}$$

Substituting the reformulation into the entropy inequality (3.53) yields

$$0 \;\leq\; \Theta\,\dot{s} \;-\; r \;-\; \frac{1}{\Theta}\,\boldsymbol{q}\,\cdot\,\operatorname{grad}\Theta \;+\; \operatorname{div}\boldsymbol{q}\,. \tag{3.56}$$

The isothermal conditions, i.e. $\boldsymbol{q} = \boldsymbol{0}$ as well as $\dot{\Theta} = 0$, are established. Thus, from the local form of the energy balance, cf. Eq. (3.52), follows the constraint with

$$0 \;\leq\; \Theta\,\dot{s} \;-\; \dot{e} \;+\; \mathbf{d}\,:\,\mathbf{T} \;-\; \boldsymbol{j}_\gamma\,\cdot\,\operatorname{grad}\mu_\gamma \;+\; \mu_\gamma\,\dot{c}_\gamma\,, \tag{3.57}$$

this results in the so-called Clausius-Planck representation of entropy inequality.

3.7. Constitutive Formulations

In order to fully understand the physical behaviour of the introduced mechanical-chemically coupled degradation problem, a thermodynamically consistent evaluation and the introduction of the constitutive equations are outlined. From a thermodynamic perspective, an open system is regarded as a single-phase. The mechanical and chemical properties of the body are coupled using volume-specific access. As a result, constitutive equations for the stress, the sink term of mass exchange and the concentrations' flux term can be established.

3.7.1. Evaluation of the Entropy

Using the method of Coleman and Noll [34], the Clausius-Planck representation of the entropy inequality from Eq. (3.57) can be evaluated. The thermodynamic consistency is ensured and the necessary constitutive equations can be established. According to Helmholtz, free energy ψ is a thermodynamic potential and can be obtained from a thermodynamic system at constant temperature and volume with

$$\dot{\psi} = \dot{e} - \Theta\,\dot{s}\,. \tag{3.58}$$

By inserting the Helmholtz free energy into the entropy inequality in Eq. (3.57) and selecting the elastic right Cauchy Green tensor and the concentrations to derive the energy process with $\psi(\mathbf{C}_e, c_\gamma)$, the following restriction is obtained

$$-\frac{\partial\psi}{\partial\mathbf{C}_e} : \dot{\mathbf{C}}_e + \mathbf{d} : \mathbf{T} - \frac{\partial\psi}{\partial c_\gamma}\dot{c}_\gamma + \mu_\gamma\,\dot{c}_\gamma - \boldsymbol{j}_\gamma \cdot \operatorname{grad}\mu_\gamma \geq 0\,, \tag{3.59}$$

whereby the last part $[-\boldsymbol{j}_\gamma \cdot \operatorname{grad}\mu_\gamma]$ is irreversible and the other parts of the equation are reversible. The set of energy functions can be separated into a mechanical ψ^{M} and chemical ψ^{C} part with their respective dependencies,

$$\psi(\mathbf{C}_e, c_\gamma) = \psi^{\mathrm{M}}(\mathbf{C}_e) + \psi^{\mathrm{C}}(c_\gamma)\,. \tag{3.60}$$

In order to ensure the entropy inequality, the reversible contributions are evaluated and the Cauchy stress $\mathbf{T}$ as well as the chemical potential μ_γ are determined as follows

$$\begin{aligned} \mathbf{T} &= 2\,\mathbf{F}_e\,\frac{\psi^{\mathrm{M}}}{\partial\mathbf{C}_e}\,\mathbf{F}_e^{\mathrm{T}} \\ \mu_\gamma &= \frac{\partial\psi^{\mathrm{C}}}{\partial c_\gamma}\,, \end{aligned} \tag{3.61}$$

wherein Eq. (3.31) is applied. The irreversible part of the entropy inequality motivates the flux of the concentrations $\boldsymbol{j}_\gamma$. Thus, the constitutive equation is based on the classical diffusion equation, the so-called Fick's law, so that

$$\boldsymbol{j}_\gamma = -D\operatorname{grad}c_\gamma\,. \tag{3.62}$$

D is introduced as a diffusion coefficient. The transformation from the material flux to the spatial flux reads as follows

$$\boldsymbol{J}_\gamma \,=\, \boldsymbol{j}_\gamma \operatorname{cof}(\mathbf{F}) \,=\, -J\,D\,\operatorname{Grad} c_\gamma\, \mathbf{C}^{-1}\,, \tag{3.63}$$

wherein the cofactor is applied with $\operatorname{cof}(\mathbf{F}) \,=\, J\,\mathbf{F}^{-\mathrm{T}}$.

3.7.2. Invariant Representations

Within the thermodynamic evaluation framework, the principle of material objectivity must be fulfilled, i.e. the constitutive equations must be independent of the state of motion. The chosen mechanical energy requires an independent representation within the coupled mechanical-chemical model, which is invariant to superimposed rigid body motions. As the elastic right Cauchy Green tensor is set as an independent process variable, the invariant and their variations follow with

$$\begin{aligned} I_{C_e} &= \operatorname{tr}\mathbf{C}_e & \frac{\partial I_{C_e}}{\partial \mathbf{C}_e} &= \mathbf{1} \\ II_{C_e} &= \frac{1}{2}\,(I_{C_e}^2 \,-\, \operatorname{tr}\mathbf{C}_e^2) & \frac{\partial II_{C_e}}{\partial \mathbf{C}_e} &= I_{C_e}\,\mathbf{1} \,-\, \mathbf{C}_e^{\mathrm{T}} \\ III_{C_e} &= \det(\mathbf{C}_e) & \frac{\partial III_{C_e}}{\partial \mathbf{C}_e} &= III_{C_e}\,\mathbf{C}_e^{-\mathrm{T}}\,. \end{aligned} \tag{3.64}$$

3.7.3. Specifications of Energy Contributions

The mechanical energy is described by applying the hyperelastic Neo-Hooke material $\psi^{\mathrm{N}eo}$, to be specific

$$\begin{aligned} \psi^{\mathrm{M}} &= \rho_t\,\psi^{\mathrm{N}eo} \\ \psi^{\mathrm{N}eo} &= \frac{1}{\rho_0^*}\left[\frac{1}{2}\,\lambda\,(\sqrt{III_{C_e}} \,-\, 1)^2 \,-\, \mu\,\ln\sqrt{III_{C_e}} \,+\, \frac{1}{2}\,\mu\,(I_{C_e} \,-\, 3)\right]. \end{aligned} \tag{3.65}$$

This representation provides a form depending on the invariant given in Eq. (3.64) and contains material parameters μ and λ. Additionally, the parameters E and ν are introduced, representing the modulus of elasticity and the Poisson's ratio.

These are related to the material parameters as follows

$$
\begin{aligned}
\mu &= \frac{E}{2\,(1\,+\,\nu)} \\
\lambda &= \frac{E\,\nu}{(1\,+\,\nu)\,(1\,-\,2\,\nu)}\,.
\end{aligned}
\tag{3.66}
$$

In addition, a chemical part contribution to the energy is introduced with ψ^{C} as follows

$$
\psi^{\mathrm{C}} \,=\, c_\gamma\,\mu_\gamma^0 \,+\, R\,\Theta\,(-c_\gamma \,+\, c_\gamma\,\ln\frac{c_\gamma}{c_\gamma^0})\,,
\tag{3.67}
$$

with the constant standard potential μ_γ^0 and concentration c_γ^0 from the reference condition. Additionally, the absolute temperature and a gas constant are illustrated with Θ and R. Inserting the mechanical and chemical Helmholtz energy ansatz into Eq. (3.61) results, first, in the constitutive equation for the Cauchy stress

$$
\begin{aligned}
\mathbf{T} &= \frac{\rho_t}{\rho_0^*}\,\mathbf{F}_e\left[\lambda\,(J^e\,-1)J^e\,(\mathbf{C}_e)^{-\mathrm{T}}\,-\,\mu\,(\mathbf{C}_e)^{-\mathrm{T}}\,+\,\mu\,\mathbf{1}\right]\mathbf{F}_e^{\mathrm{T}} \\
&= \frac{\rho_t}{\rho_0^*}\left[\lambda\,(J^e\,-1)J^e\,\mathbf{1}\,+\,2\,\mu\,\hat{\mathbf{K}}_e\right],
\end{aligned}
\tag{3.68}
$$

with the elastic part of the Karni-Reiner strain tensor from Eq. (3.19.2). Under consideration of the deformation decomposition from Eq. (3.7) and the mapping of the Cauchy stress tensor within Eq. (3.40) follows the first and the second Piola-Kirchhoff stress tensor with

$$
\begin{aligned}
\mathbf{P} &= \frac{\rho_0}{\rho_0^*}\left[\mu\,\mathbf{F}_e\,\mathbf{F}_d^{-\mathrm{T}}\,-\,[\mu\,-\,\lambda\,(J_e\,-1)\,J_e]\,\mathbf{1}\,\mathbf{F}^{-\mathrm{T}}\right] \\
\mathbf{S}_K &= \frac{\rho_0}{\rho_0^*}\left[\mu\,\mathbf{C}_d^{-1}\,-\,[\mu\,-\,\lambda\,(J_e\,-1)\,J_e]\,\mathbf{C}^{-1}\right].
\end{aligned}
\tag{3.69}
$$

Secondly, the constitutive equation for the chemical potential follows with

$$
\mu_\gamma \,=\, \mu_\gamma^0\,+\,R\,\Theta\,\ln\frac{c_\gamma}{c_\gamma^0}\,.
\tag{3.70}
$$

Taking the model assumptions into account, the constitutive formulation for the mass sink term R_0 is postulated, based on the assumptions from Sec. 3.4, resulting in

$$
R_0 \,=\, -\dot{\rho}_\gamma\,,
\tag{3.71}
$$

wherein the chemical concentrations trigger the material degradation.

Based on the derived constitutive equations, the mechanical-chemical-degradation model is dependent on material parameters; these are summarised in the material parameters vector $\boldsymbol{m}$ with

$$\boldsymbol{m} := \begin{bmatrix} \mu & \lambda & \rho_0^* & M_\gamma & c_\gamma^0 & D \end{bmatrix}^{\mathrm{T}} , \tag{3.72}$$

whereby μ and λ are the first and second Lamé constants, ρ_0^* is the initial mass density, M_γ is the molar mass, c_γ^0 is the initial concentration and D is the diffusion coefficient.

3.8. Concluding Remarks for the Continuum Model

A coupled mechanical-chemical-degradation model is developed in this section and the necessary fundamentals are presented. Furthermore, the following insights are gained.

- *The classical kinematics are extended by a degradation space and a parameter space. Thus, a mathematical basis for continuum mechanical derivations is formulated.*
- *Important tensors for the description of deformations, stresses as well as several necessary variations are introduced.*
- *The development of a degradation model is presented.*
- *The complete description of the thermodynamically consistent, material-independent and material-dependent equations of the mass-degrading system, i.e. open system, is available.*

4. Structural Analysis

This section presents the numerical implementation of the mechanical-chemical-degradation continuum model. To solve the structural-mechanical problem, the FEM is applied. Due to the nonlinear dependencies, the bilinear form for the tangential stiffness is determined for the solution of the structural analysis.

4.1. Introduction to Structural Analysis

A set of coupled partial differential equations follow from the mechanical-chemical-degradation continuum model, which is time-dependent and highly nonlinear. This section presents the application of the standard-based FEM to the coupled mechanical-chemical-degradation approach. In particular, the Bubnov-Galerkin method is utilised and therefore, spatial discretisation and time integration as well as an iterative procedure to solve the multi-field problem are required. Due to the widespread utilisation of the FEM, reference is made to the standard literature, e.g. [145, 14, 128, 140], respectively the literature is cited in the appropriate contexts. Thus, a detailed introduction to the FEM is not required. However, the required equations for applying the FEM are listed in detail, and the weak formulations of the balance equations are introduced. Moreover, the FEM uses the Newton-Raphson method to determine the solution of the nonlinear problem, and thus the linearised weak formulations are derived. Since the mechanical-chemical-degradation problem contains both spatial and temporal dependencies, the spatial discretisation and time integration approaches are outlined. The linearisation and discretisation order is selected based on the chosen variational sensitivity analysis in the structural optimisation. Thus, all continuous equations are first varied and then discretised. On this basis, the essential matrix representations from the discrete formulations are provided for numerical implementation. The nomenclature introduced in this work with the abbreviation for the continuum model listed therein and the numerical investigations are utilised.

4.2. Weak Formulation in the Reference Configuration

The FEM is applied to solve the coupled mechanical-chemical-degradation model. In the framework of the numerical solution, the Bubnov-Galerkin method is applied, where the balance equations are presented in their weak form and weighted by independent test functions. In detail, the set of unknown primary variables $R = \{\boldsymbol{u}, c_\gamma\}$ include the displacement $\boldsymbol{u} = \boldsymbol{x} - \boldsymbol{X}$ and the concentrations c_γ. The weak formulation R can be divided into a mechanical R_u and a chemical R_{c_γ} part, i.e.

$$R(\boldsymbol{u},\, c_\gamma,\, \boldsymbol{\eta},\, \gamma) \;=\; R_u(\boldsymbol{u},\, c_\gamma,\, \boldsymbol{\eta}) \,+\, R_{c_\gamma}(\boldsymbol{u},\, c_\gamma,\, \gamma)\,. \tag{4.1}$$

On the one hand, the mechanical part of the weak form is derived by the weighted balance of momentum with a test function for the displacement $\boldsymbol{\eta}$ yet, on the other hand, the chemical part of the weak form is derived by the weighted balance of mass of the concentrations with a test function for the concentrations γ. All admissible test functions are introduced in the vector space $\mathcal{S}$. In order to complete the boundary value problem, either Dirichlet (first-type) boundary conditions $\Gamma_0^D = \{\Gamma_0^u, \Gamma_0^{c_\gamma}\}$ or Neumann (second-type) boundary conditions $\Gamma_0^N = \{\Gamma_0^t, \Gamma_0^{J_\gamma}\}$ are provided and prescribed within the given weak formulation. They can be identified by the corresponding surface integral. The Dirichlet boundary conditions are specified directly from the displacements, respectively concentrations. It should be noted that the Dirichlet and Neumann boundaries satisfy $\Gamma_0 = \Gamma_0^N \cup \Gamma_0^D$ and $\emptyset = \Gamma_0^N \cap \Gamma_0^D$.

Weak Formulation for Balance of Momentum in the Reference Configuration

The mechanical part of the weak form is represented by the balance of momentum and follows in the reference configuration with

$$\begin{aligned} R_u(\boldsymbol{u},\, c_\gamma,\, \boldsymbol{\eta}) \;&=\; \int\limits_{\Omega_0} \mathbf{P} \,:\, \mathrm{Grad}\,\boldsymbol{\eta}\,\mathrm{d}V \;-\; \int\limits_{\Gamma_0} \mathbf{P}\,\boldsymbol{N} \,\cdot\, \boldsymbol{\eta}\,\mathrm{d}A \\ &=\; \int\limits_{\Omega_0} \mathbf{S}_K \,:\, \delta_u\mathbf{E}\,\mathrm{d}V \;-\; \int\limits_{\Gamma_0} \boldsymbol{t}_X^* \,\cdot\, \boldsymbol{\eta}\,\mathrm{d}A\,, \end{aligned} \tag{4.2}$$

therein the mapping of the stress tensor is applied, which is presented in Sec. 3.5. Due to the scalar product with the symmetric second Piola-Kirchhoff tensor $\mathbf{S}_K$, the symmetric part of the variation of the Green-Lagrange strain tensor $\delta_u\mathbf{E}$ from Eq. (3.28) can also be used. The boundary conditions of the weak formulation are provided by either Dirichlet

Γ_0^u or Neumann Γ_0^t boundary conditions, i.e

$$\begin{aligned} \boldsymbol{u} &= \boldsymbol{u}^* \quad \forall \quad \boldsymbol{X} \in \Gamma_0^u \\ \mathbf{P}\,\boldsymbol{N} &= \boldsymbol{t}_X^* \quad \forall \quad \boldsymbol{X} \in \Gamma_0^t\,. \end{aligned} \tag{4.3}$$

Weak Formulation for Balance of Mass in the Reference Configuration

The chemical part of the weak form refers to the balance of mass of the concentrations; this is given in the reference configuration by

$$\begin{aligned} R_{c_\gamma}(\boldsymbol{u},\, c_\gamma,\, \gamma) &= \int\limits_{\Omega_0} (\dot{c}_\gamma\, J\,\gamma - \boldsymbol{j}_\gamma \cdot \operatorname{grad}\gamma\, J)\mathrm{d}V - \int\limits_{\Gamma_0} \boldsymbol{j}_\gamma \cdot \gamma\;\; J\,\mathbf{F}^{-\mathrm{T}}\,\boldsymbol{N}\,\mathrm{d}A \\ &= \int\limits_{\Omega_0} (\dot{c}_\gamma\, J\,\gamma - \boldsymbol{J}_\gamma \cdot \operatorname{Grad}\gamma\,)\mathrm{d}V - \int\limits_{\Gamma_0} \boldsymbol{J}_\gamma \cdot \gamma\,\boldsymbol{N}\,\mathrm{d}A\,, \end{aligned} \tag{4.4}$$

wherein the transformation from the material flux to the spatial flux is applied from Eq. (3.63) and the connection $\operatorname{grad}\gamma\,\mathbf{F} = \operatorname{Grad}\gamma$ are utilised. The Dirichlet boundary conditions on $\Gamma_0^{c_\gamma}$ are introduced directly by the concentrations, and the Neumann boundary conditions are determined by a concentration flux $\boldsymbol{J}_\gamma$ into the direction of the material normal unit vector $\boldsymbol{N}$ on the surface $\Gamma_0^{J_\gamma}$, i.e.

$$\begin{aligned} c_\gamma &= c_\gamma^* \quad \forall \quad \boldsymbol{X} \in \Gamma_0^{c_\gamma} \\ \boldsymbol{J}_\gamma \cdot \boldsymbol{N} &= J_\gamma^* \quad \forall \quad \boldsymbol{X} \in \Gamma_0^{J_\gamma}\,, \end{aligned} \tag{4.5}$$

with the initial condition $c_\gamma(\mathrm{t}_0) = c_\gamma^0$.

4.3. Linearisation of the Weak Formulation

The solution of the nonlinear coupled problem is determined by applying the Newton-Raphson method, see referring literature in, e.g. [23, 67, 140]. This numerical approach meets the requirement that the weak form equals zero. The weak formulation is a continuously differentiable function dependent on the introduced primary variables and their time derivative, which is approximated by a linear function using the Taylor series. Overall, the iterative solution process allows a quadratic convergence close to the solution. Therefore, the directional derivative (the variation of the weak form in the direction of the field variables) must be provided in each iteration point. Thus, the required multi-linear representation of the weak formulation follows with

$$\delta R = \delta_u R + \delta_{c_\gamma} R = 0 \, , \tag{4.6}$$

with the partial variation $\delta_u R$ and $\delta_{c_\gamma} R$ referring to the primary variables, the displacements $\boldsymbol{u}$ respectively concentrations c_γ. Thus, it follows

$$\begin{aligned} \delta_u R &= k(\boldsymbol{\eta}, \gamma; \delta \boldsymbol{u}) \\ \delta_{c_\gamma} R &= k_\gamma(\boldsymbol{\eta}, \gamma; \delta c_\gamma) + d_\gamma(\boldsymbol{\eta}, \gamma; \delta \dot{c}_\gamma) \, . \end{aligned} \tag{4.7}$$

The form k and k_γ describe the mechanical and chemical tangent stiffness resulting from the variation of the weak form in the direction of the virtual displacement $\delta \boldsymbol{u}$ and the virtual concentration change δc_γ. Furthermore, d_γ is the chemical tangential damping which becomes relevant with the variation of the weak form in the direction of the virtual velocity change of the concentration $\delta \dot{c}_\gamma$. Since no mechanical damping and no mass inertia are generated in the course of this work, these parts are not listed here. An effective tangent stiffness is introduced, including the mechanical and chemical stiffness as well as the chemical damping with

$$k_{\text{eff}} = k + k_\gamma + d_\gamma \, . \tag{4.8}$$

The following partial variations are based on the variations introduced in Appendix A.1. First, the tangential stiffness k and k_γ follow with

$$\delta_u R = \delta_u R_u + \delta_u R_{c_\gamma} \qquad \text{and} \qquad \delta_{c_\gamma} R = \delta_{c_\gamma} R_u + \delta_{c_\gamma} R_{c_\gamma} \, , \tag{4.9}$$

which are composed of the partial variations regarding the mechanical part R_u and chemical part R_{c_γ} of the weak form. The partial variations of the mechanical part of the weak formulation lead to $\delta_u R_u$ and $\delta_{c_\gamma} R_u$, i.e.

$$\begin{aligned} \delta_u R_u &= \int\limits_{\Omega_0} [\delta_u \mathbf{S}_K : \delta_u \mathbf{E} + \mathbf{S}_K : \delta_u^2 \mathbf{E}] \, \mathrm{d}V \\ &= \int\limits_{\Omega_0} [[\mathbb{C} : \operatorname{sym}(\mathbf{F}^{\mathrm{T}} \operatorname{Grad} \delta \boldsymbol{u})] : \operatorname{sym}(\mathbf{F}^{\mathrm{T}} \operatorname{Grad} \boldsymbol{\eta}) \\ &\qquad + \mathbf{S}_K : \operatorname{sym}(\operatorname{Grad}^{\mathrm{T}} \delta \boldsymbol{u} \operatorname{Grad} \boldsymbol{\eta})] \, \mathrm{d}V \\ \delta_{c_\gamma} R_u &= \int\limits_{\Omega_0} \delta_{c_\gamma} \mathbf{S}_K : \delta_u \mathbf{E} \, \mathrm{d}V \\ &= \int\limits_{\Omega_0} \mathbf{C}_\gamma \, \delta c_\gamma : \operatorname{sym}(\mathbf{F}^{\mathrm{T}} \operatorname{Grad} \boldsymbol{\eta}) \, \mathrm{d}V \, , \end{aligned} \tag{4.10}$$

wherein Eq. (3.28) and Appendix A.1.2 are considered. The partial variations of the weak formulation for the balance of mass are also introduced. First, with respect to the concentrations $\delta_{c_\gamma} R_{c_\gamma}$, which is derived with

$$\begin{aligned} \delta_{c_\gamma} R_{c_\gamma} &= \int\limits_{\Omega_0} (J\, \delta_{c_\gamma} \dot{c}_\gamma\, \gamma \,-\, \delta_{c_\gamma} \boldsymbol{J}_\gamma \cdot \operatorname{Grad} \gamma)\, \mathrm{d}V \\ &= \int\limits_{\Omega_0} (J\, \frac{\partial \dot{c}_\gamma}{\partial c_\gamma}\, \delta c_\gamma\, \gamma \,+\, J\, D \operatorname{Grad} \delta c_\gamma\, \mathbf{C}^{-1} \,\cdot\, \operatorname{Grad} \gamma)\, \mathrm{d}V\,. \end{aligned} \tag{4.11}$$

Applying Eq. (A.31). Second, with respect to the displacements $\delta_u R_{c_\gamma}$, i.e.

$$\begin{aligned} \delta_u R_{c_\gamma} &= \int\limits_{\Omega_0} (\delta_u J\, \dot{c}_\gamma\, \gamma \,-\, \delta_u \boldsymbol{J}_\gamma \cdot \operatorname{Grad} \gamma)\, \mathrm{d}V\,, \\ &= \int\limits_{\Omega_0} (J\, \mathbf{C}^{-\mathrm{T}} \,:\, \mathbf{F}^{\mathrm{T}} \operatorname{Grad} \delta \boldsymbol{u}\, \dot{c}_\gamma\, \gamma \,-\, [\mathbb{A} \,:\, \mathbf{F}^{\mathrm{T}} \operatorname{Grad} \delta \boldsymbol{u}] \cdot \operatorname{Grad} \gamma)\, \mathrm{d}V\,, \end{aligned} \tag{4.12}$$

with reference to Eq. (3.28), Eq. (3.29) and Appendix A.1.4.

4.4. Spatial Discretisation

The Bubnov-Galerkin method is used to transform the introduced continuum into a discrete problem. Therefore, the FE approach follows with

$$R(\mathbf{u}^h, c_\gamma^h, \boldsymbol{\eta}^h, \gamma^h) \,=\, 0\,, \tag{4.13}$$

wherein $\mathbf{u}^h$ and c_γ^h are the approximate solutions. The discretisation of the domain Ω is realised by a subdivision into finite elements Ω_e

$$\Omega \,\approx\, \Omega_h \,:=\, \bigcup_{\Omega_e \,\in\, \Omega_h} \Omega_e \qquad\qquad \Gamma_h \,:=\, \bigcup_{\Gamma_e \,\in\, \Gamma_h} \Gamma_e\,, \tag{4.14}$$

with $\bigcup$ describing the union of the elements. Thus, a general function f in the reference configuration is approximated by

$$\int\limits_{\Omega_0} f \mathrm{d}V \,=\, \sum_{\mathrm{e}=1}^{\mathrm{nel}} \int\limits_{\Omega_e} f_{\mathrm{e}}\, \mathrm{d}V\,, \tag{4.15}$$

where nel denotes the number of elements.

The space discretisation is realised by the isoparametric concept, which is based on approximating geometry $\mathbf{X}^h$, displacement $\mathbf{u}^h$ and concentrations c_γ^h by the same set of ansatz functions $h^I(\boldsymbol{\xi})$, so that

$$\mathbf{X}^h := \sum_{I=1}^{\text{nn}} h^I(\boldsymbol{\xi})\,\mathbf{X}^I \qquad \mathbf{u}^h := \sum_{I=1}^{\text{nn}} h^I(\boldsymbol{\xi})\,\mathbf{u}^I \qquad c_\gamma^h := \sum_{I=1}^{\text{nn}} h^I(\boldsymbol{\xi})\,c_\gamma^I\,, \tag{4.16}$$

wherein $\boldsymbol{\xi}$ represents the local coordinates. The Gaussian quadrature integration scheme is used to calculate the integrals as the standard for the FEM. Literature on the isoparametric concept can be taken from, e.g. [131]. The discrete form of the test functions for displacement $\boldsymbol{\eta}^h$ and for concentrations γ^h as well as for discrete variations $\delta\mathbf{u}^h$ and δc_γ^h, result in

$$\begin{aligned} \boldsymbol{\eta}^h &:= \sum_{I=1}^{\text{nn}} h^I(\boldsymbol{\xi})\,\boldsymbol{\eta}^I & \gamma^h &:= \sum_{I=1}^{\text{nn}} h^I(\boldsymbol{\xi})\,\gamma^I \\ \delta\mathbf{u}^h &:= \sum_{I=1}^{\text{nn}} h^I(\boldsymbol{\xi})\,\delta\mathbf{u}^I & \delta c_\gamma^h &:= \sum_{I=1}^{\text{nn}} h^I(\boldsymbol{\xi})\,\delta c_\gamma^I\,. \end{aligned} \tag{4.17}$$

In this thesis, the numerical solution is determined by elements with eight nodes, i.e. two-dimensional Serendipity elements, see e.g. [21, 68], under plane strain conditions and nine Gauss points.

Furthermore, the definitions of the matrices applied in the discretisation process follow. First, the matrix $\mathbf{L}^I$ is introduced, it organises the variations of the ansatz function as follows

$$\mathbf{L}^I := \begin{bmatrix} h^I_{,1} \\ h^I_{,2} \end{bmatrix}. \tag{4.18}$$

The well-known Voigt notation principles are applied, marked by $[\underline{\bullet}]$, to reduce the matrices to corresponding column matrix representations. Therefore, the symmetric part of the Green-Lagrange strain tensor $\mathbf{E}$ is transformed into matrix description $\mathbf{E}$ and into Voigt notation $\underline{\mathbf{E}}$ with

$$\mathbf{E} := \begin{bmatrix} E_{11} & E_{12} \\ E_{21} & E_{22} \end{bmatrix} \qquad \underline{\mathbf{E}} := \begin{bmatrix} E_{11} & E_{22} & 2\,E_{12} \end{bmatrix}^{\mathrm{T}}. \tag{4.19}$$

Analogue result the matrices $\mathbf{S}_K$ and $\underline{\mathbf{S}}_K$ from the symmetric second Piola-Kirchhoff tensor $\mathbf{S}_K$ in

$$\mathbf{S}_K := \begin{bmatrix} S_{11} & S_{12} \\ S_{21} & S_{22} \end{bmatrix} \qquad \underline{\mathbf{S}}_K := \begin{bmatrix} S_{11} & S_{22} & S_{12} \end{bmatrix}^{\mathrm{T}}. \tag{4.20}$$

The following B-matrices are introduced to illustrate the approximation of the strain variations. Then, $\mathbf{B}_u^I$ results from the variation with respect to the displacements $\delta_u \mathbf{E}$, i.e.

$$\mathbf{B}_u^I := \begin{bmatrix} F_{11}\, h^I_{,1} & F_{21}\, h^I_{,1} \\ F_{12}\, h^I_{,2} & F_{22}\, h^I_{,2} \\ F_{11}\, h^I_{,2} + F_{12}\, h^I_{,1} & F_{21}\, h^I_{,2} + F_{22}\, h^I_{,1} \end{bmatrix}, \tag{4.21}$$

and the B-matrix $\mathbf{B}_o^I$ results in the approximation of the strain variations with respect to the geometry $\delta_X \mathbf{E}$ with

$$\mathbf{B}_o^I := \begin{bmatrix} b_1\, h^I_{,1} & b_2\, h^I_{,1} \\ b_3\, h^I_{,2} & b_4\, h^I_{,2} \\ b_1\, h^I_{,2} + b_3\, h^I_{,1} & b_2\, h^I_{,2} + b_4\, h^I_{,1} \end{bmatrix}, \tag{4.22}$$

wherein

$$\begin{aligned} b_1 &= F_{11}\, u_{1,1} + F_{21}\, u_{2,1} \qquad & b_3 &= F_{12}\, u_{1,1} + F_{22}\, u_{2,1} \\ b_2 &= F_{11}\, u_{1,2} + F_{21}\, u_{2,2} \qquad & b_4 &= F_{12}\, u_{1,2} + F_{22}\, u_{2,2}\,. \end{aligned} \tag{4.23}$$

The partial variations of the second Piola-Kirchhoff stress tensor $\delta_u \mathbf{S}_K$ and $\delta_X \mathbf{S}_K$ include the fourth-order elasticity tensor C_{ijkl}, as introduced in the continuous form in Appendix A.1.2. The tensor is symmetric in the index pairs (i,j) and (k,l); thus, it can be organised in the following matrix $\underline{\mathbf{C}}$

$$\underline{\mathbf{C}} := \begin{bmatrix} \mathbb{C}_{1111} & \mathbb{C}_{1122} & \mathbb{C}_{1112} \\ \mathbb{C}_{2211} & \mathbb{C}_{2222} & \mathbb{C}_{2212} \\ \mathbb{C}_{1211} & \mathbb{C}_{1222} & \mathbb{C}_{1212} \end{bmatrix} := \begin{bmatrix} \mathbb{C}_{11} & \mathbb{C}_{12} & \mathbb{C}_{13} \\ \mathbb{C}_{21} & \mathbb{C}_{22} & \mathbb{C}_{23} \\ \mathbb{C}_{31} & \mathbb{C}_{32} & \mathbb{C}_{33} \end{bmatrix}. \tag{4.24}$$

The same procedure is used for the third-order diffusion tensor A_{jkl}, which is introduced in Appendix A.1.4. Applying the Voigt notation and considering the symmetric index pair (k,l) leads to the following matrix $\underline{\mathbf{A}}$

$$\underline{\mathbf{A}} := \begin{bmatrix} \mathbb{A}_{111} & \mathbb{A}_{122} & \mathbb{A}_{112} \\ \mathbb{A}_{211} & \mathbb{A}_{222} & \mathbb{A}_{212} \end{bmatrix} := \begin{bmatrix} \mathbb{A}_{11} & \mathbb{A}_{12} & \mathbb{A}_{13} \\ \mathbb{A}_{21} & \mathbb{A}_{22} & \mathbb{A}_{23} \end{bmatrix}. \tag{4.25}$$

The second-order tensors $\mathbf{C}_\gamma$ and $\mathbf{C}_\mathrm{n}$ include the partial variations of the stress with respect to the concentration $\delta_{c_\gamma} \mathbf{S}_K$, respectively, to the material parameters $\delta_m \mathbf{S}_K$, as introduced in Appendix A.1.2. Related to the symmetry of the second Piola-Kirchhoff stress, the

Voigt notation results in

$$\underline{\mathbf{C}}_{\gamma} := \begin{bmatrix} C_{\gamma 11} \\ C_{\gamma 22} \\ C_{\gamma 12} \end{bmatrix} ; \qquad \underline{\mathbf{C}}_{\mathrm{n}} := \begin{bmatrix} C_{n11} \\ C_{n22} \\ C_{n12} \end{bmatrix} \text{ with } n \in \{1,2,3,4,5\} . \tag{4.26}$$

In addition to this, the matrix $\underline{\mathbf{A}}_{\gamma}$ refers to the second-order tensor $\mathbf{A}_{\gamma}$ and contains the variation of the concentration flux with respect to the geometry derived in Appendix A.1.4. Thus, the Voigt notation follows with

$$\underline{\mathbf{A}}_{\gamma} := \begin{bmatrix} A_{\gamma 11} \\ A_{\gamma 22} \\ A_{\gamma 12} \end{bmatrix} . \tag{4.27}$$

4.5. Time Integration Method

The time integration is implemented using the Newmark-beta method. Within the coupled problem, the concentrations are time-dependent. In the current time step, the concentration, the velocity of the concentrations and the acceleration of the concentration are represented with $\{c_{\gamma},\, \dot{c}_{\gamma},\, \ddot{c}_{\gamma}\}$, whereas in the previous time step, the notation $\{c_{\gamma\mathrm{N}},\, \dot{c}_{\gamma\mathrm{N}},\, \ddot{c}_{\gamma\mathrm{N}}\}$ are used. Within the considered time interval, a constant average acceleration of the concentrations $\ddot{c}_{\beta}$ is introduced with

$$\ddot{c}_{\beta} := \tfrac{1}{2} \left(\ddot{c}_{\gamma\mathrm{N}} + \ddot{c}_{\gamma} \right) , \tag{4.28}$$

with the acceleration to be approximated in the present time step $\ddot{c}_{\gamma}$ and the previous acceleration of the concentrations $\ddot{c}_{\gamma\mathrm{N}}$. The Newmark-beta method states that the approximations of the velocity $\dot{c}_{\gamma}$ and acceleration $\ddot{c}_{\gamma}$ are based on

$$\begin{aligned} \dot{c}_{\gamma} &= \dot{c}_{\gamma\mathrm{N}} + \Delta\mathrm{t}\, \ddot{c}_{\beta} \\ c_{\gamma} &= c_{\gamma\mathrm{N}} + \Delta\mathrm{t}\, \dot{c}_{\gamma\mathrm{N}} + \frac{1}{2} \Delta\mathrm{t}^{2}\, \ddot{c}_{\beta} , \end{aligned} \tag{4.29}$$

where $\Delta\mathrm{t}$ is the time increment. Finally, the approximation of the velocity for the concentrations $\dot{c}_{\gamma}$ in the present time step can be derived with

$$\dot{c}_{\gamma} = \frac{2}{\Delta\mathrm{t}} \left(c_{\gamma} - c_{\gamma\mathrm{N}} \right) - \dot{c}_{\gamma\mathrm{N}} . \tag{4.30}$$

The coupled model in this work is independent of acceleration processes. Thus, the required partial variations of the Newmark-beta approach read

$$\frac{\partial \dot{c}_\gamma}{\partial c_\gamma} = \frac{2}{\Delta \mathrm{t}}\,, \quad \frac{\partial \dot{c}_\gamma}{\partial c_{\gamma \mathrm{N}}} = -\frac{2}{\Delta \mathrm{t}} \quad \text{and} \quad \frac{\partial \dot{c}_\gamma}{\partial \dot{c}_{\gamma \mathrm{N}}} = -1\,. \tag{4.31}$$

Furthermore, the element history field column matrix $\tilde{\mathbf{h}}^e \in \mathbb{R}^{72}$ is introduced at this point. The history field contains information about the primary variables as well as the velocity and acceleration of the primary variables from the previous time step so that the following column matrix is defined with

$$\tilde{\mathbf{h}}^e := \sum_{I=1}^{\mathrm{nn}} \begin{bmatrix} \mathbf{u}^I_\mathrm{N} & c^I_{\gamma\mathrm{N}} & \dot{\mathbf{u}}^I_\mathrm{N} & \dot{c}^I_{\gamma\mathrm{N}} & \ddot{\mathbf{u}}^I_\mathrm{N} & \ddot{c}^I_{\gamma\mathrm{N}} \end{bmatrix}^\mathrm{T}. \tag{4.32}$$

4.6. Discretisation of the Weak Formulations

In the following, the approximations of Sec. 4.5 are introduced into the weak form referring to Eq. (4.2). For this reason, the weak formulation of the balance of momentum follows with

$$R^h_u = \sum_{I=1}^{\mathrm{nn}} (\boldsymbol{\eta}^I)^\mathrm{T} \left[\int\limits_{\Omega_e} (\mathbf{B}^I_u)^\mathrm{T}\, \underline{\mathbf{S}}_K \,\mathrm{d}V - \mathbf{F}^I_e \right] = \sum_{I=1}^{\mathrm{nn}} (\boldsymbol{\eta}^I)^\mathrm{T}\, \mathbf{R}^I_u\,, \tag{4.33}$$

wherein the external load is introduced in a column matrix with $\mathbf{F}^I_e \in \mathbb{R}^2$ containing nodal forces. The sub-column matrix $\mathbf{R}^I_u \in \mathbb{R}^2$ is introduced. Furthermore, the discretisation of the weak formulation of the balance of mass for the concentration, cf. Eq. (4.4), follows with

$$R^h_{c_\gamma} = \sum_{I=1}^{\mathrm{nn}} \gamma^I \left[\int\limits_{\Omega_e} (h^I\, \dot{c}_\gamma\, J - (\mathbf{L}^I)^\mathrm{T}\, \mathbf{J}_\gamma) \,\mathrm{d}V - J^I_{\gamma e} \right] = \sum_{I=1}^{\mathrm{nn}} \gamma^I\, R_{c_\gamma}\,, \tag{4.34}$$

including the external scalar $J^I_{\gamma e}$, which contains the nodal flux term. The components are gathered together in the scalar $R^I_{c_\gamma}$ and the element residuum $\mathbf{R}^e \in \mathbb{R}^{24}$ results after summation of the nodes in

$$\mathbf{R}^e = \sum_{I=1}^{\mathrm{nn}} \begin{bmatrix} \mathbf{R}^I_u \\ R^I_{c_\gamma} \end{bmatrix}, \tag{4.35}$$

assuming eight nodes per element. The external contribution of the flux and forces are assumed to be deformation and concentration-independent.

4.7. Discrete Tangential Stiffness

The effective tangential stiffness from Eq. (4.8) is required to solve the structural problem using the Newton-Raphson method. Therefore, the effective stiffness matrix $\mathbf{K}^e$ is successively assembled from the sub-matrices $\mathbf{K}_1^{IJ}, \mathbf{K}_2^{IJ}, \mathbf{K}_3^{IJ}$ and K_4^{IJ}. First, $\mathbf{K}_1^{IJ} \in \mathbb{R}^{2\times 2}$ is derived from the variation of the mechanical part of the weak formulation with respect to the displacement from Eq. (4.10.1) in the discrete form, i.e.

$$\begin{aligned} \delta_u R_u^h &= \sum_{I=1}^{\mathrm{nn}} \sum_{J=1}^{\mathrm{nn}} (\boldsymbol{\eta}^I)^{\mathrm{T}} \left[\int_{\Omega_e} ((\mathbf{L}^I)^{\mathrm{T}} \mathbf{S}_K \, \mathbf{L}^J \, \mathbf{1} \, + \, (\mathbf{B}_u^I)^{\mathrm{T}} \, \underline{\mathbf{C}} \, \mathbf{B}_u^J) \, \mathrm{d}V \right] \delta \mathbf{u}^J \\ &= \sum_{I=1}^{\mathrm{nn}} \sum_{J=1}^{\mathrm{nn}} (\boldsymbol{\eta}^I)^{\mathrm{T}} \quad \mathbf{K}_1^{IJ} \, \delta \mathbf{u}^J \, . \end{aligned} \tag{4.36}$$

Additionally, the discretisation for the mechanical weak formulation with respect to the concentrations referring to Eq. (4.10.2) leads to the column matrix $\mathbf{K}_2^{IJ} \in \mathbb{R}^2$, such that

$$\begin{aligned} \delta_{c_\gamma} R_u^h &= \sum_{I=1}^{\mathrm{nn}} \sum_{J=1}^{\mathrm{nn}} (\boldsymbol{\eta}^I)^{\mathrm{T}} \left[\int_{\Omega_e} (\mathbf{B}_u^I)^{\mathrm{T}} \, \underline{\mathbf{C}}_\gamma \, h^J \, \mathrm{d}V \right] \delta c_\gamma^J \\ &= \sum_{I=1}^{\mathrm{nn}} \sum_{J=1}^{\mathrm{nn}} (\boldsymbol{\eta}^I)^{\mathrm{T}} \quad \mathbf{K}_2^{IJ} \, \delta c_\gamma^J \, . \end{aligned} \tag{4.37}$$

However, the row matrix $\mathbf{K}_3^{IJ} \in \mathbb{R}^{1\times 2}$ results from the partial variation of the chemical weak formulation with respect to the displacements from Eq. (4.12) with

$$\begin{aligned} \delta_u R_{c_\gamma}^h &= \sum_{I=1}^{\mathrm{nn}} \sum_{J=1}^{\mathrm{nn}} \gamma^I \quad \left[\int_{\Omega_e} (h^I \, J \, \dot{c}_\gamma \, (\mathbf{L}^J)^{\mathrm{T}} \, \mathbf{C}^{-\mathrm{T}} \, \mathbf{F}^{\mathrm{T}} \, - \, (\mathbf{L}^I)^{\mathrm{T}} \, \underline{\mathbf{A}} \, \mathbf{B}_u^J) \, \mathrm{d}V \right] \delta \mathbf{u}^J \\ &= \sum_{I=1}^{\mathrm{nn}} \sum_{J=1}^{\mathrm{nn}} \gamma^I \quad \mathbf{K}_3^{IJ} \, \delta \mathbf{u}^J \, . \end{aligned} \tag{4.38}$$

Herein, the index notation is used to clarify the connections, i.e.

$$(\delta_u R_{c_\gamma}^h)_o = \sum_{I=1}^{\mathrm{nn}} \sum_{J=1}^{\mathrm{nn}} \gamma^I \left[\int_{\Omega_e} (h^I \, J \, \dot{c}_\gamma \, L_{,p}^J \, C_{np}^{-1} \, F_{on} \, + \, L_{,t}^I \, L_{,n}^J \, A_{tpn} \, F_{op}) \, \mathrm{d}V \right] \delta u_o^J \, . \tag{4.39}$$

The discretisation of the partial variation of the chemical weak formulation with respect to the concentrations, derived in Eq. (4.11), is illustrated with

$$\begin{aligned} \delta_{c_\gamma} R_{c_\gamma}^h &= \sum_{I=1}^{\mathrm{nn}} \sum_{J=1}^{\mathrm{nn}} \gamma^I \quad \left[\int_{\Omega_e} (h^I \, J \, \frac{2}{\Delta \mathrm{t}} \, h^J \, + \, (\mathbf{L}^I)^{\mathrm{T}} \, J \, D \, \mathbf{C}^{-1} \, \mathbf{L}^J) \, \mathrm{d}V \right] \delta c_\gamma^J \\ &= \sum_{I=1}^{\mathrm{nn}} \sum_{J=1}^{\mathrm{nn}} \gamma^I \quad K_4^{IJ} \, \delta c_\gamma^J \, , \end{aligned} \tag{4.40}$$

wherein the partial variation from the Newmark-beta approach, cf. Eq. (4.31.1), is used with the time increment Δt. The scalar K_4^{IJ} can be evaluated with one entry per node. Therefore, the effective element stiffness matrix $\mathbf{K}^e \in \mathbb{R}^{24\times 24}$ results with

$$\mathbf{K}^e = \sum_{I=1}^{\mathrm{nn}} \sum_{J=1}^{\mathrm{nn}} \begin{bmatrix} \mathbf{K}_1^{IJ} & \mathbf{K}_2^{IJ} \\ \mathbf{K}_3^{IJ} & K_4^{IJ} \end{bmatrix} . \tag{4.41}$$

The summation refers to eight nodes per element and three degrees of freedom.

4.8. Numerical Implementation for Structural Analysis

The numerical applications of the discrete formulations for the residuals and tangents, derived in this section, are illustrated in the Algorithm 1. The matrices are represented at the element level so that an assembly must take place within the framework of numerical implementation, i.e.

$$\mathbf{R} = \bigcup_{e=1}^{\mathrm{nel}} \mathbf{R}^e \qquad \text{and} \qquad \mathbf{K} = \bigcup_{e=1}^{\mathrm{nel}} \mathbf{K}^e , \tag{4.42}$$

wherein nel denotes the total number of elements. Moreover, the dimensions $\mathbf{R} \in \mathbb{R}^{\mathrm{dof}}$ and $\mathbf{K} \in \mathbb{R}^{\mathrm{dof}\times\mathrm{dof}}$ result with dof referring to the global number of degrees of freedom. The algorithm illustrates the calculation of the primary variables applying the iterative Newton-Raphson method. The primary variables are summarised in the global column matrix $\boldsymbol{\nu} \in \mathbb{R}^{\mathrm{dof}}$ with

$$\boldsymbol{\nu} = \begin{bmatrix} \mathbf{u} & \mathbf{c}_\gamma \end{bmatrix}^{\mathrm{T}} , \tag{4.43}$$

$\mathbf{u} \in \mathbb{R}^{\mathrm{dofm}}$ includes the overall nodal displacements and $\mathbf{c}_\gamma \in \mathbb{R}^{\mathrm{dofc}}$ describes the overall nodal concentrations with dofm describing the global number of mechanical degrees of freedom and dofc referring to the global number of chemical degrees of freedom.

4.9. Concluding Remarks for the Numerical Model

In this section, all necessary equations for the structural analysis problem's implementation and solution are provided. The concept for the numerical solution can be summarised in the following key points:

- *Weak forms of the balance equations, including the constitutive laws, are outlined.*
- *Linearisation of the weak form is derived for the nonlinear problem's solution via the Newton-Raphson method.*
- *Spatial discretisation: with the Bubnov-Galerkin method, the introduced continuum is transferred into a discrete problem. The isoparametric concept enables the same ansatz to approximate the mechanical and chemical equations with an element description of eight nodes. The Gaussian quadrature integration scheme is utilised.*
- *Time integration method: The Newmark-beta method approximates the time-dependent evolution of the concentrations.*
- *Preparation of the essential matrix representations for the numerical implementation of the structural analysis problem.*

5. Structural Optimisation

This section presents how the developed continuum mechanical model is linked to the well-known mathematical structural optimisation methods. Therefore, this section introduces structural optimisation. Both the insight into the literature is given as well as an outline of the approaches relevant for this work. An overview of structural optimisation is given with further details of the parameterised geometric representation and the mathematical solver needed for the applied shape and material parameter optimisation.

5.1. Introduction to Structural Optimisation

Optimisation problems can occur in various fields, e.g. production processes can be optimised, the shortest possible distance between locations can be found, or the most favourable price of a product can be determined. Structural optimisation refers to optimising mechanical structures and defining mathematical problems solved by simulation-based calculations. The task of structural optimisation can be formulated as follows: specific modifications of certain parameters can find the best possible solution for a structural-mechanical problem. Mathematical algorithms are applied to get optimal solutions, thus determining the change of parameters via iteration loops and ascertain the structural response. In order to set up a structural problem, some basic expressions are introduced:

- *Objective function* $\tilde{J}$
  The objective function is a mathematical function that describes the structural optimisation problem, e.g. volume, stiffness of a structure as well as stress or displacement functions.

- *Design parameters* $\tilde{s}$
  The design parameters are the alterable variables of the structure, where the number of independent design parameters determines the dimension of the optimisation problem.

- *Constraints $\tilde{g}$*
  The constraints restrict the optimisation solution with equality or inequality constraints. For example, equilibrium, stress and displacement conditions as well as stability conditions, can be introduced.

Shape optimisation is one focus of this work. Geometric design parameters are introduced to optimise the initial shape of the structure. This minimises the defined objective function while maintaining the given boundary conditions and provides new design parameters. Within the framework of structural analysis, the Computer-Aided Geometric Design (CAGD) approach is then used to create the FE-mesh. Thus, the parameterised structure geometry can be updated in each optimisation step. Further to this, parameter optimisation is then used to calculate the mechanical-chemical-degradation model's material parameters that lead to a desired result. For example, it is possible to determine the material parameters that reduce material degradation to a maximum permissible level within a defined period.

Both optimisation approaches, shape and material parameter optimisation are presented in this thesis for the proposed mechanical-chemical-degradation model. This model is then integrated into an optimisation algorithm. The mathematical optimisation is based on algorithms for structural optimisation, i.e. nonlinear constrained optimisation problems or nonlinear least-square problems. By integrating the derived structural analysis and sensitivity analysis of diffusion-driven and time-dependent degradation processes coupled with a mechanical structure: the harmful effects of chemical concentrations and the associated degradation processes can be redefined and the structure optimised.

5.2. State-of-the-Art for Presumptions on Structural Optimisation

5.2.1. Types of Structural Optimisation

The following types of structural optimisation (that are to be considered in combination) can fundamentally be named as:

- *Size optimisation,*
- *Shape optimisation,*
- *Topological optimisation,*
- *Parameter identification.*

A survey on the different variants of optimisation, the state-of-the-art technology, as well as a comparison between the different mathematical programming methods, is given in the literature, e.g. [33, 119, 5, 100]. Within the context of this thesis, it should be noted that shape optimisation is addressed to optimise the geometry and that a curve-fitting algorithm, which is often used for parameter identifications, is applied to optimise material parameters.

Size optimisation maintains the structure's shape and topology and can be described as the most direct approach to optimal solutions. Only a few parameters are defined as design parameters that can change: cross-sections, wall thickness or the thickness of the FEs. As a result, the calculation of sensitivities is more straightforward to realise than an optimisation problem in the framework of shape or topology optimisation. Examples for recent applications can be found, e.g. in [38, 44, 39, 74], where dimensioning problems are primarily used in combination with different types of structural optimisation.

Within the framework of *shape optimisation*, an initial shape is optimised by changing the outer contour to reduce weight or volume, for instance. Thereby the demanding task of mesh adaptation during the iteration process must be considered. In particular, problems can occur due to the destruction of the mesh, jagged boundaries or a considerable number of design parameters. To avoid the problems, a strategy for updating the geometric modelling must be selected accordingly. The first publications from the 1950s deal with weight reduction in aerospace, presented by Hemp [64] and Cox [36]. Presently, shape optimisation is still a widespread field of research, particularly regarding research related to the aerospace and automotive industry striving for improved approaches for shape optimisation. Current works are, e.g. [144, 141, 71].

Topology optimisation includes design parameters that describe the location and arrangement of structural elements, e.g. number, size, shape and the position of holes and inclusions. The optimal combination of material areas as well as the global shape can be determined during this optimisation. An introduction to topology optimisation can be found, for example, in [18, 17]. Michell developed the first topological optimisation problem in 1904, see [93], where he calculated the optimum arrangement of tension and compression members in a mechanical structure. As the result of his findings, analytical optimal procedures were then able to be further developed in the 1980s within the framework of topology optimisation [111]. The difficulty of topology optimisation lies mainly in the high number of design parameters, chequerboard patterns and mesh dependencies. This field, therefore, remains a predominant field of study where many techniques continue to be developed to solve such challenges, to name a few [104, 112, 121, 4].

Parameter identification, a mathematically inverse problem, involves determining parameters that can optimally simulate a measured process. The parameter identification can be used to achieve the desired result by applying curve-fitting algorithms and adjusting the established differential equations' parameters. As a result, this process can optimise material parameters. This method is often applied in different research topics. It is advantageous in the context of flow and transport processes to understand and influence flow characteristics (see [59]). Parameter identification is additionally used for machine control, as the accuracy of the machine parameters has a considerable influence on efficiency [103]. It can be applied to dynamic processes, such as the simulation of the 2019-nCoV eruption, by reconstructing parameters needed to predict the process, see [27]. Applications of parameter identification within the framework of structural analysis are published in the following publications [89, 76, 90].

5.2.2. Geometric Modelling

The strategy of parameterisation in shape optimisation is an important aspect, for which a brief insight into the literature is given below. Thus, the strategy has a considerable influence on the choice of design parameters and should be chosen depending on the optimisation task. Common approaches are:

- *CAGD-based parametrisation,*
- *Mesh-based parametrisation,*
- *Parameter-free technique,*

for detailed explanations see, e.g. [119]. The CAGD-based shape optimisation is applied in the framework of this thesis. Nevertheless, the state-of-the-art alternative methods are mentioned here, i.e. mesh-based parametrisation and parameter-free techniques.

Computer-Aided Geometric Design (CAGD) is a mathematical approach for describing geometric objects and their transfer to computer graphics. Curves, surfaces and volumes, are applied and algorithms are generated to create, analyse and manipulate geometric structures. The origins of the CAGD date back to the 1960s. The theory of Bézier lines was developed independently by P. de Casteljau and P. Bézier and has been further studied over the years. Farin present in [42] a detailed overview of the application of CAGD, the theoretical origin and further developments. Moreover, Knez et al. provide an overview of the current status of CAGD applied to geometric designs, see [77]. The integration of CAGD into the shape optimisation process offers high flexibility for modifications with low utilisation of design parameters, as Braibant et al. show in [25] using B-Splines as design parameters. Furthermore, the parametrisation of shape optimisation is demonstrated on airfoils and 3D wind turbine blades by the adaptive composition of low order Bézier curves and surfaces to complex geometries, see [137].

The *CAGD-based parametrisation* is an efficient method that provides a basis for selecting design parameters, such as control points or dimensions, such as lengths of lines and axes of ellipses and circles. However, the FE-mesh has to be re-meshed in every iteration step. In order to ensure fully automated shape variation, automatic meshing with the transfer of the updated design parameters must be implemented.

An alternative approach to achieve parametric shape optimisation is *mesh-based parameterisation*, in which an existing FE-mesh is manipulated. The so-called 'morphing technology' enables a smooth variation of the FE-nodes. Initially, the idea of morphine derived from visual effects in film and television with smooth transitions between digital images, an overview of image morphine is presented in [139]. The idea of rapid image change is transferred to the parameterisation of existing FE-meshes in the context of shape optimisation, see [107]. With the commonly used box-morphing approach, the modifiable nodes are positioned within a predefined box. Using CAGD objects, such as B-Splines, this method can be applied to define the Box. A mapping algorithm is used to calculate the change of the FE-nodes depending on the design parameters. In [52], the inverse calculation of FE-nodes based on such mapping functions is explained and examples of the application of morphing-box based parameterisation for shape optimisation are shown. Further applications of the morphing-box approach can be found in the literature, [73, 115, 66, 88]. In regards to complex models, morphine is notably a more powerful alternative to the CAGD-based approach. It combines the advantage of requiring fewer design parameters and no re-meshing. The advantages are pointed out in [26, 127].

With the *parameter-free technique* the coordinates of the FE-mesh are selected as design parameters. Thus, the approach does not require integrating the CAGD and only requires the standard post-processing tools within the Finite Element Analysis (FEA) framework. This approach's obvious disadvantage is a high number of design parameters, causing difficulties such as jagged boundaries or destroyed FE-meshes. Those drawbacks are outline among others in [60]. Subsequently, Scherer et al. avoid the problems of jagged edges by applying a fictive energy approach, see [118]. Relative works show the efficiency of filter techniques, which improve the FE-mesh quality in free-form optimisation processes, e.g. [43, 22]. More publications [53, 82, 118] prove the successful application of the parameter-free optimisation.

5.2.3. Structural Optimisation of Degradation Processes

Structural optimisation, often applied to growth or degradation processes, is traditionally solved by evolutionary optimisation algorithms; see [123] for details. The evolution models are based on the concept of gradually removing inefficient material from a structure. The disadvantage of the evolutionary concepts is that optimisation starts from one defined reference configuration and that the result quickly ends in local minima. Resulting in the inability to find an optimal solution with a single evolutionary algorithm, see [136]. The application of mathematical based structural optimisation to growth or degradation processes could help solve the problem; however, it has not yet been sufficiently investigated. Similar to the embedding of a growth approach in an optimisation algorithm, shape and topology optimisations are applied to damage models. For example, an optimal damage distribution is computed with a shape optimisation algorithm that embeds an isotropic gradient enhanced damage model, see [57]. [130] present a topology optimisation method connected to a fatigue model. The model enables the computation of optimised topologies, taking fatigue at high cycles as a limiting condition into account. [101] develop a level set-based topology optimisation framework to reduce damage in the context of structural design.

5.3. Procedure for Structural Optimisation

In general, the process of structural optimisation is identical for all types of optimisation and is schematically illustrated in Figure 5.1. The structural optimisation process used in this thesis is described in more detail in the following section.

In the first step, the boundary value problem and the optimisation problem are initialised. Signifying that the geometry model with the FE-mesh, material parameters, boundary conditions and loads must be transferred and that the objective function, constraints and design parameters are defined. The geometry parameters are specified as design parameters within the scope of shape optimisation. For this reason, the geometry model is structured parametrically with a CAGD-based approach.

The structural analysis of the mechanical-chemical-degradation approach is carried out using the numerical approximation method FEM with the given once inputted. Within this given information, the deformation of the body, stresses and concentration distributions are calculated and the variational sensitivity analysis is thus, carried out. In the context of the sensitivity analysis, the derivatives of the objective function and constraints with respect to design changes are calculated. The variational sensitivity analysis provides first the gradients of the continuous problem according to the design parameters. It then offers discretisation in space and time according to the numerical approximation method. Thus, structural analysis and sensitivity analysis can be performed concurrently with the integrated continuum mechanical formulation. For this purpose, the continuum mechanical quantities must be extended by the dependency of the design parameters, e.g. geometry parameters.

The information from the sensitivity analysis provides the objective function, the constraints, their derivatives are therefore, passed on to the mathematical optimiser. In this thesis, the MATLAB toolbox is used to perform the mathematical optimisation, i.e. minimising the defined objective function while maintaining the given constraints and providing new design parameters.

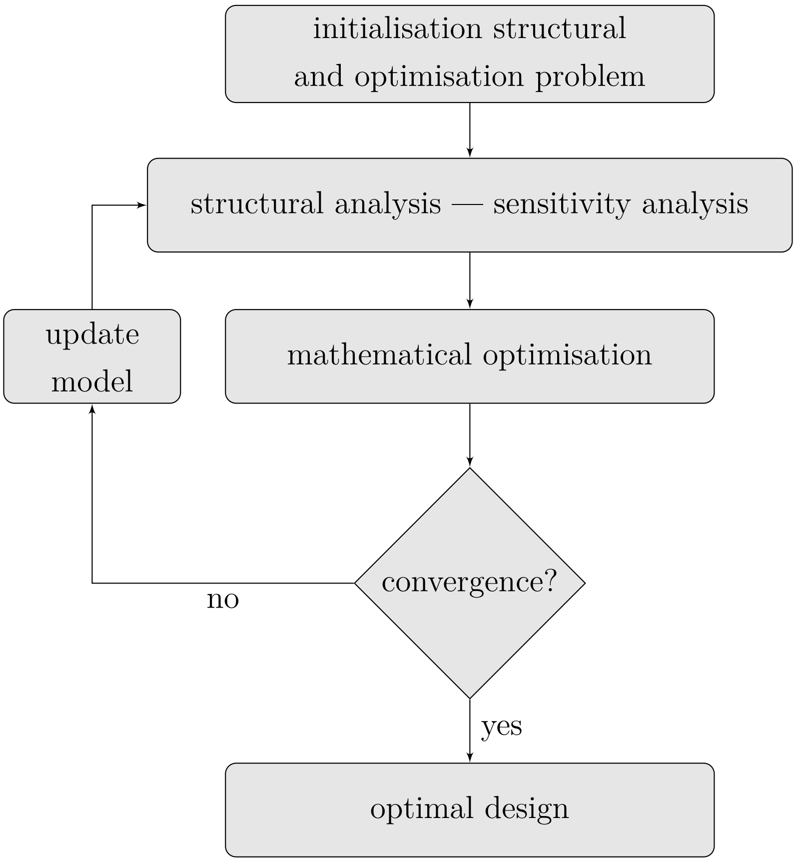

Figure 5.1.: Process of the optimisation problem.

With the new design parameters, the mechanical model is updated and the quality of the structure is examined. The criteria specified by the user is checked. Finally, the continuum's balance is ensured for the new design parameters. If the criteria are not met, the CAGD model is automatically updated and the algorithm repeats itself until the desired quality of the structure is achieved. The algorithm provides an improved design.

5.4. Parameterised Geometry

In this thesis, CAGD is applied to generate the FE-mesh of the desired geometry required for structural analysis and select design parameters as the coordinates of control points for shape optimisation. In this mathematical approach, geometries are described by lines, curves and surfaces. Approximation methods for curves and surfaces enable soft and smooth geometries. The standard approximation methods of curves are named. Thus, Bézier lines, rational curves, B-Splines and NURBS are approximation methods for polygons. The Bézier lines approximate control polygons with n+1 control points by a curve of degree n. The same applies to rational curves, whereby a weighting value is assigned to the control polygon points so that the course of the curve can be influenced. The B-splines compose the curve by segments and thus, enable local changes of the parameters; the curve's degree is arbitrary. The strategy behind NURBS is similar to the B-Splines, yet here again, the individual control nodes' weighting value can be used. It should be mentioned that the same methods are used to generate surfaces, only with higher dimensions.

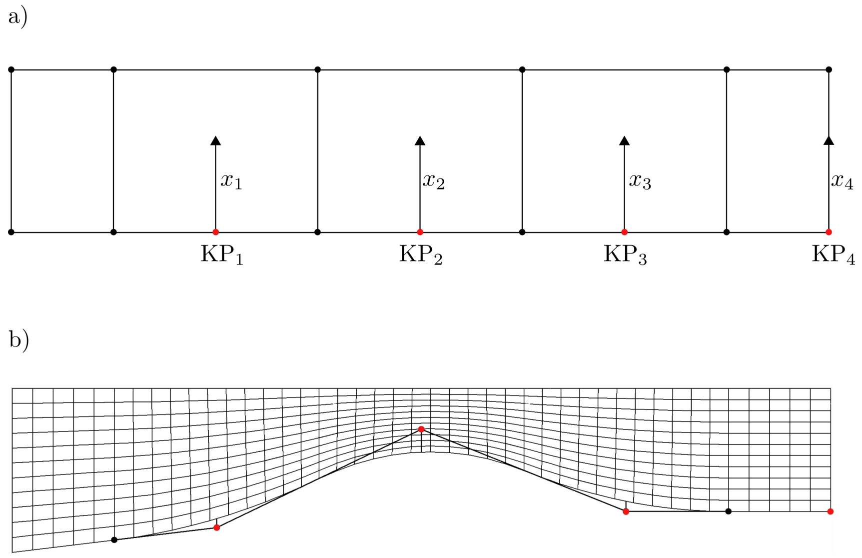

Figure 5.2.: a) CAGD geometry via points, lines, key points (KP$_n$) and B-Splines. b) FE-mesh in dependency of parametric key points.

In this thesis, the program Gmsh is applied to create the geometries based on these approximations and generate an FE-mesh. The control nodes are set as design parameters for shape optimisation. Therefore, CAGD-based access enables parameterised geometry with mesh manipulation. The advantage of an approach with a relatively small number of design parameters becomes visible in Figure 5.2. The CAGD geometry is created by defined points, lines and a B-spline function for the lower edge of the structure. The B-spline function is dependent on the given control points (KP$_n$), the design parameters, to create a curve for the lower edge of the structure. A change of these design parameters leads to the manipulation of the FE-mesh.

5.5. Mathematical Optimisation

Due to the widespread use of mathematical optimisation, a more precise literary classification is not given here and therefore, only a few references are mentioned, such as [100, 48, 100]. This thesis addresses restricted optimisation problems. As a result, the solution method of Sequential Quadratic Programming (SQP) for such problems is introduced. Where an inverse analysis for the optimisation of material parameters is derived, the mathematical method of nonlinear least-squares is presented. In the following subsections, reference is made to the nomenclature introduced in this thesis and the abbreviation listed therein are applied for the mathematical solver.

5.5.1. Nonlinear Constrained Optimisation Problems

The mathematical description of a general restricted minimisation problem follows with

$$\begin{array}{llrclll} \min \tilde{J}(\tilde{\boldsymbol{s}}) & \text{subject to} & \tilde{h}_j(\tilde{\boldsymbol{s}}) & = & 0 & \text{with} & j \in \{1,\dots,m_h\} \\ \tilde{\boldsymbol{s}} \in \mathbb{R}^{n_s} & & \tilde{g}_k(\tilde{\boldsymbol{s}}) & \leq & 0 & \text{with} & k \in \{1,\dots,m_g\} \\ & & \tilde{s}_i^l & \leq & \tilde{s}_i \leq \tilde{s}_i^u & \text{with} & i \in \{1,\dots,n_s\}\,, \end{array} \tag{5.1}$$

wherein the following quantities correspond to

$$\begin{array}{lcllllll} \tilde{J} & : & \mathbb{R}^{n_s} & \to & \mathbb{R} & & & \text{objective function} \\ \tilde{h}_j & : & \mathbb{R}^{n_s} & \to & \mathbb{R}, & j & \in \{1,\dots,m_h\} & \text{equality constraints} \\ \tilde{g}_k & : & \mathbb{R}^{n_s} & \to & \mathbb{R}, & k & \in \{1,\dots,m_g\} & \text{inequality constraints,} \end{array} \tag{5.2}$$

as well as

$$\begin{array}{ll} \tilde{\boldsymbol{s}} = \left[\tilde{s}_1,\dots,\tilde{s}_{n_s}\right]^{\mathrm{T}} & \text{design parameters} \\ \text{with} & \\ \tilde{s}_i^l,\ \tilde{s}_i^u,\ i \in \{1,\dots,n_s\} & \text{lower and upper bounds}\,. \end{array} \tag{5.3}$$

A finite number of equality and inequality constraints as well as upper and lower design parameters, are introduced in the following notation, which may also be presented as empty depending on the given problem,

$$\tilde{\boldsymbol{h}}(\tilde{\boldsymbol{s}}) = \begin{bmatrix} \tilde{h}_1(\tilde{\boldsymbol{s}}) \\ \vdots \\ \tilde{h}_{m_h}(\tilde{\boldsymbol{s}}) \end{bmatrix}, \quad \tilde{\boldsymbol{g}}(\tilde{\boldsymbol{s}}) = \begin{bmatrix} \tilde{g}_1(\tilde{\boldsymbol{s}}) \\ \vdots \\ \tilde{g}_{m_g}(\tilde{\boldsymbol{s}}) \end{bmatrix}, \quad \tilde{\boldsymbol{s}}^l = \begin{bmatrix} \tilde{s}^l_1 \\ \vdots \\ \tilde{s}^l_{n_s} \end{bmatrix} \text{ and } \quad \tilde{\boldsymbol{s}}^u = \begin{bmatrix} \tilde{s}^u_1 \\ \vdots \\ \tilde{s}^u_{n_s} \end{bmatrix}. \tag{5.4}$$

The mathematical formulation follows in the compact notation for the general nonlinear constrained minimisation problem from Eq. (5.1), i.e.

$$\begin{array}{lllll} \min \tilde{J}(\tilde{\boldsymbol{s}}) & \text{subject to} & \tilde{\boldsymbol{h}}(\tilde{\boldsymbol{s}}) & = & \boldsymbol{0} \\ \tilde{\boldsymbol{s}} \in \mathbb{R}^{n_s} & & \tilde{\boldsymbol{g}}(\tilde{\boldsymbol{s}}) & \leq & \boldsymbol{0} \\ & & \tilde{\boldsymbol{s}}^l & \leq & \tilde{\boldsymbol{s}} \leq \tilde{\boldsymbol{s}}^u . \end{array} \tag{5.5}$$

SQP is applied to solve the nonlinear optimisation problem. Within this approach, a sequence of sub-problems is formulated under consideration of optimal conditions and application of the Newton approximation. Therefore, the nonlinear restricted optimisation problem is presented using a Lagrange formulation. For this purpose, the inequality restrictions are transformed into equality restrictions applying commonly named 'slack variables'. Besides, a complementary slackness condition is introduced as it is a necessary optimal criterion derived from the inequality constraints, i.e.

$$\mu_k \, \tilde{g}_k(\tilde{\boldsymbol{s}}) = 0, \qquad k \in \{1, \ldots, m_g\}, \tag{5.6}$$

wherein μ_k is a Lagrange parameter. According to these conditions, the Lagrange function ($L : \mathbb{R}^{n_s} \times \mathbb{R}^{m_h} \times \mathbb{R}^{m_g} \rightarrow \mathbb{R}$) follows with

$$L(\tilde{\boldsymbol{s}}, \boldsymbol{\lambda}, \boldsymbol{\mu}) := \tilde{J}(\tilde{\boldsymbol{s}}) + \sum_{j=1}^{m_h} \lambda_j \, \tilde{h}_j(\tilde{\boldsymbol{s}}) + \sum_{k=1}^{m_g} \mu_k \, \tilde{g}_k(\tilde{\boldsymbol{s}}), \tag{5.7}$$

wherein λ_j is another Lagrange parameter. The optimality conditions, including the complementary slackness condition, reads as

$$\begin{array}{lllll} \nabla_{\tilde{s}} L(\tilde{\boldsymbol{s}}, \boldsymbol{\lambda}, \boldsymbol{\mu}) & = & \boldsymbol{0} & & \\ \tilde{h}_j(\tilde{\boldsymbol{s}}) & = & 0, & j \in & \{1, \ldots, m_h\} \\ \tilde{g}_k(\tilde{\boldsymbol{s}}) & \leq & 0, & k \in & \{1, \ldots, m_g\} \\ \mu_k & \geq & 0, & k \in & \{1, \ldots, m_g\} \\ \mu_k \, \tilde{g}_k & = & 0, & k \in & \{1, \ldots, m_g\} . \end{array} \tag{5.8}$$

These specified, and necessary, optimal conditions are called Karush–Kuhn–Tucker (KKT) conditions and a point $(\tilde{\boldsymbol{s}}^*, \boldsymbol{\lambda}^*, \boldsymbol{\mu}^*)$ that complies with these conditions is called a KKT point. The total derivative of the Lagrange function $\nabla L(\tilde{\boldsymbol{s}}, \boldsymbol{\lambda}, \boldsymbol{\mu})$ can be approximated by Newton's method resulting in the representation of the following sub-problem i in the iteration point $(\tilde{\boldsymbol{s}}^i, \boldsymbol{\lambda}^i, \boldsymbol{\mu}^i)$, with

$$\begin{array}{llrcl} \min \overline{J^i}(\Delta\tilde{\boldsymbol{s}}) & \text{subject to} & \overline{\boldsymbol{h}^i}(\Delta\tilde{\boldsymbol{s}}) & = & \boldsymbol{0} \\ \Delta\tilde{\boldsymbol{s}} \in \mathbb{R}^{n_s} & & \overline{\boldsymbol{g}^i}(\Delta\tilde{\boldsymbol{s}}) & \leq & \boldsymbol{0} \\ & & (\tilde{\boldsymbol{s}}^l - \Delta\tilde{\boldsymbol{s}}^i) & \leq & \tilde{\boldsymbol{s}} \leq (\tilde{\boldsymbol{s}}^u - \tilde{\boldsymbol{s}}^i)\,. \end{array} \tag{5.9}$$

Therein, a quadratic approximation of the objective function and a linearisation of the constraints are applied, i.e.

$$\begin{aligned} \overline{J^i}(\Delta\tilde{\boldsymbol{s}}) &= \frac{1}{2}\,\Delta\tilde{\boldsymbol{s}}^{\mathrm{T}}\,\nabla^2_{\tilde{\boldsymbol{s}}\tilde{\boldsymbol{s}}}L(\tilde{\boldsymbol{s}}^i, \boldsymbol{\lambda}^i, \boldsymbol{\mu}^i)\,\Delta\tilde{\boldsymbol{s}} + \nabla J(\tilde{\boldsymbol{s}}^i)^{\mathrm{T}}\,\Delta\tilde{\boldsymbol{s}} \\ \overline{\boldsymbol{h}^i}(\Delta\tilde{\boldsymbol{s}}) &= \tilde{\boldsymbol{h}}(\tilde{\boldsymbol{s}}^i) + \nabla\tilde{\boldsymbol{h}}(\tilde{\boldsymbol{s}}^i)^{\mathrm{T}}\,\Delta\tilde{\boldsymbol{s}} \\ \overline{\boldsymbol{g}^i}(\Delta\tilde{\boldsymbol{s}}) &= \tilde{\boldsymbol{g}}(\tilde{\boldsymbol{s}}^i) + \nabla\tilde{\boldsymbol{g}}(\tilde{\boldsymbol{s}}^i)^{\mathrm{T}}\,\Delta\tilde{\boldsymbol{s}}\,. \end{aligned} \tag{5.10}$$

With the solution of the quadratic sub-problem, the design parameters can be updated as follows

$$\tilde{\boldsymbol{s}}^{i+1} = \tilde{\boldsymbol{s}}^i + \Delta\tilde{\boldsymbol{s}}^i\,. \tag{5.11}$$

The approximations for the quadratic sub-problem, cf. Eq. (5.10), contain the derivatives of the objective function $\nabla\tilde{J}(\tilde{\boldsymbol{s}}^i)$, the equality constraints $\nabla\tilde{\boldsymbol{h}}(\tilde{\boldsymbol{s}}^i)$ and inequality constraints $\nabla\tilde{\boldsymbol{g}}(\tilde{\boldsymbol{s}}^i)$ with respect to the design parameters. In addition to this, the Hessian matrix of the Lagrange function $\nabla^2_{\tilde{\boldsymbol{s}}\tilde{\boldsymbol{s}}}L$, is required, the derivative second-order. In this thesis, the SQP algorithm is executed by the MATLAB function *fmincon* from the MATLAB optimisation toolbox. *fmincon* enables numerical access to calculate these derivatives via an application of finite differences. Thus, the user only has to provide the objective function and constraints. However, the application of the Finite Difference Method (FDM) is a precise though time-consuming method. For this reason, the required derivatives are determined in the course of this work. They are transferred to the mathematical optimiser in the framework of FEM. In contrast, the Hessian matrix is provided by the *fmincon* function using an iterative update, where the Broyden-Fletcher-Goldfarb-Shanno (BFGS) formulation is used. The BFGS procedure guarantees a positive definite Hessian matrix to fulfil the sufficient optimisation condition for a local minimum, see [120].

5.5.2. Nonlinear Least-Square Problems

The mathematical description of a general nonlinear least-square curve-fitting problem follows with

$$\begin{array}{lll} \underset{\boldsymbol{m}\,\in\,\mathbb{R}^{n_m}}{\min} & \sum\limits_{j=1}^{m_j} \tilde{J}_j(\boldsymbol{m})^2 & \text{with} \;\; j \;\in\; \{1,\dots,m_j\} \\ & \text{subject to} & \\ & m_i^l \;\leq\; m_i \;\leq\; m_i^u & \text{with} \;\; i \;\in\; \{1,\dots,n_m\}\,. \end{array} \tag{5.12}$$

Thereby, the problem at this point relates to a material fitting problem. Thus, the following quantities correspond to the

$$\tilde{J}_j \;:\; \mathbb{R}^{n_s} \;\to\; \mathbb{R} \;\; j \;\in\; \{1,\dots,m_j\} \;\; \text{objective function}\,, \tag{5.13}$$

with a vector-valued objective function applied as $\tilde{\boldsymbol{J}} = \left[\tilde{J}_1,\dots,\tilde{J}_{m_j}\right]^{\mathrm{T}}$. Additionally, the material parameters and limits are specified with

$$\begin{array}{ll} \boldsymbol{m} = \left[m_1,\dots,m_{n_m}\right]^{\mathrm{T}} & \text{material parameters} \\ \text{with} & \\ m_i^l,\, m_i^u \;\in \{1,\dots,n_m\} & \text{lower and upper bounds}\,. \end{array} \tag{5.14}$$

Solving the least-squares problem provides the values of the parameters for the requested function that best match the data. The Levenberg-Marquardt method is applied to solve the minimisation problem. This gradient-based optimisation strategy applies the trust-region strategy to calculate the next iteration step and uses a Hessian approximation, i.e. $\nabla^2\tilde{\boldsymbol{J}} \;\approx\; \nabla\tilde{\boldsymbol{J}}^{\mathrm{T}}\nabla\tilde{\boldsymbol{J}}$, to reduce the computational effort. The trust-region is one of two possible strategies; the alternative is the line search method; to calculate the next iteration step of a defined sub-problem. Mathematical background to the methods can be found in the literature, e.g. [100]. Given these backgrounds, the required sub-problem can be summarised in each iteration point $\boldsymbol{m}^i$ as follows

$$\begin{array}{llll} \underset{\boldsymbol{p}\,\in\,\mathbb{R}^{\mathrm{dofp}}}{\min} & ||\nabla\tilde{\boldsymbol{J}}(\boldsymbol{m}^i)\,\boldsymbol{p} \,+\, \tilde{\boldsymbol{J}}(\boldsymbol{m}^i)||_2^2 & & \text{with}\,||\boldsymbol{p}|| \leq \Delta \\ & \text{subject to} & & \\ & (\nabla\tilde{\boldsymbol{J}}(\boldsymbol{m}^i)^{\mathrm{T}}\,\nabla\tilde{\boldsymbol{J}}(\boldsymbol{m}^i) \,+\, \lambda\,\mathbf{1})\,\boldsymbol{p} & = & -\nabla\tilde{\boldsymbol{J}}(\boldsymbol{m}^i)^{\mathrm{T}}\,\tilde{\boldsymbol{J}}(\boldsymbol{m}^i) \\ & \lambda\,(\Delta \,-\, ||\boldsymbol{p}||) & = & 0\,. \end{array} \tag{5.15}$$

The notation $||\bullet||_2^2$ denotes the sum of the squares, and dofc refers to the global number of material parameters. $\boldsymbol{p}$ is the descent direction vector, Δ is the trust-region radius and

λ is a scalar value. If $\boldsymbol{p}^{i*}$ is a feasible solution of the sub-problem, and $\lambda \geq 0$, the design parameters can be updated as follows

$$\boldsymbol{m}^{i+1} = \boldsymbol{m}^{i} + \boldsymbol{p}^{i*} . \tag{5.16}$$

The MATLAB Optimisation toolbox is used to solve the least-squares problem. In detail, the function *lsqnonlin* is utilised, which applies the Levenberg-Marquardt method.

5.6. Remarks on Objective, Constraints and Design Parameters

The following section provides a short overview of continuum mechanical quantities, which are applied as objective functions or constraints in the course of this work. This proposal predominantly applies two different optimisation problems; the nonlinear constrained optimisation problems and the least-square problems. The constrained optimisation problems minimise structural-mechanical quantities as a scalar value objective function and the design parameters have geometrical characteristics. Within the framework of the applied nonlinear least-squares problems, the objective function can represent arbitrary structural-mechanical quantities. Specification of the discussed objective functions, constraints and design parameters are shown in Table 5.1. The design parameters are material parameters of the mechanical-chemical problem. Details for solving the optimisation tasks follow in the corresponding sections.

Table 5.1.: Specification of the discussed objective functions, constraints and design parameters within the scope of this thesis.

Objective function	Constraint	Design parameters
stress	area	geometry
area	stress	geometry
deformation		material parameters
concentrations		material parameters

5.7. Concluding Remarks for the Optimisation

In addition to a general introduction to the terminology of structural optimisation, the following insights can be obtained from this section.

- *Shape optimisation and material parameter optimisation are addressed in this thesis.*
- *Knowledge about the process and the connections of the structural optimisation with a continuum mechanical problem.*
- *Strategy for geometric modelling by referring to CAGD-based parametrisation and insights into the implementation.*
- *Mathematical foundations for the nonlinear constrained optimisation problem as a mathematical solver for shape problems.*
- *Mathematical foundations for the nonlinear least-square problem as a mathematical solver for parameter optimisation.*

6. Sensitivity Analysis

This section introduces the applied sensitivity analysis and presents the obtained sensitivities of the continuum mechanical quantities. This section aims to introduce the tangential sensitivity using the same methodology as for the derivation of the tangential stiffness in the structural analysis. Additionally, this section elaborates on the required variations of the objective functions and constraints required in the optimisation process.

6.1. Introduction to Sensitivity Analysis

The sensitivity analysis is an important component in structural optimisation, in which the derivations of the objective functions and constraints are determined. However, the determination of derivatives has proven to be a complex and indeed extensive task. A special feature of this work is that a complex continuum mechanical, coupled and time-dependent problem exists. A time-efficient and accurate strategy to determine sensitivities is used. Therefore, the access via the variation of continuum mechanical quantities within the variational sensitivity approach is applied. The sensitivity analysis is based on the same numerical approximation method, i.e. FEM, as the underlying structural analysis, see [13]. Both structural analysis and sensitivity analysis can be implemented simultaneously, maximising the efficiency of the computational effort in comparison to numerical approaches. The efficiency of this ansatz is highlighted among others in [10, 12, 52, 73, 91]. Due to the chemical concentrations, a path-dependent design behaviour becomes present and the history of the deformation is influenced. A nonlinear behaviour must be taken into account in the sensitivity analysis. Therefore, the history field is included in the gradient calculations. Similar procedures are used in [85] referring to plastic structures or [57] referring to damage models.

In this section, the required variations of the continuous equations are first described, followed by the outline of the discretisation with an analogous procedure as presented before for the structural analysis. Due to the fact, both geometry and material related changes are considered, they are therefore, both presented. The CAGD-based FE-formulation allows for introducing a so-called design velocity field, which transforms the geometrical sensitivities to a chosen design space. Finally, the derivations of selected objective functions and constraints of an optimisation task can be introduced on this basis. This thesis addresses the first principal stress and area changes as objective functions and constraints.

However, a short overview of different strategies for the structural sensitivity analysis in the literature is first presented.

6.2. State-of-the-Art for Presumptions on Sensitivity Analysis

In the structural sensitivity analysis, the change of an arbitrary problem function is calculated based on selected structural parameters. Structural optimisation involves the derivatives of objective functions and constraints with respect to design parameters. A good overview of different sensitivity analysis approaches is provided by, e.g. [135]. Nevertheless, three different possibilities for the calculation of sensitivities are discussed in the following:

- *Global finite differences,*
- *Continuum variations,*
- *Discrete derivatives.*

In order to determine *global finite differences*, the structural analysis is repeatedly calculated while perturbing the design parameters. Thus, the numerical procedure of the FEM can be applied to determine the derivatives. However, due to the repeated calculations and the need to select perturbation parameters, the task results in an onerous method. Thus, this approach can be used to verify analytically determined derivatives. The global finite difference approach is then applied, e.g. in [142, 108, 75]. This strategy is in this work only used to validate the implementation of the analytically derived equations.

The *continuum variations* are calculated within the framework of the variational sensitivity analysis. In this approach, first, the gradients of the continuous equations that determine the structural behaviour are calculated with respect to the design parameters. Then, the continuous sensitivities are discretised in space and time according to the numerical approximation methods of structural analysis. This continuum mechanical-based approach is introduced in [13], where an integrated formulation of all necessary variations, linearisation and derivatives of the sensitivity analysis for a continuum are presented.

Barthold presents in [6] the basic principles of design changes necessary for structural optimisation and their effects on the structural response on a continuum. A convective approach with local coordinates is introduced, derived from a differentiable manifold. Furthermore, Barthold emphasises this approach's importance for obtaining information about the kinematic relation required for numerical methods such as the FEM and CAGD. The sensitivity analysis is based on the works of the material derivation approach, see among others [30, 124, 31], and the domain parameterisation approach, see [63, 58]. Recent works applying the variational sensitivity approach are, e.g. [52, 91, 73, 85]. This efficient strategy is also pursued in this work and derived for the current problem.

The *discrete derivatives* are determined by obtaining the discrete formulations of the structural-mechanical problem with respect to the design parameters. Therefore, the discretisation of the continuum mechanical problem is carried out first and then the derivatives are established. A more detailed overview is provided by [135]. As a particular case, the discrete sensitivity analysis can be combined with the FDM. In such a semi-analytical approach, as presented in [72, 62], only the global quantities are determined analytically, whereas finite differences obtain the local quantities.

6.3. Weak Formulation in the Parameter Space

The weak formulation in the reference configuration introduced in Sec. 4.2 is transformed into the parameter space with the help of the kinematics presented in Sec. 3.3.1. Due to the representation in the convective coordinates of the parameter space, the integration domain is independent of the geometry, deformations and chemical concentrations. This allows an easier variation of the weak form and enables access to the partial variations within the framework of the sensitivity analysis.

Weak Formulation for Balance of Momentum in the Parameter Space

First, the mechanical contribution of the weak formulation follows in the parameter space with

$$R_u(\boldsymbol{u},\, c_\gamma,\, \boldsymbol{\eta}) \;=\; \int\limits_{\Omega_\theta} \mathbf{S}_K \,:\, \delta_u \mathbf{E}\, J_K \,\mathrm{d}V_\theta \;-\; \int\limits_{\Gamma_\theta} \boldsymbol{t}^*_\theta \cdot \boldsymbol{\eta}\,\mathrm{d}A_{\boldsymbol{\theta}}\,, \tag{6.1}$$

with the test functions for the displacements $\boldsymbol{\eta}$.

Weak Formulation for Balance of Mass in the Parameter Space

Secondly, the weak formulation of the balance of mass for the concentrations follows in the parameter space with the test functions for the concentrations γ, i.e.

$$R_{c_\gamma}(\boldsymbol{u},\, c_\gamma,\, \gamma) \;=\; \int\limits_{\Omega_\theta} (\dot{c}_\gamma\, J\, \gamma \,-\, \boldsymbol{J}_\gamma \cdot \operatorname{Grad}\gamma\,) J_K \, \mathrm{d}V_\theta \,-\, \int\limits_{\Gamma_\theta} \boldsymbol{J}_{\gamma\,\theta} \cdot \gamma\, \boldsymbol{N}_\theta \, \mathrm{d}A_{\boldsymbol{\theta}}\,, \tag{6.2}$$

wherein the connection between the spatial and local flux of the concentration is applied with $\boldsymbol{J}_{\gamma\,\theta} = J_K\, \boldsymbol{J}_\gamma\, \mathbf{K}^{-\mathrm{T}}$.

6.4. Total Variation of the Weak Formulation

The variation of the weak formulation from Eq. (4.6) is not only the basis for the solution of the structural problem; it also leads to the requirement of the sensitivity analysis. Within the framework of structural optimisation, the continuum can change both geometrical and material parameters to optimise the structural response. As a result, the multi-linear representation of the variation of the weak formulation is extended as a result, cf. [138, 6], so that

$$\delta R \,=\, \delta_X R \,+\, \delta_m R \,+\, \delta_u R \,+\, \delta_{c_\gamma} R \,+\, \delta_h R \,=\, 0\,. \tag{6.3}$$

In other words, the condition for solving the structural problem should also be met if the geometry, the material parameters or the history of the evolutionary problem changes. On this basis, the additional partial variations, cf. Eq. (4.7), result in

$$\begin{aligned} \delta_X R &= p_X(\boldsymbol{\eta},\, \gamma;\, \delta\boldsymbol{X}) \\ \delta_m R &= p_m(\boldsymbol{\eta},\, \gamma;\, \delta\boldsymbol{m}) \\ \delta_h R &= h(\boldsymbol{\eta},\, \gamma;\, \delta h)\,. \end{aligned} \tag{6.4}$$

The forms $p_{(\bullet)}$ are the tangential sensitivities of the system with the index referring to a change of geometry p_X or a change of material parameters p_m. Analogous to the procedure for calculating the sensitivity of plastic structures, the path-dependent history variables must be considered, cf. [85]. The path dependence in this work is due to the chemical concentrations. Thus, the form h corresponds to the concentration history. Here again, the following partial variations are based on the derivations outlined in Appendix A.1. The partial variation of the weak formulation with respect to the geometry is decomposed into the mechanical $\delta_X R_u$ and chemical $\delta_X R_{c_\gamma}$ part of the weak formulation so that

$$\delta_X R \,=\, \delta_X R_u \,+\, \delta_X R_{c_\gamma}\,. \tag{6.5}$$

The partial variation of the mechanical weak formulation follows in detail with

$$\begin{aligned}
\delta_X R_u \;&=\; \int\limits_{\Omega_0} \left[\delta_X \mathbf{S}_K \,:\, \delta_u \mathbf{E}\, J_K \,+\, \mathbf{S}_K \,:\, \delta_X \delta_u \mathbf{E}\, J_K \,+\, \mathbf{S}_K \,:\, \delta_u \mathbf{E}\; \delta_X J_K\right] \mathrm{d}V_\theta \\
&=\; \int\limits_{\Omega_0} \left[\delta_X \mathbf{S}_K \,:\, \delta_u \mathbf{E} \,+\, \mathbf{S}_K \,:\, \delta_X \delta_u \mathbf{E} \,+\, \mathbf{S}_K \,:\, \delta_u \mathbf{E}\ \mathrm{Div}\,\delta \boldsymbol{X}\right] \mathrm{d}V \\
&=\; \int\limits_{\Omega_0} \big[[-\mathbb{C} \,:\, \mathrm{sym}(\mathbf{F}^{\mathrm{T}}\,\mathrm{Grad}\,\boldsymbol{u}\,\mathrm{Grad}\,\delta \boldsymbol{X})] \,:\, \mathrm{sym}(\mathbf{F}^{\mathrm{T}}\,\mathrm{Grad}\,\boldsymbol{\eta}) \\
&\qquad -\mathbf{S}_K \,:\, \mathrm{sym}(\mathrm{Grad}\,\boldsymbol{u}\,\mathrm{Grad}\,\delta \boldsymbol{X}\,\mathrm{Grad}\,\boldsymbol{\eta} \,-\, \mathbf{F}^{\mathrm{T}}\,\mathrm{Grad}\,\boldsymbol{\eta}\,\mathrm{Grad}\,\delta \boldsymbol{X}) \\
&\qquad +\mathbf{S}_K \,:\, \mathrm{sym}(\mathbf{F}^{\mathrm{T}}\,\mathrm{Grad}\,\boldsymbol{\eta})\,\mathrm{Div}\,\delta \boldsymbol{X}\big]\,\mathrm{d}V\,,
\end{aligned} \tag{6.6}$$

wherein Eq. (3.28), Eq. (3.29), Eq. (3.30) and Appendix A.1.2 are utilised. The transport from the reference configuration into the parameter space is performed as presented in Eq. (6.1), since the integration area in the parameter space is independent of the geometry. Consequently, the variation of the local geometry determinant $\delta_X J_K$, derived in Eq. (3.30), is applied.

The same procedure is used for the variation of the weak formulation for the balance of mass referred to the concentrations, based on Eq. (6.2), which results in

$$\begin{aligned}
\delta_X R_{c_\gamma} \;&=\; \int\limits_{\Omega_0} \big[\delta_X J\,\dot{c}_\gamma\,\gamma \,+\, J\,\delta_X \dot{c}_\gamma\,\gamma \,-\, \delta_X \boldsymbol{J}_\gamma \cdot \mathrm{Grad}\,\gamma \,-\, \boldsymbol{J}_\gamma \cdot \delta_X \mathrm{Grad}\,\gamma \\
&\qquad +(J\,\dot{c}_\gamma\,\gamma \,-\, \boldsymbol{J}_\gamma \,\cdot\, \mathrm{Grad}\,\gamma)\,\mathrm{Div}\,\delta \boldsymbol{X}\big]\,\mathrm{d}V \\
&=\; \int\limits_{\Omega_0} \big[-J\,\mathbf{C}^{-1} \,:\, \mathrm{sym}(\mathbf{F}^{\mathrm{T}}\,\mathrm{Grad}\,\boldsymbol{u}\,\mathrm{Grad}\,\delta \boldsymbol{X})\,\dot{c}_\gamma\,\gamma \,-\, J\,\dot{c}_\gamma\,\mathbf{1}\,\mathrm{Grad}\,\delta \boldsymbol{X}\,\gamma \\
&\qquad +[\mathbb{A} \,:\, \mathrm{sym}(\mathbf{F}^{\mathrm{T}}\,\mathrm{Grad}\,\boldsymbol{u}\,\mathrm{Grad}\,\delta \boldsymbol{X})] \,\cdot\, \mathrm{Grad}\,\gamma \\
&\qquad -D\,\mathrm{Grad}\,c_\gamma\,\mathrm{Grad}\,\delta \boldsymbol{X}\;J\,\mathbf{C}^{-\mathrm{T}} \,\cdot\, \mathrm{Grad}\,\gamma \,+\, \boldsymbol{J}_\gamma \,\cdot\, \mathrm{Grad}\,\gamma\,\mathrm{Grad}\,\delta \boldsymbol{X} \\
&\qquad +J\,\dot{c}_\gamma\,\mathrm{Grad}\,\delta \boldsymbol{X} \,\cdot\, \mathbf{1} \,-\, \boldsymbol{J}_\gamma \,\cdot\, \mathrm{Grad}\,\gamma\,\mathrm{Grad}\,\delta \boldsymbol{X} \,\cdot\, \mathbf{1}\,\big]\,\mathrm{d}V\,,
\end{aligned} \tag{6.7}$$

with reference to the Eq. (3.28), Eq. (3.29), Eq. (3.30) and Appendix A.1.4.

The variation of the weak formulation with respect to the material parameters $\delta_m R$ follows with

$$\delta_m R \,=\, \delta_m R_u \,+\, \delta_m R_{c_\gamma}\,, \tag{6.8}$$

wherein the mechanical part $\delta_m R_u$ leads to

$$\delta_m R_u = \int_{\Omega_0} \delta_m \mathbf{S}_K : \delta_u \mathbf{E} \,\mathrm{d}V \,. \tag{6.9}$$

Here, reference is made to Appendix A.1.2 and the second-order tensor $\mathbf{C}_n$ is applied with

$$\mathbf{C}_n = \{\mathbf{C}_1, \mathbf{C}_2, \mathbf{C}_3, \mathbf{C}_4, \mathbf{C}_5\} \qquad \text{with} \qquad n \in \{1, 2, 3, 4, 5\} \,, \tag{6.10}$$

so that the partial variation of the mechanical weak formulation follows with utilisation of Eq. (3.29), i.e.

$$\delta_m R_u = \int_{\Omega_0} \mathbf{C}_n : \mathrm{sym}(\mathbf{F}^{\mathrm{T}} \,\mathrm{Grad}\, \boldsymbol{\eta}) \,\mathrm{d}V. \tag{6.11}$$

Furthermore, the chemical part of the variation of the weak formulation with respect to the material parameters $\delta_m R_{c_\gamma}$ results in

$$\delta_m R_{c_\gamma} = \int_{\Omega_0} - \mathbf{C}_6 \cdot \mathrm{Grad}\, \gamma \,\mathrm{d}V \,, \tag{6.12}$$

wherein reference is made to Appendix A.1.4.

Finally, the chemical part of the weak formulation depends on the evolution of the concentrations $\delta_h R_{c_\gamma}$, so that

$$\delta_h R_{c_\gamma} = \int_{\Omega_0} (J \, \delta_h \dot{c}_\gamma \, \gamma) \,\mathrm{d}V \,. \tag{6.13}$$

6.5. Discrete Tangential Sensitivity

6.5.1. Discrete Tangential Sensitivity for Geometry Parameters

The summary of the tangential sensitivities follows analogous to the discrete representation of the stiffness matrix and is based on the previously introduced discretisation, cf. Sec. 4.4. First, the so-called pseudo-load matrix $\mathbf{P}^e_X$ is derived from the tangential sensitivities with respect to the geometry sensitivity. Here again, sub-matrices $\mathbf{P}^{IJ}_{X1}$ and $\mathbf{P}^{IJ}_{X2}$ are introduced, referring to the evaluation per node. The discrete form of the mechanical part is based on the variation in Eq. (6.6).

Therefore, it follows

$$
\begin{aligned}
\delta_X R_u^h \;&=\; \sum_{I=1}^{\mathrm{nn}} \sum_{J=1}^{\mathrm{nn}} (\boldsymbol{\eta}^I)^{\mathrm{T}} \quad \Bigg[\int\!\!\!\int_{\Omega_e} (-(\mathbf{B}_u^I)^{\mathrm{T}} \, \underline{\mathbf{C}} \, \mathbf{B}_o^J \;-\; \mathrm{Grad}\, \mathbf{u} \, (\mathbf{L}^I)^{\mathrm{T}} \, \mathbf{S}_K \, \mathbf{L}^J \\
&\qquad\qquad - (\mathbf{B}_u^J)^{\mathrm{T}} \, \underline{\mathbf{S}}_K \, \mathbf{L}^I \;+\; (\mathbf{B}_u^I)^{\mathrm{T}} \, \underline{\mathbf{S}}_K \, \mathbf{L}^J \,) \, \mathrm{d}V \Bigg] \delta \mathbf{X}^J \\
&=\; \sum_{I=1}^{\mathrm{nn}} \sum_{J=1}^{\mathrm{nn}} (\boldsymbol{\eta}^I)^{\mathrm{T}} \quad \mathbf{P}_{X1}^{IJ} \, \delta \mathbf{X}^J \, .
\end{aligned}
\tag{6.14}
$$

Here, the introduced B-matrices for the variation of the Green-Lagrange tensor are applied with respect to the displacement $\mathbf{B}_u^I$ in Eq. (4.21) and with respect to the geometry $\mathbf{B}_o^J$ in Eq. (4.22). The terms result in the sub-matrix $\mathbf{P}_{X1}^{IJ} \in \mathbb{R}^{2\times 2}$. Furthermore, the discretisation of the chemical part from Eq. (6.7) refers to the row matrix $\mathbf{P}_{X2}^{IJ} \in \mathbb{R}^{1\times 2}$, i.e.

$$
\begin{aligned}
\delta_X R_{c_\gamma}^h \;&=\; \sum_{I=1}^{\mathrm{nn}} \sum_{J=1}^{\mathrm{nn}} \gamma^I \quad \Bigg[\int\!\!\!\int_{\Omega_e} (-h^I \, J \, \dot{c}_\gamma \, (\mathbf{L}^J)^{\mathrm{T}} \, \mathbf{C}^{-\mathrm{T}} \, \mathbf{F}^{\mathrm{T}} \, \mathrm{Grad}\, \mathbf{u} \;-\; h^I \, J \, \dot{c}_\gamma \, (\mathbf{L}^J)^{\mathrm{T}} \\
&\qquad\qquad - (\mathbf{L}^I)^{\mathrm{T}} \, \mathbf{C}^{-\mathrm{T}} \, \mathbf{L}^J \, D \, J \, \mathrm{Grad}\, \mathbf{c}_\gamma + \; (\mathbf{L}^I)^{\mathrm{T}} \, \underline{\mathbf{A}} \, \mathbf{B}_o^I \\
&\qquad\qquad + \mathbf{J}_\gamma \, \mathbf{L}^J \, (\mathbf{L}^I)^{\mathrm{T}} \;+\; h^I \, J \, \dot{c}_\gamma \, (\mathbf{L}^J)^{\mathrm{T}} - \; (\mathbf{L}^J)^{\mathrm{T}} \, \mathbf{J}_\gamma \, (\mathbf{L}^I)^{\mathrm{T}}) \, \mathrm{d}V \Bigg] \delta \mathbf{X}^J \\
&=\; \sum_{I=1}^{\mathrm{nn}} \sum_{J=1}^{\mathrm{nn}} \gamma^I \quad \mathbf{P}_{X2}^{IJ} \, \delta \mathbf{X}^J \, .
\end{aligned}
\tag{6.15}
$$

The pseudo-load matrix $\mathbf{P}_X^e \in \mathbb{R}^{24\times 16}$ is the sum of eight nodes in each element and follows with

$$
\mathbf{P}_X^e = \sum_{I=1}^{\mathrm{nn}} \sum_{J=1}^{\mathrm{nn}} \begin{bmatrix} \mathbf{P}_{X1}^{IJ} \\ \mathbf{P}_{X2}^{IJ} \end{bmatrix} . \tag{6.16}
$$

6.5.2. Discrete Tangential Sensitivity for Material Parameters

This section outlines the composition of the pseudo-load matrix $\mathbf{P}_m^e$, which depends on the sensitivity due to a change of material parameters. The sub-column matrices $\mathbf{P}_{m1}^I, \mathbf{P}_{m2}^I, \mathbf{P}_{m3}^I, \mathbf{P}_{m4}^I, \mathbf{P}_{m5}^I \in \mathbb{R}^2$ result from the variation of the mechanical part of the weak formulation from Eq. (6.11).

The matrices have the same dimension and are listed as follows

$$\begin{aligned}
\delta_{\mu} R_u^h &= \sum_{I=1}^{\text{nn}} (\boldsymbol{\eta}^I)^{\mathrm{T}} \left[\int_{\Omega_e} (\mathbf{B}_u^I)^{\mathrm{T}}\, \mathbf{C}_1 \,\mathrm{d}V \right] &= \sum_{I=1}^{\text{nn}} (\boldsymbol{\eta}^I)^{\mathrm{T}}\, \mathbf{P}_{m1}^I \\
\delta_{\lambda} R_u^h &= \sum_{I=1}^{\text{nn}} (\boldsymbol{\eta}^I)^{\mathrm{T}} \left[\int_{\Omega_e} (\mathbf{B}_u^I)^{\mathrm{T}}\, \mathbf{C}_2 \,\mathrm{d}V \right] &= \sum_{I=1}^{\text{nn}} (\boldsymbol{\eta}^I)^{\mathrm{T}}\, \mathbf{P}_{m2}^I \\
\delta_{\rho_0} R_u^h &= \sum_{I=1}^{\text{nn}} (\boldsymbol{\eta}^I)^{\mathrm{T}} \left[\int_{\Omega_e} (\mathbf{B}_u^I)^{\mathrm{T}}\, \mathbf{C}_3 \,\mathrm{d}V \right] &= \sum_{I=1}^{\text{nn}} (\boldsymbol{\eta}^I)^{\mathrm{T}}\, \mathbf{P}_{m3}^I \\
\delta_{M_\gamma} R_u^h &= \sum_{I=1}^{\text{nn}} (\boldsymbol{\eta}^I)^{\mathrm{T}} \left[\int_{\Omega_e} (\mathbf{B}_u^I)^{\mathrm{T}}\, \mathbf{C}_4 \,\mathrm{d}V \right] &= \sum_{I=1}^{\text{nn}} (\boldsymbol{\eta}^I)^{\mathrm{T}}\, \mathbf{P}_{m4}^I \\
\delta_{c_\gamma^{\mathrm{t}=0}} R_u^h &= \sum_{I=1}^{\text{nn}} (\boldsymbol{\eta}^I)^{\mathrm{T}} \left[\int_{\Omega_e} (\mathbf{B}_u^I)^{\mathrm{T}}\, \mathbf{C}_5 \,\mathrm{d}V \right] &= \sum_{I=1}^{\text{nn}} (\boldsymbol{\eta}^I)^{\mathrm{T}}\, \mathbf{P}_{m5}^I \,.
\end{aligned} \tag{6.17}$$

Whereas the chemical part of the variation of the weak formulation referring to Eq. (6.12) results only in one dependency with

$$\delta_D R_{c_\gamma}^h = \sum_{I=1}^{\text{nn}} \gamma^I \left[\int_{\Omega_e} (\mathbf{L}^I)^{\mathrm{T}}\, \mathbf{C}_6 \,\mathrm{d}V \right] = \sum_{I=1}^{\text{nn}} \gamma^I\, P_{m6}^I \,, \tag{6.18}$$

with the scalar P_{m6}^I. Therefore, the discrete pseudo-load matrix $\mathbf{P}_m^e \in \mathbb{R}^{24\times 6}$ follows by summation of the nodes and refers to the material sensitivity, so that

$$\mathbf{P}_m^e = \sum_{I=1}^{\text{nn}} \begin{bmatrix} \mathbf{P}_{m1}^I & \mathbf{P}_{m2}^I & \mathbf{P}_{m3}^I & \mathbf{P}_{m4}^I & \mathbf{P}_{m5}^I & \mathbf{0} \\ 0 & 0 & 0 & 0 & 0 & P_{m6}^I \end{bmatrix} . \tag{6.19}$$

6.5.3. Discrete Tangential Sensitivity for the History Field

The history field matrix from Eq. (4.32) contains information about the displacement, the concentrations, the velocity and acceleration of both primary variables referring to the previous time step. In the following, the partial variations of the weak formulations with respect to the history field are derived. The displacements depend only on the actual time step, so that the partial variations of the weak formulations with respect to the history field are not applicable, so that

$$\begin{aligned}
\delta_{u_{\mathrm{N}}} R_u^h &= \sum_{I=1}^{\text{nn}} \sum_{J=1}^{\text{nn}} (\boldsymbol{\eta}^I)^{\mathrm{T}} \left[\int_{\Omega_e} 0 \,\mathrm{d}V \right] \delta \mathbf{u}_{\mathrm{N}}^J &= \sum_{I=1}^{\text{nn}} \sum_{J=1}^{\text{nn}} (\boldsymbol{\eta}^I)^{\mathrm{T}}\, \mathbf{Z}_{1a}^{IJ}\, \delta \mathbf{u}_{\mathrm{N}}^J &= 0 \\
\delta_{c_{\gamma\mathrm{N}}} R_u^h &= \sum_{I=1}^{\text{nn}} \sum_{J=1}^{\text{nn}} (\boldsymbol{\eta}^I)^{\mathrm{T}} \left[\int_{\Omega_e} 0 \,\mathrm{d}V \right] \delta c_{\gamma\mathrm{N}}^J &= \sum_{I=1}^{\text{nn}} \sum_{J=1}^{\text{nn}} (\boldsymbol{\eta}^I)^{\mathrm{T}}\, \mathbf{Z}_{2a}^{IJ}\, \delta c_{\gamma\mathrm{N}}^J &= 0 \,,
\end{aligned} \tag{6.20}$$

wherein only the variations with respect to the primary variables of the previous time step are listed, for the displacements $\mathbf{Z}^{IJ}_{1a} = \mathbf{0} \in \mathbb{R}^{2\times2}$, respectively for the concentrations $\mathbf{Z}^{IJ}_{2a} = \mathbf{0} \in \mathbb{R}^{2}$. The same procedure is applied for the variation of the mechanical part of the weak formulation with respect to the velocity $\delta_{\dot{u}_\mathrm{N}} R^h_u$ and acceleration $\delta_{\ddot{u}_\mathrm{N}} R^h_u$ terms, which lead to the empty matrices with the dimensions $\mathbf{Z}^{IJ}_{1b}, \mathbf{Z}^{IJ}_{1c} \in \mathbb{R}^{2\times2}$. Furthermore, the variation with respect to the velocity $\delta_{\dot{c}_{\gamma\mathrm{N}}} R^h_u$ and acceleration $\delta_{\ddot{c}_{\gamma\mathrm{N}}} R^h_u$ of the concentration results in the empty sub-matrices $\mathbf{Z}^{IJ}_{2b}, \mathbf{Z}^{IJ}_{2c} \in \mathbb{R}^{2}$. Analogue considerations follow for the partial variation of the chemical part of the weak formulation with respect to the displacement, i.e.

$$\delta_{u_\mathrm{N}} R^h_{c_\gamma} = \sum_{I=1}^{\mathrm{nn}} \sum_{J=1}^{\mathrm{nn}} \gamma^I \left[\int_{\Omega_e} 0 \,\mathrm{d}V \right] \delta \mathbf{u}^J_\mathrm{N} = \sum_{I=1}^{\mathrm{nn}} \sum_{J=1}^{\mathrm{nn}} \gamma^I \, \mathbf{Z}^{IJ}_{3a} \, \delta \mathbf{u}^J_\mathrm{N} = 0 \,. \tag{6.21}$$

Thus, the empty sub-matrices follow from the chemical part with respect to the mechanical primary variables and can be summarised with $\mathbf{Z}^{IJ}_{3a}, \mathbf{Z}^{IJ}_{3b}, \mathbf{Z}^{IJ}_{3c} = \mathbf{0} \in \mathbb{R}^{1\times2}$. Finally, the partial variation of the chemical part of the weak formulation with respect to the concentrations, respectively velocity and acceleration of the concentrations are derived from Eq. (6.13) and result in

$$\begin{aligned}
\delta_{c_{\gamma\mathrm{N}}} R^h_{c_\gamma} &= \sum_{I=1}^{\mathrm{nn}} \sum_{J=1}^{\mathrm{nn}} \gamma^I \left[\int_{\Omega_e} - J \, \frac{2}{\Delta\mathrm{t}} \,\mathrm{d}V \right] \delta c^J_{\gamma\mathrm{N}} &&= \sum_{I=1}^{\mathrm{nn}} \sum_{J=1}^{\mathrm{nn}} \gamma^I \, Z^{IJ}_{4a} \, \delta c^J_{\gamma\mathrm{N}} \\
\delta_{\dot{c}_{\gamma\mathrm{N}}} R^h_{c_\gamma} &= \sum_{I=1}^{\mathrm{nn}} \sum_{J=1}^{\mathrm{nn}} \gamma^I \left[\int_{\Omega_e} - J \,\mathrm{d}V \right] \delta \dot{c}^J_{\gamma\mathrm{N}} &&= \sum_{I=1}^{\mathrm{nn}} \sum_{J=1}^{\mathrm{nn}} \gamma^I \, Z^{IJ}_{4b} \, \delta \dot{c}^J_{\gamma\mathrm{N}} \\
\delta_{\ddot{c}_{\gamma\mathrm{N}}} R^h_{c_\gamma} &= \sum_{I=1}^{\mathrm{nn}} \sum_{J=1}^{\mathrm{nn}} \gamma^I \left[\int_{\Omega_e} 0 \,\mathrm{d}V \right] \delta \ddot{c}^J_{\gamma\mathrm{N}} &&= \sum_{I=1}^{\mathrm{nn}} \sum_{J=1}^{\mathrm{nn}} \gamma^I \, Z^{IJ}_{4c} \, \delta \ddot{c}^J_{\gamma\mathrm{N}} \,,
\end{aligned} \tag{6.22}$$

with the scalars $Z^{IJ}_{4a}, Z^{IJ}_{4b}, Z^{IJ}_{4c}$ and the partial variation $\delta_h \dot{c}_\gamma$ from Eq. (4.31.2), i.e.

$$\frac{\partial \dot{c}_\gamma}{\partial c_{\gamma\mathrm{N}}} = -\frac{2}{\Delta\mathrm{t}} \,, \quad \frac{\partial \dot{c}_\gamma}{\partial \dot{c}_{\gamma\mathrm{N}}} = -1 \quad \text{and} \quad \frac{\partial \dot{c}_\gamma}{\partial \ddot{c}_{\gamma\mathrm{N}}} = 0 \,. \tag{6.23}$$

The discretisation of the tangential history matrix follows with the summation of the nodes with

$$\mathbf{H}^e = \sum_{I=1}^{\mathrm{nn}} \sum_{J=1}^{\mathrm{nn}} \begin{bmatrix} \mathbf{Z}^{IJ}_{1a} & \mathbf{Z}^{IJ}_{2a} & \mathbf{Z}^{IJ}_{1b} & \mathbf{Z}^{IJ}_{2b} & \mathbf{Z}^{IJ}_{1c} & \mathbf{Z}^{IJ}_{2c} \\ \mathbf{Z}^{IJ}_{3a} & Z^{IJ}_{4a} & \mathbf{Z}^{IJ}_{3b} & Z^{IJ}_{4b} & \mathbf{Z}^{IJ}_{3c} & Z^{IJ}_{4c} \end{bmatrix} , \tag{6.24}$$

so that $\mathbf{H}^e \in \mathbb{R}^{24\times72}$.

6.5.4. Numerical Implementation for the Sensitivity Analysis

Algorithm 1: Illustration of newton update.

```
Result: $\boldsymbol{\nu}$
initialisation;
    $convergence = 0$ ;  TOL  ;  % $tolerance$
    $time\,step$  ;  $\Delta t$  ;  % $time\,increment$
    $\boldsymbol{\nu} = \mathrm{zeros}(\mathrm{dof}, 1)$  ;  $\mathrm{edof}; \mathrm{dof}$  ;  % $degrees\,of\,freedom\,element;\ global$

while $convergence \neq 1$ do
    element level (MEX interface) with input $\boldsymbol{\nu}^e = \boldsymbol{\nu}(\mathrm{edof})$ ;
    Newmark-update;
    if $time\ step{=}1$ then
        $\boldsymbol{\nu}^e_{\mathrm{N}} = 0; \quad \dot{\boldsymbol{\nu}}^e_{\mathrm{N}} = 0;$
    end
        $\dot{\boldsymbol{\nu}}^e = \frac{2}{\Delta t}\left(\boldsymbol{\nu}^e - \boldsymbol{\nu}^e_{\mathrm{N}}\right) - \dot{\boldsymbol{\nu}}^e_{\mathrm{N}}$
        $\boldsymbol{\nu}^e_{\mathrm{N}} = \boldsymbol{\nu}^e, \quad \dot{\boldsymbol{\nu}}^e_{\mathrm{N}} = \dot{\boldsymbol{\nu}}^e$

    residuum and tangent information's;
        $\mathbf{R}^e(\boldsymbol{\nu}^e, \dot{\boldsymbol{\nu}}^e) \ , \ \mathbf{K}^e(\boldsymbol{\nu}^e, \dot{\boldsymbol{\nu}}^e)$
        $\mathbf{P}^e_X(\boldsymbol{\nu}^e, \dot{\boldsymbol{\nu}}^e) \ , \ \mathbf{P}^e_m(\boldsymbol{\nu}^e, \dot{\boldsymbol{\nu}}^e) \ , \ \mathbf{H}^e(\dot{\boldsymbol{\nu}}^e)$

    global level ;
    assembly;
        $\mathbf{R} = \bigcup_{e=1}^{\mathrm{nel}} \mathbf{R}^e \ , \ \mathbf{K} = \bigcup_{e=1}^{\mathrm{nel}} \mathbf{K}^e$
        $\mathbf{P}_X = \bigcup_{e=1}^{\mathrm{nel}} \mathbf{P}^e_X \ , \ \mathbf{P}_m = \bigcup_{e=1}^{\mathrm{nel}} \mathbf{P}^e_m \ , \ \mathbf{H} = \bigcup_{e=1}^{\mathrm{nel}} \mathbf{H}^e$

    if $|\mathbf{R}| \leq \mathrm{TOL}$ then
        $convergence = 1$;
        further computations of sensitiviy informations with $\mathbf{P}_X$, $\mathbf{P}_m$ and $\mathbf{H}$;
    else
        linearisation ;
            $\Delta\boldsymbol{\nu} = \mathbf{K}^{-1}\,\mathbf{R}$
            $\boldsymbol{\nu} = \boldsymbol{\nu} + \Delta\boldsymbol{\nu}$
    end
end
```

In analogy to the discrete formulations of the tangents in the context of the structural analysis, see Sec. 4.8, the matrices derived at element level are assembled as follows

$$\mathbf{P}_X = \bigcup_{e=1}^{\text{nel}} \mathbf{P}_X^e \quad , \quad \mathbf{P}_m = \bigcup_{e=1}^{\text{nel}} \mathbf{P}_m^e \quad , \quad \mathbf{H} = \bigcup_{e=1}^{\text{nel}} \mathbf{H}^e \, , \tag{6.25}$$

wherein nel denotes the total number of elements and the so-called pseudo-load matrices $\mathbf{P}_X \in \mathbb{R}^{\text{dof} \times \text{dofm}}$, $\mathbf{P}_m \in \mathbb{R}^{\text{dof} \times 6}$ and $\mathbf{H} \in \mathbb{R}^{\text{dof} \times 3\,\text{dof}}$ result. At this point, the global column matrix with the history field is defined with $\tilde{\mathbf{h}} \in \mathbb{R}^{3\,\text{dof}}$, i.e.

$$\tilde{\mathbf{h}} = \begin{bmatrix} \boldsymbol{\nu} & \dot{\boldsymbol{\nu}} \end{bmatrix}^{\mathrm{T}} . \tag{6.26}$$

An overview of the implementation is provided by the Algorithm 1.

6.6. Sensitivity Matrices

6.6.1. Update of the History Variation

The primary variables are stored as internal variables in the history field matrix $\tilde{\mathbf{h}}$, cf. Eq. (6.26). After each time step, the total variation of the residuum has to be updated by the information's from the previous time step, see Algorithm 1. The tangential history matrix, with respect to a change of the geometry $\mathbf{H}_X \in \mathbb{R}^{\text{dof} \times \text{dofm}}$ as well as with respect to a change of the material parameters $\mathbf{H}_m \in \mathbb{R}^{\text{dof} \times 6}$, are derived as follows

$$\begin{aligned} \mathbf{H}_X &= \frac{\partial \mathbf{R}}{\partial \tilde{\mathbf{h}}} \frac{\mathrm{d}\tilde{\mathbf{h}}}{\mathrm{d}\mathbf{X}} = \mathbf{H}\,\mathbf{S}_X^{\mathrm{H}} \\ \mathbf{H}_m &= \frac{\partial \mathbf{R}}{\partial \tilde{\mathbf{h}}} \frac{\mathrm{d}\tilde{\mathbf{h}}}{\mathrm{d}\mathbf{m}} = \mathbf{H}\,\mathbf{S}_m^{\mathrm{H}} \, , \end{aligned} \tag{6.27}$$

wherein the global tangential history matrix $\mathbf{H}$ from Eq. (6.25) is applied. The partial variation of the history with respect to the geometry, respectively with respect to the material parameters, includes the sensitivity information of the previous time step $\mathbf{S}_X^{\mathrm{H}} \in \mathbb{R}^{3\,\text{dof} \times \text{dofm}}$ and $\mathbf{S}_m^{\mathrm{H}} \in \mathbb{R}^{3\,\text{dof} \times 6}$, i.e.

$$\mathbf{S}_X^{\mathrm{H}} = \frac{\mathrm{d}\tilde{\mathbf{h}}}{\mathrm{d}\mathbf{X}} = \begin{bmatrix} \mathbf{S}_{X\mathrm{N}} & \frac{2}{\Delta \mathrm{t}} \mathbf{S}_{X\mathrm{N}} & \mathbf{0} \end{bmatrix}^{\mathrm{T}} ; \quad \mathbf{S}_m^{\mathrm{H}} = \frac{\mathrm{d}\tilde{\mathbf{h}}}{\mathrm{d}\mathbf{m}} = \begin{bmatrix} \mathbf{S}_{m\mathrm{N}} & \frac{2}{\Delta \mathrm{t}} \mathbf{S}_{m\mathrm{N}} & \mathbf{0} \end{bmatrix}^{\mathrm{T}} . \tag{6.28}$$

The partial variations from the Eq. (4.31) are applied and $\mathbf{S}_{X\mathrm{N}}$, respectively $\mathbf{S}_{m\mathrm{N}}$, are the sensitivity matrices of the previous time step. The equations are independent of accelerations.

It should be noted that the matrices $\mathbf{S}_{X\mathrm{N}}$ and $\mathbf{S}_{m\mathrm{N}}$ correspond to zero matrices in the first time step with

$$\begin{aligned} \mathbf{S}_{X\mathrm{N}} &= \mathbf{0} \in \mathbb{R}^{3\,\mathrm{dof}\times\mathrm{dofm}} \\ \mathbf{S}_{m\mathrm{N}} &= \mathbf{0} \in \mathbb{R}^{3\,\mathrm{dof}\times 6}\,. \end{aligned} \tag{6.29}$$

Remark: In the context of the sensitivity analysis, the sensitivity information is introduced using the matrices $\mathbf{S}_X^{\mathrm{H}}, \mathbf{S}_{m\mathrm{N}}, \mathbf{S}_{X\mathrm{N}}, \mathbf{S}_{m\mathrm{N}}, \mathbf{S}_X$ and $\mathbf{S}_m$. This notation is not to be confounded with the matrix $\mathbf{S}_K$ for the description for the second Piola-Kirchhoff tensor.

6.6.2. Sensitivity Matrix for Geometric Changes

Assuming a fixed set of material parameters, yet with a differentiable set of geometry parameters for the initial design, results in the following total partial variation of the weak formulation in global matrix representation, i.e.

$$\begin{aligned} \delta\mathbf{R} &= \frac{\partial\mathbf{R}}{\partial\mathbf{X}}\,\delta\mathbf{X} + \frac{\partial\mathbf{R}}{\partial\mathbf{u}}\,\delta\mathbf{u} + \frac{\partial\mathbf{R}}{\partial\mathbf{c}_\gamma}\,\delta\mathbf{c}_\gamma + \frac{\partial\mathbf{R}}{\partial\tilde{\mathbf{h}}}\,\frac{\mathrm{d}\tilde{\mathbf{h}}}{\mathrm{d}\mathbf{X}}\,\delta\mathbf{X} = \mathbf{0} \\ &= \left[\mathbf{P}_X + \mathbf{H}_X\right]\delta\mathbf{X} + \mathbf{K}\begin{bmatrix}\delta\mathbf{u}\\ \delta\mathbf{c}_\gamma\end{bmatrix}\,, \end{aligned} \tag{6.30}$$

based on the multi-linear form from Eq. (6.3). The stiffness matrix $\mathbf{K}$, respectively the pseudo-load matrix $\mathbf{P}_X$, refers to the assembly in Eq. (4.42) and Eq. (6.25). Furthermore, the matrix $\mathbf{H}_X$ is the sensitivity history matrix with respect to the geometry, which is evaluated in Sec. 6.6.1, cf. Eq. (6.27.1). The total variation of the primary variables $\boldsymbol{\nu}$ with respect to a change of the geometry, leads to the following sensitivity matrix $\mathbf{S}_X \in \mathbb{R}^{\mathrm{dof}\times\mathrm{dofm}}$

$$\mathbf{S}_X = \frac{\mathrm{d}\boldsymbol{\nu}}{\mathrm{d}\mathbf{X}} = -\mathbf{K}^{-1}\left[\mathbf{P}_X + \mathbf{H}_X\right]. \tag{6.31}$$

6.6.3. Sensitivity Matrix for Material Changes

In addition to examining possible geometric changes, the sensitivity of the material parameters is studied in this thesis. Therefore, the geometry parameters are fixed and the variation of the residuum includes the partial variation of the residuum with respect to a change of the material parameters, i.e.

$$\begin{aligned} \delta \mathbf{R} &= \frac{\partial \mathbf{R}}{\partial \mathbf{m}} \delta \mathbf{m} + \frac{\partial \mathbf{R}}{\partial \mathbf{u}} \delta \mathbf{u} + \frac{\partial \mathbf{R}}{\partial \mathbf{c}_\gamma} \delta \mathbf{c}_\gamma + \frac{\partial \mathbf{R}}{\partial \tilde{\mathbf{h}}} \frac{\mathrm{d}\tilde{\mathbf{h}}}{\mathrm{d}\mathbf{m}} \delta \mathbf{m} = \mathbf{0} \\ &= [\mathbf{P}_m + \mathbf{H}_m]\, \delta \mathbf{m} + \mathbf{K}\, \delta \boldsymbol{\nu}\,, \end{aligned} \tag{6.32}$$

wherein the material parameters are stored in the column matrix form $\mathbf{m} \in \mathbb{R}^6$, cf. Eq. (3.72), with a total of 6 material parameters containing mechanical and chemical components. Analogue to the sensitivity of geometry change, the sensitivity history matrix with respect to the material parameters is referred to $\mathbf{H}_m$ in Eq. (6.27.2). Moreover, the applied tangential matrices refer to Eq. (4.42) and Eq. (6.25). The sensitivity matrix $\mathbf{S}_m \in \mathbb{R}^{\mathrm{dof} \times 6}$ follows with

$$\mathbf{S}_m = \frac{\mathrm{d}\boldsymbol{\nu}}{\mathrm{d}\mathbf{m}} = -\mathbf{K}^{-1} [\mathbf{P}_m + \mathbf{H}_m]\,. \tag{6.33}$$

6.7. Design Velocity Matrix

The sensitivity analysis determines how sensitive the objective functions and constraints are and monitors their reaction to changes made to the design parameters. Thereby, the continuum mechanical quantities of the objective functions and constraints depend on the FE-nodes. Due to the parameterised CAGD description, cf. Sec. 5.4, the FE-nodes are in turn dependent on the geometric design parameters; the chain rule is applied and the multiplication follows from two parts. The first being that the derivatives relate to the FE-nodes and the second, the derivatives relate to the design parameters. The last part represents the design velocity field, which is introduced in Eq. (6.34). The design velocity matrix $\mathbf{v} \in \mathbb{R}^{\mathrm{dofm} \times \mathrm{dofs}}$ connects the nodal parameters $\mathbf{X} \in \mathbb{R}^{\mathrm{dofm}}$ to the design parameters $\tilde{\mathbf{s}} \in \mathbb{R}^{\mathrm{dofs}}$ with dofs describing the global number of design parameters, i.e.

$$\mathbf{v} = \frac{\partial \mathbf{X}}{\partial \tilde{\mathbf{s}}}\,. \tag{6.34}$$

The open-source software Gmsh is used to generate the mesh in the context of FEM pre-processing. Thereby, the design velocity matrix is determined numerically according to the central difference scheme, which follows as

$$\mathbf{v} \;=\; \frac{\mathbf{X}(\tilde{\mathbf{s}}, \epsilon^{+}) \;-\; \mathbf{X}(\tilde{\mathbf{s}}, \epsilon^{-})}{2\,\epsilon}\,. \tag{6.35}$$

Where ϵ^{-} and ϵ^{+} are the negative and positive perturbation variables.

The numerical evaluation of the design velocity field is implemented in a sensitivity routine, see Listing 6.1, which demonstrates the computation of the design velocity matrix for the CAGD geometry referring to Figure 5.2. The basic geometries applied in this work do not increase the numerical effort. However, it should be noted that a numerical determination in more complex geometries can lead to higher computational costs. In [73, 52] analytical calculations of the design velocity field are described.

6.8. Sensitivity of Continuum Mechanical Quantities

6.8.1. Sensitivity of the First Piola-Kirchhoff Stress

The sensitivity of the First Piola-Kirchhoff Stress $\delta_X \mathbf{P} \in \mathbb{R}^{4\times \mathrm{nel} \times 9 \times \mathrm{dofm}}$ follows by taking into account a change of the geometry $\mathbf{X}$. The multidimensional array refers to the entries in $\mathbf{P}$ (4), the global number of elements (nel), nine Gauss points and the global number of mechanical degrees of freedom (dofm). It follows with

$$\begin{aligned} \delta_X \mathbf{P} \;&=\; \left[\frac{\partial \mathbf{P}}{\partial \mathbf{X}} + \frac{\partial \mathbf{P}}{\partial \mathbf{u}}\,\frac{\mathrm{d}\mathbf{u}}{\mathrm{d}\mathbf{X}} + \frac{\partial \mathbf{P}}{\partial \mathbf{c}_\gamma}\,\frac{\mathrm{d}\mathbf{c}_\gamma}{\mathrm{d}\mathbf{X}}\right]\delta\mathbf{X} \\ &=\; \left[\frac{\partial \mathbf{P}}{\partial \mathbf{X}} + \frac{\partial \mathbf{P}}{\partial \boldsymbol{\nu}}\,\frac{\mathrm{d}\boldsymbol{\nu}}{\mathrm{d}\mathbf{X}}\right]\delta\mathbf{X} \;=\; \left[\frac{\partial \mathbf{P}}{\partial \mathbf{X}} + \frac{\partial \mathbf{P}}{\partial \boldsymbol{\nu}}\,\mathbf{S}_X\right]\delta\mathbf{X}\,, \end{aligned} \tag{6.36}$$

with the partial variations $\dfrac{\partial \mathbf{P}}{\partial \mathbf{X}}$ as well as the sensitivity matrix $\mathbf{S}_X$. The partial variation $\dfrac{\partial \mathbf{P}}{\partial \boldsymbol{\nu}}$ contains the dependency of the primary variables $\boldsymbol{\nu}$, i.e.

$$\frac{\partial \mathbf{P}}{\partial \boldsymbol{\nu}} = \begin{bmatrix} \dfrac{\partial \mathbf{P}}{\partial \mathbf{u}} & \dfrac{\partial \mathbf{P}}{\partial c_\gamma} \end{bmatrix}. \tag{6.37}$$

A detailed outline of the variations is presented in Appendix A.1.1. With the introduced design velocity matrix $\mathbf{v}$ from Eq. (6.34), the geometric sensitivity matrix of the first Piola Kirchhoff stress can be transformed into a defined and reduced design field, i.e.

$$\delta_s \mathbf{P} = \left[\frac{\partial \mathbf{P}}{\partial \mathbf{X}} + \frac{\partial \mathbf{P}}{\partial \boldsymbol{\nu}} \mathbf{S}_X \right] \mathbf{v} \, \delta \tilde{\mathbf{s}} \,, \tag{6.38}$$

so that $\delta_s \mathbf{P} \in \mathbb{R}^{4 \times \mathrm{nel} \times 9 \times \mathrm{dofs}}$.

6.8.2. Sensitivity of the Second Piola-Kirchhoff Stress

The sensitivity of the second Piola-Kirchhoff stress $\delta_X \underline{\mathbf{S}}_K \in \mathbb{R}^{3 \times \mathrm{nel} \times 9 \times \mathrm{dofm}}$ with respect to a change of the nodal coordinates $\mathbf{X}$ is determined. Whereby the symmetry of the second Piola-Kirchhoff stress reduces the dimension. The total partial variation follows with

$$\begin{aligned} \delta_X \underline{\mathbf{S}}_K &= \left[\frac{\partial \underline{\mathbf{S}}_K}{\partial \mathbf{X}} + \frac{\partial \underline{\mathbf{S}}_K}{\partial \mathbf{u}} \frac{\mathrm{d}\mathbf{u}}{\mathrm{d}\mathbf{X}} + \frac{\partial \underline{\mathbf{S}}_K}{\partial \mathbf{c}_\gamma} \frac{\mathrm{d}\mathbf{c}_\gamma}{\mathrm{d}\mathbf{X}} \right] \delta \mathbf{X} \\ &= \left[\frac{\partial \underline{\mathbf{S}}_K}{\partial \mathbf{X}} + \frac{\partial \underline{\mathbf{S}}_K}{\partial \boldsymbol{\nu}} \frac{\mathrm{d}\boldsymbol{\nu}}{\mathrm{d}\mathbf{X}} \right] \delta \mathbf{X} = \left[\frac{\partial \underline{\mathbf{S}}_K}{\partial \mathbf{X}} + \frac{\partial \underline{\mathbf{S}}_K}{\partial \boldsymbol{\nu}} \mathbf{S}_X \right] \delta \mathbf{X} \,, \end{aligned} \tag{6.39}$$

with

$$\frac{\partial \underline{\mathbf{S}}_K}{\partial \boldsymbol{\nu}} = \begin{bmatrix} \dfrac{\partial \underline{\mathbf{S}}_K}{\partial \mathbf{u}} & \dfrac{\partial \underline{\mathbf{S}}_K}{\partial c_\gamma} \end{bmatrix} . \tag{6.40}$$

The partial variations $\frac{\partial \underline{\mathbf{S}}_K}{\partial \mathbf{X}}$, $\frac{\partial \underline{\mathbf{S}}_K}{\partial \boldsymbol{\nu}}$ and $\frac{\partial \underline{\mathbf{S}}_K}{\partial c_\gamma}$ can be found in Appendix A.1.2. Here again, the design velocity matrix $\mathbf{v}$ from Eq. (6.34) is applied to transform the introduced matrix into a defined and reduced design field $\delta_s \underline{\mathbf{S}}_K \in \mathbb{R}^{3 \times \mathrm{nel} \times 9 \times \mathrm{dofs}}$, as follows

$$\delta_s \underline{\mathbf{S}}_K = \left[\frac{\partial \underline{\mathbf{S}}_K}{\partial \mathbf{X}} + \frac{\partial \underline{\mathbf{S}}_K}{\partial \boldsymbol{\nu}} \mathbf{S}_X \right] \mathbf{v} \, \delta \tilde{\mathbf{s}} \,. \tag{6.41}$$

6.8.3. Sensitivity of the First Principal Stress

In the context of optimisation problems within this thesis, the first principal stress of the Cauchy stress tensor T_I is considered as an objective function and as a constraint. Thus, the total variation of the first principal stress $\delta_s T_I \in \mathbb{R}^{1 \times \mathrm{nel} \times 9 \times \mathrm{dofm}}$ is required and follows with

$$\delta_s T_I = \frac{\partial T_I}{\partial \mathbf{T}} \, \delta_s \mathbf{T} \,, \tag{6.42}$$

wherein the variation of the Cauchy stress with respect to the design parameters follows analogue to the sensitivity of the first and second Piola-Kirchhoff stress with

$$\delta_s \mathbf{T} = \left[\frac{\partial \mathbf{T}}{\partial \mathbf{X}} + \frac{\partial \mathbf{T}}{\partial \boldsymbol{\nu}} \mathbf{S}_X\right] \mathbf{v}\, \delta \tilde{\mathbf{s}}\,, \tag{6.43}$$

and the dimension $\delta_s \mathbf{T} \in \mathbb{R}^{4 \times \mathrm{nel} \times 9 \times \mathrm{dofs}}$. Furthermore, the equation contains the partial variation of the Cauchy stress with respect to the primary variables the following components

$$\frac{\partial \mathbf{T}}{\partial \boldsymbol{\nu}} = \begin{bmatrix} \dfrac{\partial \mathbf{T}}{\partial \mathbf{u}} & \dfrac{\partial \mathbf{T}}{\partial c_\gamma} \end{bmatrix}. \tag{6.44}$$

Whereby reference is made to the variations in Appendix A.1.3. Moreover, the partial variation of the first principal stress from Eq. (3.42) with respect to the Cauchy stress in Voigt notation results in

$$\frac{\partial T_I}{\partial \mathbf{T}} = \frac{1}{2}\mathbf{1} + \frac{-\dfrac{1}{4} I_T \,\mathbf{1} + \mathbf{T}^{\mathrm{T}}}{\sqrt{\left(\dfrac{I_T}{2}\right)^2 - II_T}}\,. \tag{6.45}$$

6.8.4. Sensitivity of the Area

Within the framework of structural optimisation, the sensitivity of the area is a helpful measure for the objective functions or the constraints. Thus, the area depends on the change of the coordinates, respectively, the chosen design parameters. The area can be calculated by the sum of the total element areas, i.e.

$$A = \bigcup_{e=1}^{\mathrm{nel}} \sum_{I=1}^{\mathrm{nn}} \int_{\Omega_e} \mathrm{d}A\,. \tag{6.46}$$

The variation of the area with respect to the design parameters $\delta_s A \in \mathbb{R}^{1 \times \mathrm{dofs}}$ follows with the variations of the ansatz functions, cf. Eq. (4.18), so that

$$\delta_s A = \bigcup_{e=1}^{\mathrm{nel}} \sum_{I=1}^{\mathrm{nn}} \int_{\Omega_e} \mathbf{L}^I \,\mathrm{d}A\,. \tag{6.47}$$

6.9. Concluding Remarks for the Sensitivity Analysis

This section presents the time-efficient strategy of the variational sensitivity analysis. Considering the equilibrium conditions from the structural analysis, the requirements for the sensitivity of geometry, material and history can be obtained in this section. Based on this, the following equations are provided:

- *The tangential matrices are derived analogously to the structural analysis first via the partial variations of the weak forms and finally discretised with the same approaches. In the process, the pseudo-load, history field and sensitivity matrices are derived for geometric and material changes.*
- *The design velocity matrix provides the transfer from geometrical sensitivities to the dependency of chosen design parameters. Due to the design velocity field, the sensitivity evaluation can be reduced to the most relevant geometric changes, which leads to a very time-efficient method.*
- *Sensitivity of the second Piola-Kirchhoff stress.*
- *Sensitivity of the first principal stress.*
- *Sensitivity of the area.*

```
function [v]=sensidX(lc,mesh,X)
% dofm                          overall number FE-coordinates
% ϵ                             pertubation
% lc                            mesh size
% X=[X1; X2; X3; X4=X3]         design parameters

% mesh = structure array with:
% coord: [dofm double]          matrix FE-node coordinates

% initialisation
ϵ=10^(-4);
v=zeros(size(mesh.coord,1) × 2,3);

% start finite difference loop
for t=1:3
X_a=X;
X_b=X;
X_a(t)=X(t)+ϵ;
X_b(t)=X(t)-ϵ;

% new FE-nodes coordinates: mesh.coord_vec_a
[mesh]=Mesh(lc,X_a);
mesh.coord_vec_a=zeros(size(mesh.coord,1) × 2,1);
p=1;
for i=1:size(mesh.coord,1)
for k=1:2
mesh.coord_vec_a(p)=mesh.coord_vec_a(p)+mesh.coord(i,k);
p=p+1;
end
end

% new FE-nodes coordinates: mesh.coord_vec_b
[mesh]=Mesh(lc,X_b);
mesh.coord_vek_b=zeros(size(mesh.coord,1) × 2,1);
p=1;
for i=1:size(mesh.coord,1)
for k=1:2
mesh.coord_vec_b(p)=mesh.coord_vec_b(p)+mesh.coord(i,k);
p=p+1;
end
end

% design velocity matrix
v(:,t) = (mesh.coord_vec_a - mesh.coord_vec_b)/(2 × ϵ);
% end finite difference loop
end
```

Listing 6.1: Sensitivity routine for design velocity matrix **v**

7. Numerical Investigations

In this section, the properties of the proposed diffusion-controlled degradation model are discussed. Using small examples, the presented model is assessed for plausibility, sensitivities are controlled and convergence behaviour is examined.

7.1. Introduction to Numerical Investigations

The objective of this section is to examine the mechanical-chemical-degradation model for plausibility with the use of representative examples. The general coupling between the diffusion of concentrations and the mechanical response is analysed. Therefore, structural analysis is used to assess a boundary value problem. This also deals with the verification of the analytically derived and implemented sensitivities, as well as the convergence of the solutions determined by structural analysis is examined.

7.2. Coupled Boundary Value Problem

In the following, the correlations between mechanical impact and diffusion-driven degradation processes are investigated based on an example including one element and two different sets of boundary conditions as shown in Figure 7.1. The example is calculated with a given x-displacement of $\Delta\, u = -0.2\,\mathrm{cm}$ at the left edge using Dirichlet boundary conditions, see Figure 7.1a, and further a constant line load is applied as shown in Figure 7.1b. The line load is a result of the given nodal loads over the Neumann boundary. To start from an identical deformation state, the force is set to a value of $F = -0.45\,\mathrm{MN}$, so that a displacement of $-0.2\,\mathrm{cm}$ occurs. Besides the mechanical boundary conditions, concentrations are applied via the left Dirichlet edge. For both examples, a quadratic increase over time of the concentration c^0_γ is assumed as shown in Figure 7.2. Thus, the degradation process, triggered by the concentrations, is identically established for both

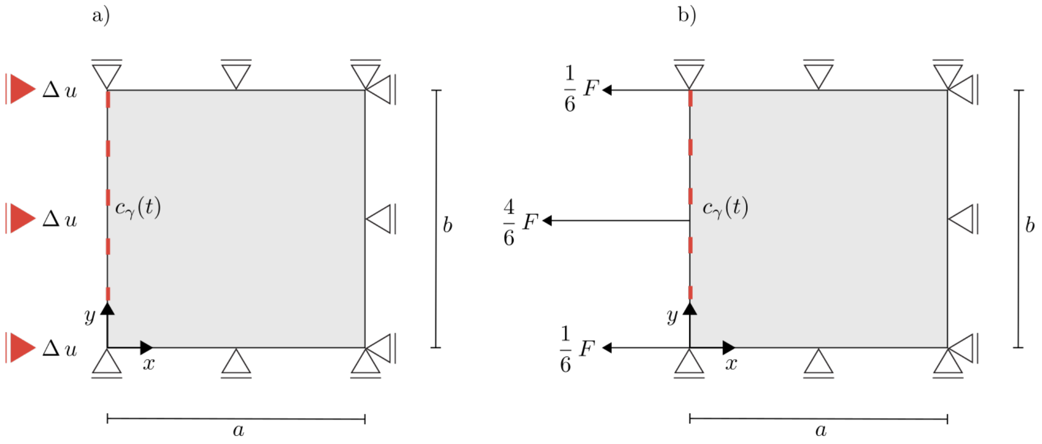

Figure 7.1.: a) Dirichlet boundary conditions Δu and b) Neumann boundary conditions F.

examples. The applied material parameters are shown in Table 7.1. The example is simulated over 25 days with a time increment of $\Delta t = 0.02\,\mathrm{d}$ for the time integration scheme. Nevertheless, the total deformation behaves differently due to the two boundary conditions. First, the observations on the boundary value problem referring to Figure 7.1a with given displacements follow. The total deformation represented by J is constant, as the boundary condition does not allow shrinkage. The elastic deformation changes inversely so that the kinematic condition $J_e = [J_d]^{-1} J$ is fulfilled. As a result, the stress T_{xx} increases because the deformation is fixed, whereas the degradation decreases.

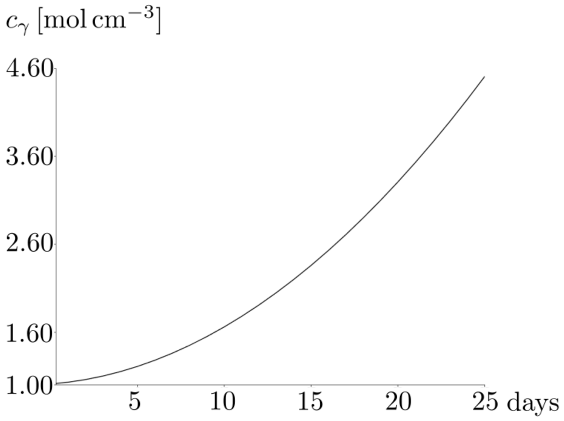

Figure 7.2.: Dirichlet boundary condition for the concentration with the quadratic function $c_\gamma(\mathrm{t}) = 0.005\mathrm{t}^2 + 0.005\mathrm{t} + 1$ over time.

Table 7.1.: Material and geometry parameters.

E	=	$2\,\mathrm{MN\,cm^{-2}}$
ν	=	0.2
ρ_0^*	=	$300\,\mathrm{kg\,cm^{-3}}$
M_γ	=	$10\,\mathrm{kg\,mol^{-1}}$
D	=	$30\,\mathrm{cm^2\,d^{-1}}$
c_γ^0	=	$1\,\mathrm{mol\,cm^{-3}}$
a	=	1 cm
b	=	1 cm

Furthermore, the observations on the second boundary value problem illustrated in Figure 7.1b with given loads continues. As a result, the total deformation gradient decreases over time, whereas the stress is constant. Nevertheless, the elastic deformation increases since the concentrations change the density and thus, the material behaviour.

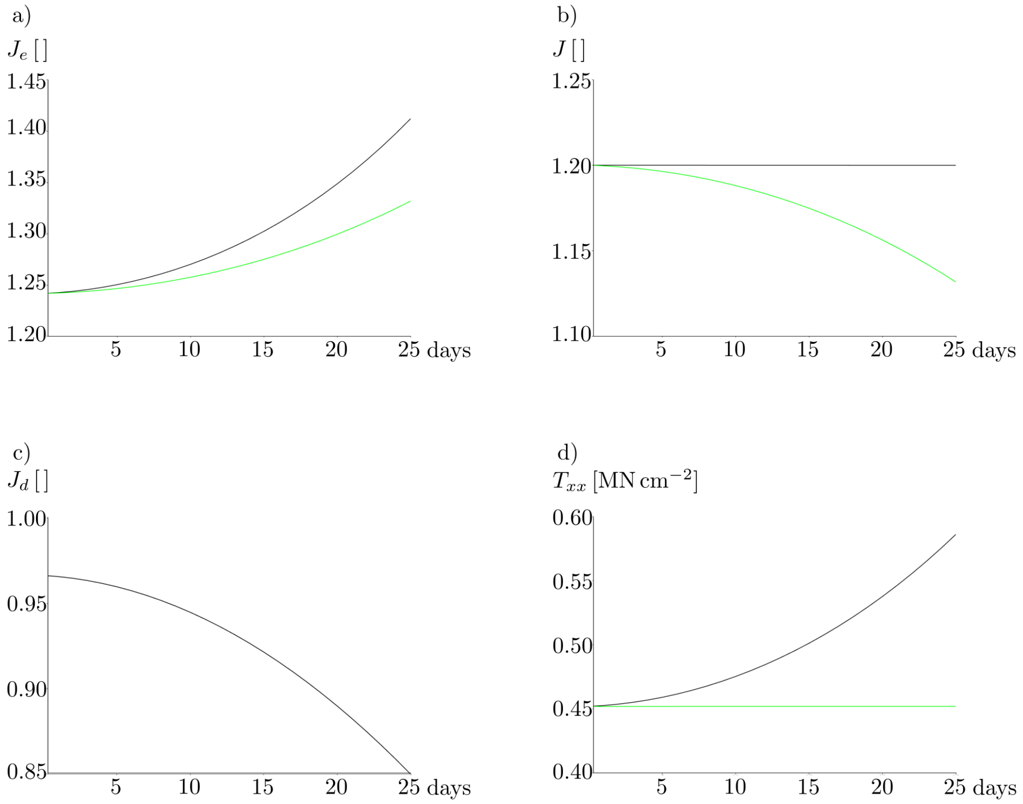

Figure 7.3.: Evaluation of the boundary condition related to Figure 7.1a with black line and related to the boundary condition in Figure 7.1b with green line with a time slot of 25 days. a) Determinant of the elastic contribution to the deformation gradient J_e over time. b) Determinant of the total deformation gradient J over time. c) Determinant of the degradation contribution to the deformation gradient J_d. d) Cauchy stress in x-direction T_{xx} in MN cm^{-2} over time.

Overall, the example shows a reasonable mechanical correlation between the loads, deformations and stresses. The evaluation illustrates that the split of the deformation into an elastic and degradation contribution allows a deeper insight into the effects of the concentrations. Thus, in this example it becomes clear that the density and the material behaviour are affected by the concentrations.

7.3. Investigations on Sensitivity Matrix for Geometric Changes

The design sensitivity matrix shows the impact of geometry changes on the displacement and concentrations in the structure, resulting from the FEM investigation. The matrix can be determined with two approaches, either a numerical or an analytical approach. The analytical calculation is summarised in Sec. 6.6.2, which introduces the sensitivity matrix $\mathbf{S}_X$. In this section, the numerical approach is investigated using the FDM. The following approaches can determine the numerical derivatives

$$\begin{aligned}
\mathbf{S}_d^c &= \frac{\mathbf{u}(\mathbf{X},\epsilon^+) - \mathbf{u}(\mathbf{X},\epsilon^-)}{2\,\epsilon} && \text{central difference} \\
\mathbf{S}_d^f &= \frac{\mathbf{u}(\mathbf{X},\epsilon^+) - \mathbf{u}(\mathbf{X})}{\epsilon} && \text{forward difference} \\
\mathbf{S}_d^b &= \frac{\mathbf{u}(\mathbf{X}) - \mathbf{u}(\mathbf{X},\epsilon^-)}{\epsilon} && \text{backward difference.}
\end{aligned} \tag{7.1}$$

The approximations are calculated by difference quotients with a selected perturbation ϵ. In the following, the numerical approximations are derived with different perturbation factors to achieve the highest precision for the numerical approximation of the gradients and prove the correct implementation of the derived gradients for the analytical approach. For this purpose, the boundary value problem presented in Figure 7.1b is used to determine the sensitivity matrix with the analytical and numerical approaches. The material parameters listed in Table 7.1 are used for the calculation; however, only the first five days of concentration exposure as shown in Figure 7.2 are simulated. This boundary value problem is chosen to activate both the chemical and mechanical influence. Thus, the numerical approach can be used to verify whether an inhomogeneous, time-dependent and coupled problem determines the appropriate sensitivities of displacement and concentration with respect to changes in geometry. The analytical calculation provides the sensitivity of the concentration and displacements by modifications of the node coordinates, summarised in the sensitivity matrix $\mathbf{S}_X$. Table 7.2 shows the relative error between the analytical derived design sensitivity matrix $\mathbf{S}_X$ and the numerical sensitivity matrix using different perturbation variables and different FDM approaches ($\mathbf{S}_d^c$, $\mathbf{S}_d^f$, $\mathbf{S}_d^b$), whereby the Euclidean norm is utilised. The perturbations in the range 10^{-7} to 10^{-8} lead to the smallest relative errors between the numerical and analytical sensitivity matrix. Nevertheless, it is clear that the central difference FDM scheme determines the most robust comparison matrix. The FDM offers a simple way to calculate the sensitivity of the parameters, yet causing a very high computational effort, the computational time required is outlined in Sec. 9.2.4.

Table 7.2.: Calculation of the relative error between the analytical design sensitivity matrix $\mathbf{S}_X$ and the numerical sensitivity matrix using different perturbation variables and different FDM approaches ($\mathbf{S}_d^c$, $\mathbf{S}_d^f$, $\mathbf{S}_d^b$). The framed area shows optimal perturbations.

$\frac{\vert\vert\mathbf{S}_d^c - \mathbf{S}_X\vert\vert}{\vert\vert\mathbf{S}_X\vert\vert}$	$\frac{\vert\vert\mathbf{S}_d^f - \mathbf{S}_X\vert\vert}{\vert\vert\mathbf{S}_X\vert\vert}$	$\frac{\vert\vert\mathbf{S}_d^b - \mathbf{S}_X\vert\vert}{\vert\vert\mathbf{S}_X\vert\vert}$	ϵ
1.96×10^{-4}	1.78×10^{-2}	1.78×10^{-2}	1×10^{-2}
1.96×10^{-6}	1.78×10^{-3}	1.78×10^{-3}	1×10^{-3}
1.04×10^{-7}	1.78×10^{-4}	1.78×10^{-4}	1×10^{-4}
1.04×10^{-7}	1.78×10^{-5}	1.78×10^{-5}	1×10^{-5}
1.04×10^{-7}	1.78×10^{-6}	1.78×10^{-6}	1×10^{-6}
1.04×10^{-7}	1.76×10^{-7}	1.76×10^{-7}	1×10^{-7}
1.08×10^{-7}	1.31×10^{-7}	1.18×10^{-7}	1×10^{-8}
4.65×10^{-7}	8.78×10^{-7}	1.10×10^{-6}	1×10^{-9}

Furthermore, due to the small relative errors in all procedures, it can be shown that the analytical solution is properly implemented.

7.4. Investigations on Sensitivity Matrix for Material Changes

The sensitivity matrix regarding material parameters shows the influence of a material modification on the primary variables, i.e. displacements and concentrations, which are the results of the structural analysis. As in the previous section, the example presented in Figure 7.1b is used to compare the numerical and analytical derived sensitivity matrix. The analytical sensitivity matrix $\mathbf{S}_m$ is evaluated in Sec. 6.6.3 and the numerical approximations follow with

$$
\begin{aligned}
\mathbf{S}_m^c &= \frac{\mathbf{u}(\mathbf{m}, \epsilon^+) - \mathbf{u}(\mathbf{m}, \epsilon^-)}{2\,\epsilon} && \text{central difference} \\
\mathbf{S}_m^f &= \frac{\mathbf{u}(\mathbf{m}, \epsilon^+) - \mathbf{u}(\mathbf{m})}{\epsilon} && \text{forward difference} \\
\mathbf{S}_m^b &= \frac{\mathbf{u}(\mathbf{m}) - \mathbf{u}(\mathbf{m}, \epsilon^-)}{\epsilon} && \text{backward difference.}
\end{aligned}
\tag{7.2}
$$

In Table 7.3, it can be concluded that the smallest relative error occurs in the perturbation range of 10^{-6} to 10^{-7}. Due to the low deviation, the analytically derived material sensitivity matrix can be assumed to be correctly calculated and implemented.

Table 7.3.: Calculation of the relative error between the analytical material sensitivity matrix $\mathbf{S}_m$ and the numerical sensitivity matrix using different perturbation variables and different FDM approaches ($\mathbf{S}_m^c$, $\mathbf{S}_m^f$, $\mathbf{S}_m^b$). The framed area shows optimal perturbations.

$\frac{\|\|\mathbf{S}_m^c - \mathbf{S}_m\|\|}{\|\|\mathbf{S}_m\|\|}$	$\frac{\|\|\mathbf{S}_m^f - \mathbf{S}_m\|\|}{\|\|\mathbf{S}_m\|\|}$	$\frac{\|\|\mathbf{S}_m^b - \mathbf{S}_m\|\|}{\|\|\mathbf{S}_m\|\|}$	ϵ
6.72×10^{-5}	7.99×10^{-3}	8.13×10^{-3}	1×10^{-2}
6.73×10^{-7}	8.05×10^{-4}	8.07×10^{-4}	1×10^{-3}
3.33×10^{-8}	8.06×10^{-5}	8.06×10^{-5}	1×10^{-4}
3.26×10^{-8}	8.06×10^{-6}	8.06×10^{-6}	1×10^{-5}
3.25×10^{-8}	8.05×10^{-7}	8.07×10^{-7}	1×10^{-6}
3.25×10^{-8}	8.58×10^{-8}	7.98×10^{-8}	1×10^{-7}
1.08×10^{-7}	1.66×10^{-7}	1.63×10^{-7}	1×10^{-8}
6.67×10^{-7}	2.00×10^{-6}	1.31×10^{-6}	1×10^{-9}

7.5. Investigations on Convergence

The coupled mechanical-chemical-degradation model applies both time and space discretisation. In the following section, the convergence of the solutions, the displacements and concentrations are analysed depending on the number of elements and on the number of time steps. Therefore, the boundary value problem printed in Figure 7.4 is evaluated.

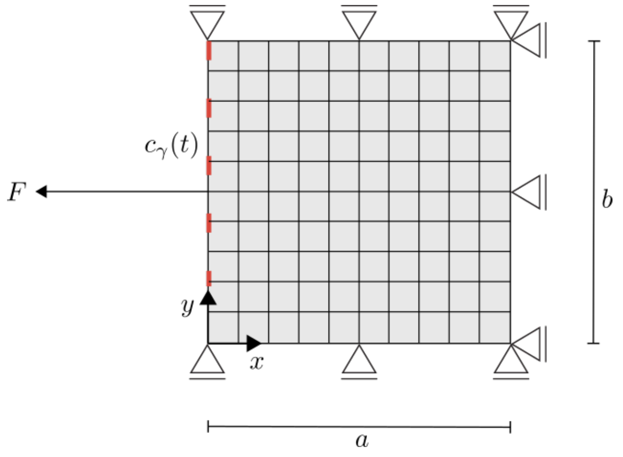

Figure 7.4.: Boundary value problem with a nodal force F and Dirichlet boundary conditions for the concentration $c_\gamma(t)$ on the left edge of the structure. Here, the structure is meshed with 100 elements.

The material parameters listed in Table 7.1 are used for the calculation; however, only the first day of concentration exposure, as shown in Figure 7.2, is simulated. Furthermore, the force is set to a value of $F = -0.01\,\mathrm{MN}$. In order to see the effects of the discretisation, the example is calculated with different time steps and number of elements. Table 7.4

shows the solution of the concentrations and Table 7.5 shows the x-displacement, both values are evaluated in the middle point of the structure, i.e. $(0.5\,a, 0.5\,b)$. The solutions are determined using different meshes; the applied number of elements and time steps vary. The blue area shows the range in which the solution variables can be evaluated as sufficiently accurate under consideration of computational time effort and accuracy of the solution. It is clear that the convergence of concentrations is predominantly dependent on temporal discretisation yet, the convergence of displacement depends mainly on spatial discretisation since only the evolution of the concentration is considered in the structural problem. However, since the processes are coupled, both the spatial discretisation and the time increments for the time integration scheme must be selected small. In this example, 36 elements with a time increment of 0.02 d achieve a converged result. With the convergence study at hand, the mesh sizes for the coming examples are selected. Both convergence studies are illustrated in Figure 7.5.

Table 7.4.: Solution of the concentrations $[\mathrm{mol\,cm^{-3}}]$ in the middle point of the structure, i.e. $(0.5\,a, 0.5\,b)$ for different space and time increments.

	Convergence concentrations				
time [d]	spatial				
	4 elements	16 elements	36 elements	64 elements	100 elements
1	4.962×10^{-3}	4.961×10^{-3}	4.962×10^{-3}	4.962×10^{-3}	4.962×10^{-3}
0.1	4.988×10^{-3}	4.986×10^{-3}	4.987×10^{-3}	4.987×10^{-3}	4.987×10^{-3}
0.02	4.983×10^{-3}	4.981×10^{-3}	4.982×10^{-3}	4.982×10^{-3}	4.982×10^{-3}
0.01	4.983×10^{-3}	4.981×10^{-3}	4.982×10^{-3}	4.982×10^{-3}	4.982×10^{-3}
0.005	4.983×10^{-3}	4.981×10^{-3}	4.982×10^{-3}	4.982×10^{-3}	4.982×10^{-3}
0.001	4.983×10^{-3}	4.981×10^{-3}	4.982×10^{-3}	4.982×10^{-3}	

Table 7.5.: Solution of the x-displacement in the middle point of the structure, i.e. $(0.5\,a, 0.5\,b)$ for different space and time increments.

	Convergence displacements				
time [d]	spatial				
	4 elements	16 elements	36 elements	64 elements	100 elements
1	-1.59×10^{-3}	-1.79×10^{-3}	-1.80×10^{-3}	-1.79×10^{-3}	-1.79×10^{-3}
0.1	-1.59×10^{-3}	-1.79×10^{-3}	-1.80×10^{-3}	-1.79×10^{-3}	-1.79×10^{-3}
0.02	-1.59×10^{-3}	-1.79×10^{-3}	-1.80×10^{-3}	-1.79×10^{-3}	-1.79×10^{-3}
0.01	-1.59×10^{-3}	-1.79×10^{-3}	-1.80×10^{-3}	-1.79×10^{-3}	-1.79×10^{-3}
0.005	-1.59×10^{-3}	-1.79×10^{-3}	-1.80×10^{-3}	-1.79×10^{-3}	-1.79×10^{-3}
0.001	-1.59×10^{-3}	-1.79×10^{-3}	-1.80×10^{-3}	-1.79×10^{-3}	-1.79×10^{-3}

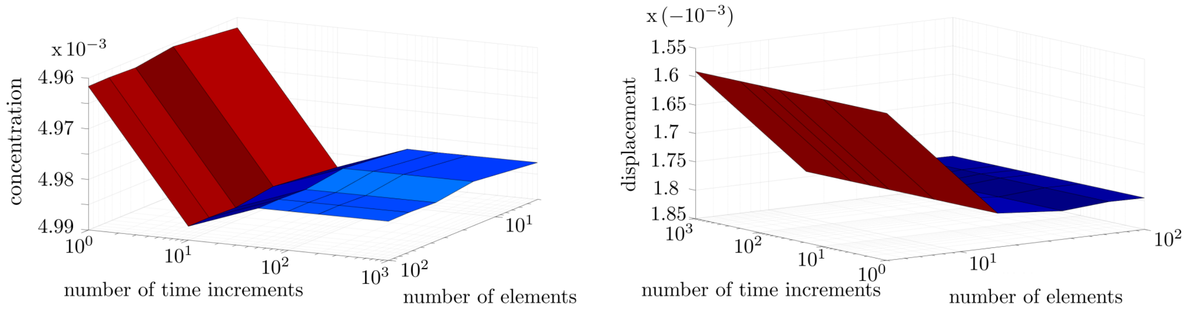

Figure 7.5.: Graphical illustration of the spatial and temporal convergence.

7.6. Concluding Remarks on the Numerical Investigations

The correlation between the degradation and the established kinematics as well as the stresses can be evaluated as plausible. This statement is based on the evaluations of the coupled problem in Sec. 7.2. In particular, the influence of degradation can be clarified with the help of the multiplicative decomposition of the deformation gradient into an elastic and a growth part. Thus, the deformation caused by degradation processes can be quantified using the determinant of the degradation contribution to the deformation gradient J_d.

Furthermore, the analytically determined sensitivities can be evaluated as accurately implemented for the sensitivity of the design and the sensitivity of the material parameters, cf. Sec. 7.3 and Sec. 7.4. The analytical approach represents a considerable time efficiency for the application of optimisation tasks for the further course of this work.

In addition, Sec. 7.5 provides an estimation of mesh resolution for spatial discretisation and the time steps for the time integration. On this basis, the discretisation chosen for the following examples is as efficient as possible.

8. Examples of Structural Analysis

In this section, the coupled effects of diffusion leading to the degradation of material are discussed. To outline the possible use of such a model, common material degradation processes that occur particularly in the building industry are referred.

8.1. Introduction to Examples of Structural Analysis

The broadly chosen model approach makes it possible to address different application areas with mechanical-chemical induced degradation processes. However, within the following, two fields of possible applications in the framework of civil engineering are explained in more detail. In the construction industry, the use of cement as a binder for the production of mortar or concrete is common. The material properties depend on the strength development during the hydration process, whereby in particular calcium silicate hydrate, the so-called C-H-S phase, is produced, see [126]. Two common occurring problems in the building industry, characterised by diffusion-driven material degradation, are addressed in a short overview of the state-of-the-art:

- *Calcium leaching,*
- *Chemical attack.*

The mechanism of calcium dissolution from the hardened cement paste is called *calcium leaching*. In this process, C-H-S phases are decalcified and thus, serious changes in the material properties can occur. For example, long-term exposure to water, with a lower calcium concentration than the equilibrium concentration, can trigger calcium hydroxide crystals. As a result of leaching, materials degrade and the pore volume increases, as published among others in [65]. Pores in the range of 100 nm to 1 µm can occur, see [78], thus having a considerable influence on the mechanical properties of the concrete. A number of publications demonstrate the use of a diffusion-controlled chemically coupled model to simulate calcium leaching, see [51, 83, 146]. In [49], a simplified numerical model of calcium leaching is presented, which concentrates on the chemical state variable calcium and the kinetics of the leaching process. This model considers time-dependent chemical processes and gives an outlook on the possibility of a simple coupling in an FE-algorithm. [78] presents a chemo-mechanical model for the numerical simulation of calcium leaching in concrete. He emphasises the effects of the chemical degradation on the pore volume and the mechanical stability of concrete. A damage function is used for constitutive modelling of the chemo-mechanically degraded material.

A common *chemical attack* can occur for example within wastewater environments. Hydrogen sulfide (H_2S) releases from the wastewater and biodegradable element sulfur is absorbed into the bio-film covering the surface of the wastewater components. Bacteria are formed leading to a reduction of the pH-value. Elementary sulfur and a low pH-value are ideal living conditions for so-called sulfur-oxidising bacteria (Thiobacillus thiooxidans). These bacteria produce sulfuric acid (H_2S0_4), causing a powerful attack on concrete and cement mortar. The chemical attack on concrete triggered by bacteria results in bio-degradation and thus, to structural damage. The process of chemical attacks on concrete is well-known, see e.g. [106, 69, 99]. [143] presents a model for degradation of concrete triggered by sulfuric acid attack wherein a coupling between chemical reactions and the diffusion of different species are implemented. Further publications, which present models for degradation by biogenic organic acids, can be found, e.g. [37, 129].

In the context of this work, diffusion processes of chemical concentrations causing material degradation are considered in a coupled mechanical model. A general approach is chosen to address different fields. This work, therefore, provides a basis for possible applications of specific chemical processes, such as calcium leaching or chemical attacks. The boundary problem is motivated by the concept of analysing the chemical influence on hollow concrete blocks since concrete is a permeable medium that allows the inflow of concentrations and is susceptible to chemical degradation, such as in calcium leaching processes.

8.2. Structure with a Hole

The objective of this example is the investigation on the mechanical effects triggered by chemical concentrations in a structure with a hole. The boundary value problem is illustrated in Figure 8.1a. The material degradation takes place gradually. Hence, the calculation is accelerated by applying the diffusion rate per day and thus, the evaluation per day [d]. The computation runs over 40 d in total. The discretisation is chosen fine to generate accurate results, as outlined in Sec. 7.5. Therefore, the mesh is created with 72 elements as shown in Figure 8.1a and a time increments of 0.02 d is applied for the time integration.

A concentration inflow is considered on the left side of the structure, and the chemicals are increasing over the days as printed in Figure 8.1c. On the right side of the structure the concentration outflow is set to a constant Dirichlet boundary condition with the value of the initial concentration c_γ^0. The concentration contour plot of the last time step is shown in Figure 8.1b. Fixed displacements enable a stable mechanical environment, cf. Figure 8.1a. No specific chemical process is described in this example; however, the material parameters used in Table 8.1 are based on common values for the concrete and the orders of magnitude for chemical diffusion processes. In Figure 8.2a the deformation induced by the concentrations is evaluated and the determinant of the degradation contribution to the deformation gradient, $J_d = \dfrac{\rho_0}{\rho^*}$, is represented. The deformation causes stresses in the structure as the first principal stress of the Cauchy stress T_I shows in a contour plot in Figure 8.3a. The main material degradation occurs near the inlet area due to the material degradation triggered by a high concentration of chemicals. Nevertheless, as a result of the shape, the maximum stress is in marked point A, the area close to the hole. Both the degradation and the first principal stress are evaluated in this point A over time, see Figures 8.2b and 8.3b. This example shows the coupling between a diffusion process and deformations and illustrates the harmful effects of chemical substances. Especially long-term exposure to diffusion processes can cause gradual damage.

Table 8.1.: Material and geometry parameters.

E	$=$	$2\,\mathrm{MN\,cm^{-2}}$
ν	$=$	0.2
ρ_0^*	$=$	$300\,\mathrm{kg\,cm^{-3}}$
M_γ	$=$	$10\,\mathrm{kg\,mol^{-1}}$
D	$=$	$30\,\mathrm{cm^2\,d^{-1}}$
c_γ^0	$=$	$1\,\mathrm{mol\,cm^{-3}}$
a	$=$	$5\,\mathrm{cm}$
b	$=$	$5\,\mathrm{cm}$

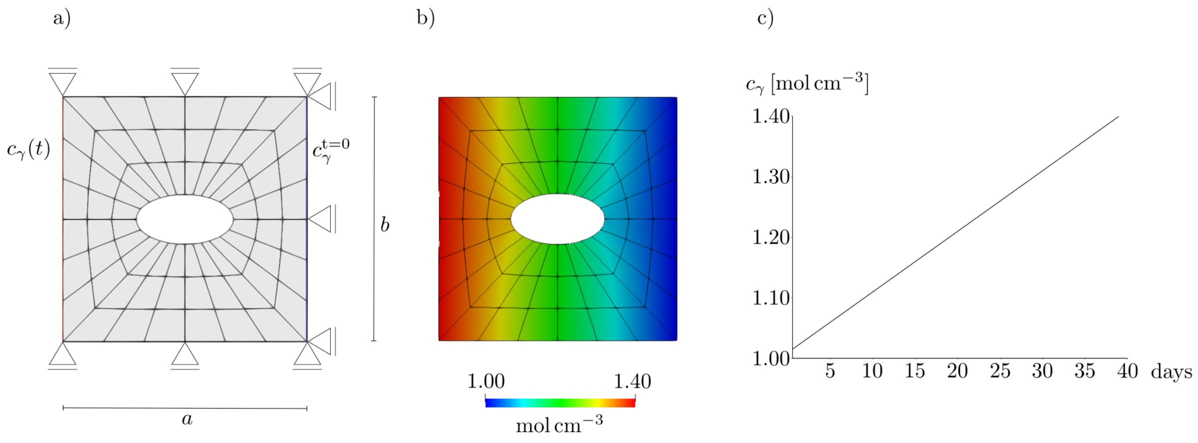

Figure 8.1.: a) Dirichlet boundary conditions and mesh of a structure with a hole. b) Contour plot of the concentrations in the last time step. c) Illustration of the concentrations $c_\gamma(\mathrm{t})$ over 40 d with a linear increase in the applied Dirichlet boundary conditions.

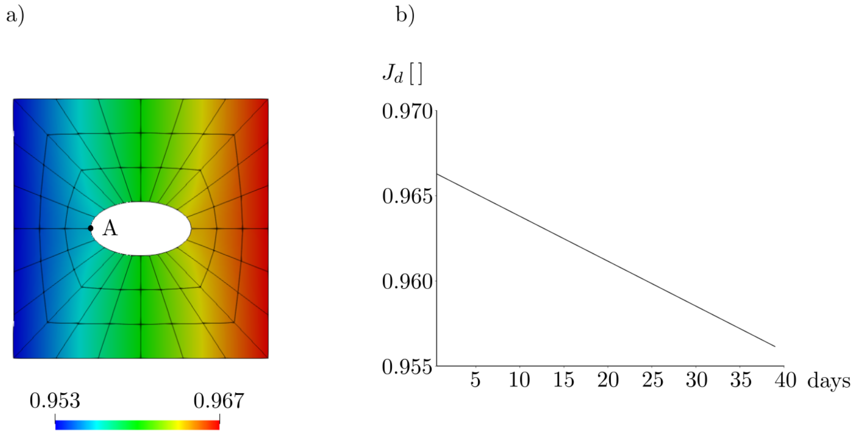

Figure 8.2.: a) Contour plot of degradation J_d in the last time step. b) Evaluation of the degradation J_d in point A over time triggered by the concentration c_γ.

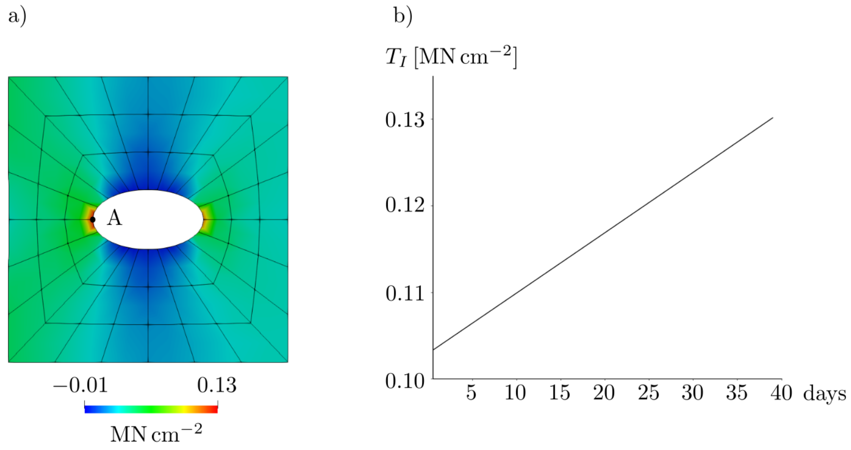

Figure 8.3.: a) Contour plot of first principal Cauchy stress T_I in the last time step. b) Evaluation of the first principal Cauchy stress T_I in point A over time triggered by the degradation J_d.

8.3. Concluding Remarks on the Structural Analysis Examples

In this section, an example for the application of the developed diffusion-driven degradation model is presented. The purpose of this section is to simulate a time-dependent problem due to environmental influences and, in particular, to illustrate the mechanical effects in the form of stresses. The aim of the example is to illustrate how environmental influences can gradually change the stresses in a structure and demonstrate how the load-bearing behaviour may no longer be guaranteed.

The example simulates a structure with a hole with a chemical diffusion. The concentrations lead to material degradation and deformations, which in turn trigger the stresses in the structure and create stress peaks at the area of the hole. This example is used as the basis for a subsequent optimisation task.

9. Examples of Shape Optimisation

The developed model of a diffusion-driven degradation model, which is embedded in an algorithm for the calculation of structural shape optimisation, is applied. The examples provided have a practical reference and are optimised under the influence of chemical concentrations.

9.1. Introduction to the Examples of Shape Optimisation

Shape optimisation of structures can provide a better understanding of mechanical requirements and repeated efficiency. For this reason, examples of shape optimisation of the diffusion-driven degradation model are presented in this section. The first example refers to an unfilled structure, similar to a hollow concrete block, loaded with chemical substances. Whereby the optimised shape of the brick is evaluated in such a way that the maximum stress caused by the concentrations is reduced, though still no additional material needs to be used. A further bridge-like structure is analysed regarding an optimised shape, where materials are saved and the load-bearing capacity is still fulfilled.

With the help of the following examples, it is shown that the shape plays a relevant role in fulfilling the mechanical requirements, even when diffused concentrations are taken into account. The examples serve to illustrate possible practical applications. Finally, the analytically determined gradients, which are applied in the context of structural optimisation, can be verified employing comparative numerical results.

9.2. Optimisation of a Structure with a Hole

The shape optimisation of the structure with a hole from Sec. 8.2 is discussed in detail in the following sections. The objective of the optimisation task is to reduce the stress resulting from the degradation processes. Hence, the maximum first principal stress in the Gauss point is applied as the objective function. The restriction is defined in such a way that the area is not allowed to change significantly. Therefore, the objective function $\tilde{J}(\tilde{\mathbf{s}}, \boldsymbol{\nu}(\tilde{\mathbf{s}}))$ and constraint $\tilde{g}(\tilde{\mathbf{s}}, \boldsymbol{\nu}(\tilde{\mathbf{s}}))$ are established as follows

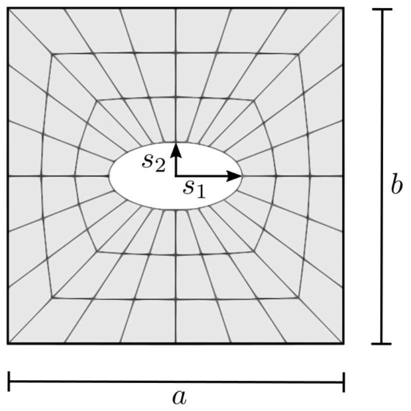

Figure 9.1.: Shape optimisation.

Table 9.1.: Input parameters for the optimisation algorithm.

threshold	$\bar{A}$	0.005	
limit values	$\tilde{\mathbf{s}}^u$	[1.3; 0.8]	cm
	$\tilde{\mathbf{s}}^l$	[0.7; 0.2]	
initial design	$\tilde{\mathbf{s}}$	[1; 0.5]	cm
geometric values	$a = b$	5	cm

$$\begin{aligned} \tilde{J}(\tilde{\mathbf{s}}, \boldsymbol{\nu}(\tilde{\mathbf{s}})) &= T_I^{\max} \\ \tilde{g}(\tilde{\mathbf{s}}, \boldsymbol{\nu}(\tilde{\mathbf{s}})) &= \left| \frac{A^{\text{ini}} - A}{A^{\text{ini}}} \right| - \bar{A}\,, \end{aligned} \tag{9.1}$$

wherein $T_I^{\max}$ is the maximal first principal stress in the Gauss points, A^{ini} is the initial area, A is the actual area and $\bar{A}$ is a defined threshold. Both the objective function and the constraint must be calculated using the solutions of the structural analysis as they are dependent on the field variables $\boldsymbol{\nu}$, cf. Sec. 8.2. Furthermore, the optimisation task depends on the design parameters, the axes of the ellipse (s_1, s_2) as printed in Figure 9.1, which are altered to minimise the objective function. The optimisation problem reads

$$\begin{array}{lcccl} \min \tilde{J}(\tilde{\mathbf{s}}, \boldsymbol{\nu}(\tilde{\mathbf{s}})) & : \quad \tilde{g} & \leq & 0 & \text{inequality constraint} \\ \tilde{\mathbf{s}} \in \mathbb{R}^{\text{dofs}},\ \boldsymbol{\nu} \in \mathbb{R}^{\text{dof}} & \tilde{\mathbf{s}}^l & \leq & \tilde{\mathbf{s}} \leq \tilde{\mathbf{s}}^u & \text{limit values.} \end{array} \tag{9.2}$$

The parameters of the hole are the design parameters $\tilde{\mathbf{s}} = \begin{bmatrix} s_1 & s_2 \end{bmatrix}^{\mathrm{T}}$, with defined upper limit values $\tilde{\mathbf{s}}^u = \begin{bmatrix} s_1^u & s_2^u \end{bmatrix}^{\mathrm{T}}$ and lower limit values $\tilde{\mathbf{s}}^l = \begin{bmatrix} s_1^l & s_2^l \end{bmatrix}^{\mathrm{T}}$. The optimisation algorithm applies the input parameters listed in Table 9.1.

9.2.1. Parameter Calibration Sensitivity of the Objective Function

For the solution to the optimisation task, the variations of the objective function and the inequality constraint with respect to the design parameters are required, as described in Sec. 5.5.1. Both gradients can be calculated either analytically or numerically. The maximum first principal stress is used as the objective function and the change of the area is used as the inequality constraint. Therefore, Eq. (6.42) and Eq. (6.47) are applied for the analytical derived gradients $\nabla \tilde{J}$ and $\nabla \tilde{g}$, i.e.

$$\begin{aligned} \nabla \tilde{J} &= \delta_s T_I^{max} \\ \nabla \tilde{g} &= \left| \frac{-1}{A^{\text{ini}}} \right| \delta_s A \,. \end{aligned} \tag{9.3}$$

However, the numerical gradients are determined using the FDM, whereby the following central difference approximations are applied for the objective function $\nabla \tilde{J}_c$ and for the constraint $\nabla \tilde{g}_c$, i.e.

$$\begin{aligned} \nabla \tilde{J}_c &= \frac{\tilde{J}(\tilde{\mathbf{s}}, \boldsymbol{\nu}(\tilde{\mathbf{s}}), \epsilon_c^+) \; - \; \tilde{J}(\tilde{\mathbf{s}}, \boldsymbol{\nu}(\tilde{\mathbf{s}}), \epsilon_c^-)}{2\, \epsilon_c} \\ \nabla \tilde{g}_c &= \frac{\tilde{g}(\tilde{\mathbf{s}}, \boldsymbol{\nu}(\tilde{\mathbf{s}}), \epsilon_c^+) \; - \; \tilde{g}(\tilde{\mathbf{s}}, \boldsymbol{\nu}(\tilde{\mathbf{s}}), \epsilon_c^-)}{2\, \epsilon_c} \,, \end{aligned} \tag{9.4}$$

with the perturbation ϵ_c.

The objective of this subsection is to compare the analytical gradients with the numerical approaches, whereby the relative errors are determined. However, the influence of the selected perturbation value ϵ, which are required to determine the design velocity matrix $\mathbf{v}$, cf. Eq. (6.35), is examined in detail. For this purpose, different values are applied for the perturbation values ϵ and the perturbation values ϵ_c. The calculations are based on the hollow structure, see Sec. 8.2, with the same material and geometry parameters as introduced in Table 8.1. To accelerate the calibration, however, the discretisation in space and time are applied more roughly, i.e. the structure is approximated with eight elements and a time increment of 0.2 d. The results become more accurate with finer discretisation. It is therefore, assumed, that if a coarser approximation leads to verification of the analytical variation, the same statement is also permissible for finer approximation strategies. The assumption for a coarser discretisation is only applied in the context of calibration; the following optimisation in Sec. 9.2.2 is based on the previously introduced fine approximations for time and space. Table 9.2 contains the relative errors between the analytical $\nabla \tilde{J}$ and numerical $\nabla \tilde{J}_c$ approach for the gradients of the objective function, whereby the Euclidean norm is applied.

Table 9.2.: Calculation of the relative error between the analytical derivation $\nabla \tilde{J}$ and the numerical derivation $\nabla \tilde{J}_c$ with respect to different perturbation values ϵ_c for the numerical access of the gradient and with respect to different perturbation values ϵ for the design velocity matrix.

Design velocity perturbation			
$\epsilon = 1 \times 10^{-2}$		$\epsilon = 1 \times 10^{-3}$	
$\frac{\lVert\nabla \tilde{J}_c - \nabla \tilde{J}\rVert}{\lVert\nabla \tilde{J}\rVert}$	ϵ_c	$\frac{\lVert\nabla \tilde{J}_c - \nabla \tilde{J}\rVert}{\lVert\nabla \tilde{J}\rVert}$	ϵ_c
1.8036×10^{-4}	1×10^{-2}	1.9518×10^{-4}	1×10^{-2}
4.8634×10^{-5}	1×10^{-3}	1.8282×10^{-6}	1×10^{-3}
6.6722×10^{-5}	1×10^{-4}	5.6384×10^{-5}	1×10^{-4}
3.9663×10^{-4}	1×10^{-5}	3.8015×10^{-4}	1×10^{-5}
Design velocity perturbation			
$\epsilon = 1 \times 10^{-4}$		$\epsilon = 1 \times 10^{-5}$	
$\frac{\lVert\nabla \tilde{J}_c - \nabla \tilde{J}\rVert}{\lVert\nabla \tilde{J}\rVert}$	ϵ_c	$\frac{\lVert\nabla \tilde{J}_c - \nabla \tilde{J}\rVert}{\lVert\nabla \tilde{J}\rVert}$	ϵ_c
2.2974×10^{-4}	1×10^{-2}	$3.705\,64 \times 10^{-4}$	1×10^{-2}
5.5958×10^{-5}	1×10^{-3}	3.7952×10^{-4}	1×10^{-3}
1.4750×10^{-6}	1×10^{-4}	3.5544×10^{-4}	1×10^{-4}
3.5569×10^{-4}	1×10^{-5}	1.4686×10^{-6}	1×10^{-5}

Table 9.3 presents relative errors between the analytical $\nabla \tilde{g}$ and numerical $\nabla \tilde{g}_c$ approach for the gradients of the constraints. Both tables highlight the rows, resulting in the smallest error. Resulting in a more visible identical application, it becomes apparent that an identical perturbation value for the design velocity matrix ϵ and for the numerical investigation of the gradients ϵ_c lead to the smallest error.

Due to the very small relative errors, it can be stated that the analytically derived variants of the objective function and constraints are implemented correctly. Furthermore, it becomes clear that the numerical approaches depend on the choice of the perturbation factors. An efficient optimisation process can be guaranteed overall with the analytical approaches.

9.2.2. Optimal Solution

The solution of the nonlinear constrained optimisation problem is carried out with the help of a mathematical solver. The function fmincon, available in the MATLAB optimisation toolbox, is used to determine the optimised design parameters with the 'active-set' algorithm. This algorithm is based on the solution method of SQP, cf. Sec. 5.5.1. Providing the defined objective function, the constraint and its analytical derived gradients.

Table 9.3.: Calculation of the relative error between the analytical derivation $\nabla\tilde{g}$ and the numerical derivation $\nabla\tilde{g}_c$ with respect to different perturbation values ϵ_c for the numerical access of the gradient and with respect to different perturbation values ϵ for the design velocity matrix.

Design velocity perturbation			
$\epsilon = 1\times10^{-2}$		$\epsilon = 1\times10^{-3}$	
$\frac{\lVert\nabla\tilde{g}_c - \nabla\tilde{g}\rVert}{\lVert\nabla\tilde{g}\rVert}$	ϵ	$\frac{\lvert\nabla\tilde{g}_c - \nabla\tilde{g}\rVert}{\lVert\nabla\tilde{g}\rVert}$	ϵ
6.7779×10^{-6}	1×10^{-2}	2.6020×10^{-6}	1×10^{-2}
4.4967×10^{-6}	1×10^{-3}	6.8041×10^{-8}	1×10^{-3}
4.3730×10^{-6}	1×10^{-4}	1.7184×10^{-7}	1×10^{-4}
3.5957×10^{-6}	1×10^{-5}	2.6036×10^{-6}	1×10^{-5}
Design velocity perturbation			
$\epsilon = 1\times10^{-4}$		$\epsilon = 1\times10^{-5}$	
$\frac{\lVert\nabla\tilde{g}_c - \nabla\tilde{g}\rVert}{\lVert\nabla\tilde{g}\rVert}$	ϵ	$\frac{\lVert\nabla\tilde{g}_c - \nabla\tilde{g}\rVert}{\lVert\nabla\tilde{g}\rVert}$	ϵ
2.5740×10^{-6}	1×10^{-2}	3.7988×10^{-6}	1×10^{-2}
1.9396×10^{-7}	1×10^{-3}	2.6316×10^{-6}	1×10^{-3}
9.3693×10^{-10}	1×10^{-4}	2.4382×10^{-6}	1×10^{-4}
2.4382×10^{-6}	1×10^{-5}	1.0387×10^{-9}	1×10^{-5}

The diagram in Figure 9.2 shows the iteration course of the mathematical solver, which minimises the objective function. In the last iteration step the maximum first principal stress $T_I^{\max}$ achieves a value of $0.077\,\mathrm{MN\,cm^{-2}}$ in the Gauss point. The solver requires a total of 5 iterations until it calculates a local minimum that satisfies the constraints. The mathematical optimisation is completed due to the solver being able to decrease the objective functions whilst the first-order optimality approaches zero with a value of 7.2233×10^{-9} in the last iteration step, see Figure 9.3. The first-order optimality is a measure, which includes the underlying KKT conditions from Eq. (5.8), and determines how close a point is to optimal. The optimisation leads to the optimal point, the new design parameters, i.e.

$$\tilde{\mathbf{s}} = \begin{bmatrix}0.7 & 0.7676\end{bmatrix}^{\mathrm{T}} . \tag{9.5}$$

The contour plot of the first principal stress in Figure 9.4 shows that the change of the hole parameters leads to an overall decrease in stress. This example illustrates how the shape has a major influence on the stress distribution in the structure. This observation is supported by Figure 9.4, which shows the temporal course of the first principal stress $T_I^{\max}$ in the maximum loaded point A for the new shape, printed with a green line, and the initial shape, printed with a black line. Due to the shape optimisation, the overall stress can be reduced. The influence of degradation can also be slightly reduced, as shown in Figure 9.5. However, with a value of $J_d = 0.9563$ in the new design and $J_d = 0.9561$

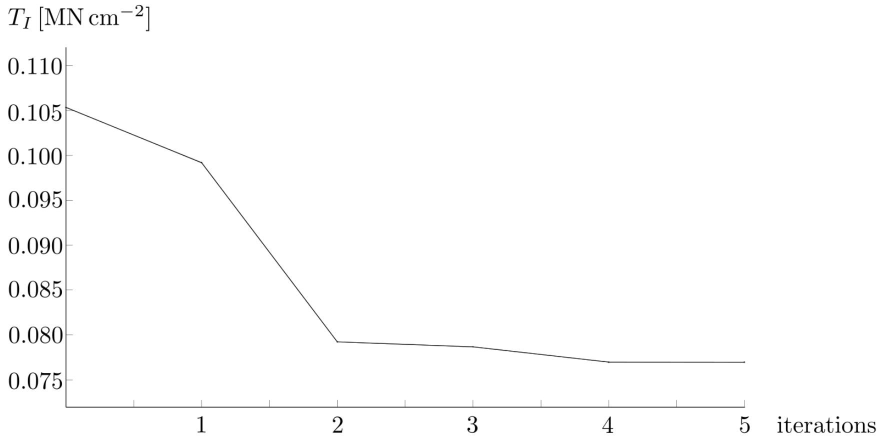

Figure 9.2.: Iteration of the optimisation solver, which records the decrease of the objective function, i.e. the first principal stress T_I. In the last iteration step, a minimised first principal stress of 0.077 MN cm^{-2} is present.

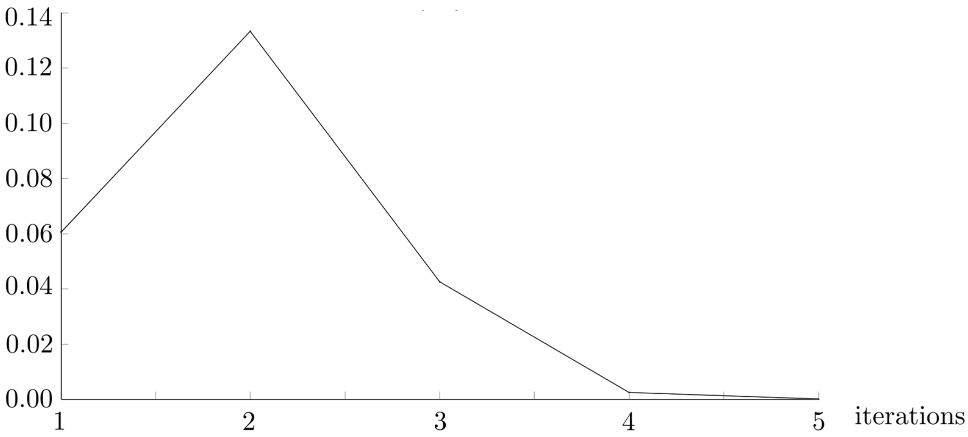

Figure 9.3.: Iteration of the optimisation solver, which records the decrease of the first-order optimality measure. In the last iteration step, a first-order optimality of 7.2233×10^{-9} is present.

in the initial design after the last time step, the difference is minimal. To further reduce the material degradation, the material parameters must be optimised. Nevertheless, this example shows a strong coupling between the chemical concentrations and the mechanical stresses.

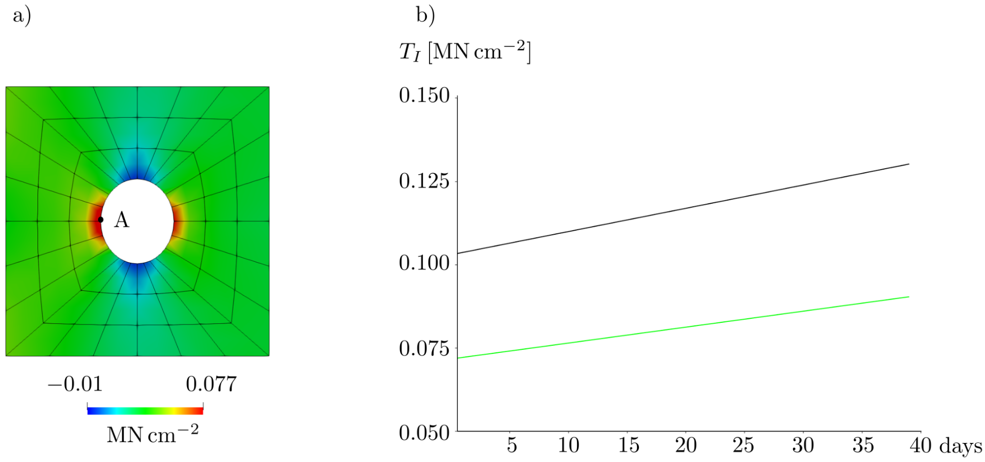

Figure 9.4.: a) Contour plot of first principal stress T_I in the last time step with the new design. b) Evaluation of the first principal stress $T_I^{\max}$ in point A over time with green line referred to the new design and black line referred to the initial design.

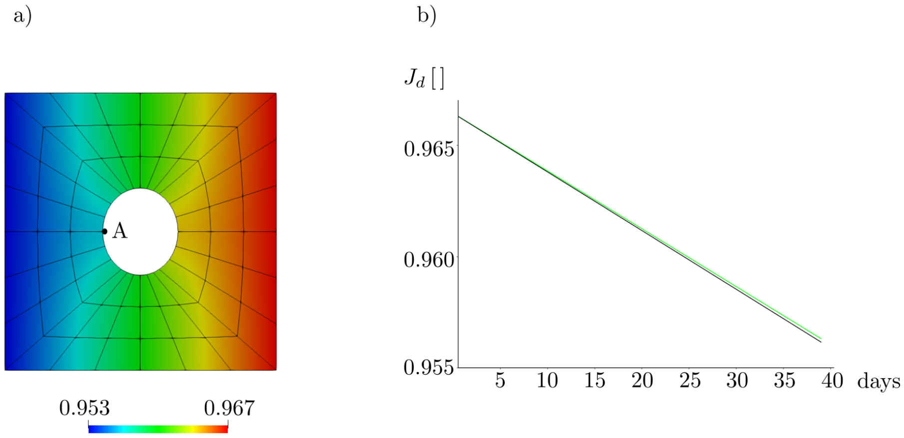

Figure 9.5.: a) Contour plot of degradation J_d in the last time step with the new design. b) Evaluation degradation J_d in point A over time with green line referred to the new design and black line referred to the initial design.

9.2.3. Optimal Solution Algorithm

The mathematical optimisation is solved utilising the MATLAB function fmincon, which calculates the minimum of a constrained nonlinear multi-variable function. The MATLAB user can choose between different algorithms to solve the problem whereby the mathematical background of the solvers may differ and influence the optimisation result. For this reason, the influence of the solution algorithm on the optimised result is investigated more closely in this subsection. In detail, the algorithm 'sqp-legacy', 'active-set' and 'interior-point' are applied to solve the introduced optimisation task, cf. Eq. (9.1). The algorithms 'sqp-legacy' and 'active-set' are based on the SQP method presented in this thesis. SQP is developed using Newton's method whilst taking inequality constraints into account. Nevertheless, the two algorithms differ in their implementation, e.g. they use alternative definitions for strict feasibility regarding bounds or the choice of solution algorithm for the sub-problems. In contrast, the 'interior-point' algorithm first converts the inequality-constrained problem into an equality constrained problem. It then solves it with Newton steps or conjugate gradient steps depending on the solution of each iteration step. For more information, see [92]. The solutions are identical for all approaches, i.e. the efficiency can be assessed based on the number of iterations and calculation time. Table 9.4 compares the efficiency of the algorithms on this basis and demonstrates how the algorithm, 'active-set', runs most efficiently, as the solution is obtained after five iterations, respectively after 7525 s.

Table 9.4.: Comparison of different solution algorithms.

Algorithm	**Number of iterations**	**Time in seconds**	**Optimisation result**	**First-order optimality measure**
'sqp-legacy'	5	9205	[0.7; 0.7676]	3.06×10^{-7}
'active-set'	5	7525	[0.7; 0.7676]	7.22×10^{-9}
'interior-point'	31	221412	[0.7; 0.7676]	2.62×10^{-6}

9.2.4. Efficiency of the Variational Approach

As mentioned above, the required gradients of the objective function and constraints can be determined numerically with FDM as well as analytically. Thus, the analytical solution of the previously described optimisation problem is compared with the solution using FDM, whereby the most efficient 'active-set' algorithm is utilised. Applying the central FDM with a perturbation factor of $\epsilon_c = 1 \times 10^{-4}$ leads to the identical iteration process and design parameters. However, there is a big difference in the amount of computational time required, the analytically predefined gradients take 7525 s and the numerical derived gradients take 37 673 s. The time efficiency is due to the variational method and the analytical gradients are determined simultaneously within the FEM calculation. Where the numerical method approximates the gradients by repeating calculation loops with altered design parameters. Due to this time efficiency, the added value of the presented variation approach becomes apparent.

9.3. Optimisation of a Bridge-like Structure

The example is inspired by a bridge with mechanical loading under environmental conditions, such as calcium leaching. Calcium leaching can occur under long-term exposure to pure water, with calcium ions being released due to concentration differences. The equalisation of concentrations takes place via the diffusion of the particles. In this example, a description is provided of a concentration's general diffusion process, which as discussed, consequentially leads to material degradation. Figure 9.6a displays the applied boundary value problem. The symmetry of the structure is exploited to save computing time. The calculation is therefore, performed on half of the system with symmetry boundary conditions on the right side.

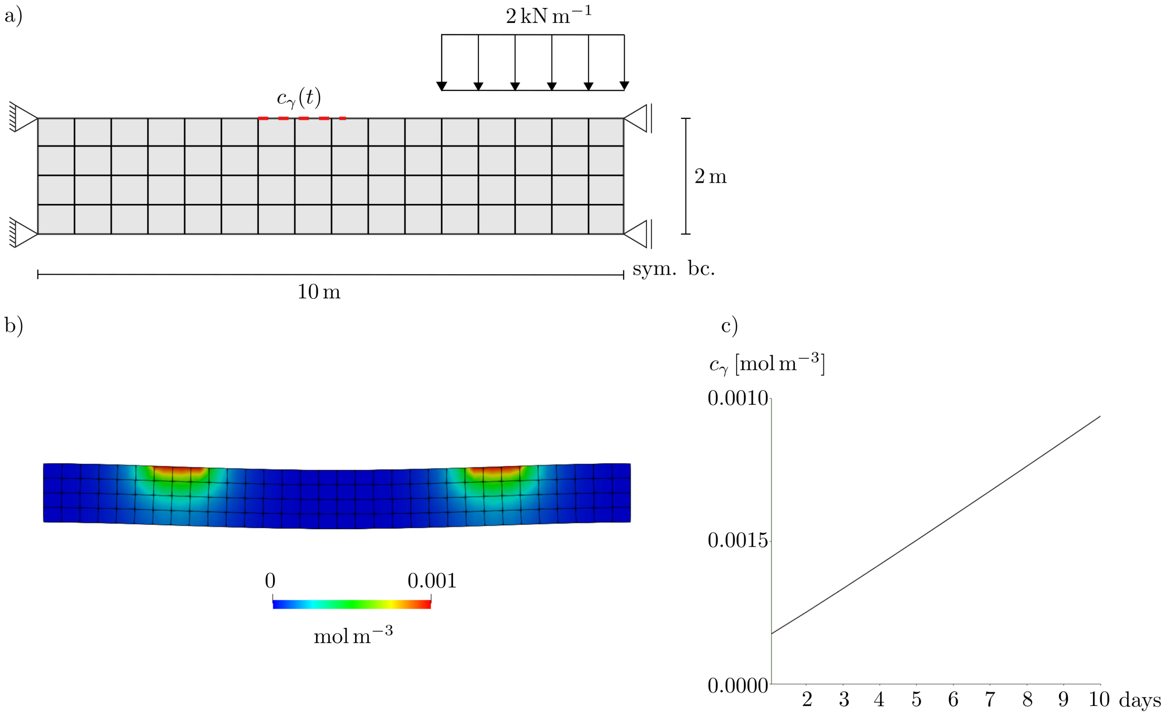

Figure 9.6.: a) Mechanical and chemical boundary conditions and mesh of a bridge-like structure. b) Contour plot of the concentrations in the last time step. c) Illustration of the concentrations $c_\gamma(\mathrm{t})$ over 10 d with a linear increase in the applied Dirichlet boundary conditions.

The bridge is loaded by a line load with 2 kN m^{-1} and a concentration, which increases during the simulation time up to 0.001 mol m^{-3}, as shown in Figures 9.6b and 9.6c.

Table 9.5.: Material and geometry parameters.

$E = 3000\,\mathrm{kN\,m^{-2}}$

$\nu = 0.2$

$\rho_0^* = 1000\,\mathrm{kg\,m^{-3}}$

$M_\gamma = 10\,000\,\mathrm{kg\,mol^{-1}}$

$D = 0.1\,\mathrm{m^2\,d^{-1}}$

$c_\gamma^0 = 0.0001\,\mathrm{mol\,m^{-3}}$

The boundary value problem is discretised with 64 elements and with a time increment of 0.02 d, whereby a total of 10 d is simulated. Table 9.5 presents the applied material and geometry parameters. The objective of this example is to investigate how the long-term effect of concentrations can influence the optimisation of a mechanically loaded structure. Of particular interest is the evaluation of the optimisation result during different times of the simulation. The task specifies the area A of a bridge-like structure as the objective function $\tilde{J}(\tilde{\mathbf{s}}, \boldsymbol{\nu}(\tilde{\mathbf{s}}))$, so that the material costs can be reduced. Hereby, Eq. (6.46) is applied for a plane strain setting. Furthermore, the constraint is defined by a column matrix $\tilde{\mathbf{g}}(\tilde{\mathbf{s}}, \boldsymbol{\nu}(\tilde{\mathbf{s}}))$, which contains a restriction to a maximum first principal stress in all Gauss points. Thus, the optimisation problem is defined as follows

$$\begin{aligned} \tilde{J}(\tilde{\mathbf{s}}, \boldsymbol{\nu}(\tilde{\mathbf{s}})) &= A \\ \tilde{\mathbf{g}}(\tilde{\mathbf{s}}, \boldsymbol{\nu}(\tilde{\mathbf{s}})) &= \mathbf{T}_I - \bar{T}_I\,\mathbf{1}\,, \end{aligned} \tag{9.6}$$

with a column matrix containing the solution of the first principal stresses in the Gauss points $\mathbf{T}_I \in \mathbb{R}^{576}$, a all-ones column matrix $\mathbf{1} \in \mathbb{R}^{576}$ and the defined threshold $\bar{T}_I$. Respectively, the total optimisation problem follows with, i.e.

$$\begin{aligned} &\min \tilde{J}(\tilde{\mathbf{s}}, \boldsymbol{\nu}(\tilde{\mathbf{s}})) \;:\; && \tilde{\mathbf{g}} \le \mathbf{0} && \text{inequality constraint} \\ &\tilde{\mathbf{s}} \in \mathbb{R} && \tilde{\mathbf{s}}^l \le \tilde{\mathbf{s}} \le \tilde{\mathbf{s}}^u && \text{limit values}\,, \end{aligned} \tag{9.7}$$

whereby the design parameters are defined with

$$\tilde{\mathbf{s}} = \begin{bmatrix} x_1 & x_2 & x_3 & x_4 \end{bmatrix}^{\mathrm{T}}, \quad \tilde{\mathbf{s}}^u = \begin{bmatrix} x_1^u & x_2^u & x_3^u & x_4^u \end{bmatrix}^{\mathrm{T}}, \quad \tilde{\mathbf{s}}^l = \begin{bmatrix} x_1^l & x_2^l & x_3^l & x_4^l \end{bmatrix}^{\mathrm{T}}. \tag{9.8}$$

The design parameters are the control points of a B-spline function: they describe the lower edge of the structure as outlined in Figure 9.7 allowing for vertical displacement.

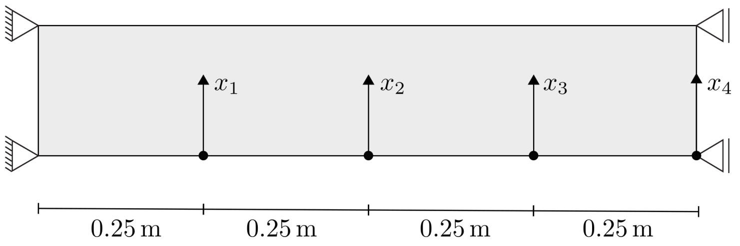

Figure 9.7.: Design parameters for the structural optimisation.

Accordingly, the two-column matrices $\tilde{\mathbf{s}}^u$ and $\tilde{\mathbf{s}}^l$ contain the upper and lower values of the design parameters. Due to the assumed symmetry, the design parameters must fulfil the requirement that a horizontal geometry is maintained at the lower right support. Therefore, the condition $x_3 = x_4$ is introduced. The parameters for the optimisation algorithm are shown in Table 9.6. The nonlinear constrained optimisation problem is evaluated at three simulation times, the optimisation is carried out after 1 d, 5 d and 10 d. As a result, the influence of the time-dependent chemical concentration becomes visible. Here again, the MATLAB fmincon function is utilised to solve the mathematical optimisation and the gradients for the objective function and the constraints are provided. The analytical derived objective function $\nabla \tilde{J}$ is obtained with Eq. (6.47) and the analytical constraint $\nabla \tilde{g}$ is calculated under consideration of Eq. (6.42), whereby the gradient of the area and of the first principal stress are derived, i.e.

Table 9.6.: Input parameters for the optimisation algorithm.

threshold	$\bar{T}_I$	60	$\mathrm{kN\,m^{-2}}$
limit values	$\tilde{\mathbf{s}}^u$	$[1.0;\ 1.0; 1.0; 1.0]$	m
	$\tilde{\mathbf{s}}^l$	$[-1.0;\ -1.0; -1.0; -1.0]$	
initial design	$\tilde{\mathbf{s}}$	$[0;\ 0; 0; 0]$	m

$$\begin{aligned} \nabla \tilde{J} &= \delta_s A \\ \nabla \tilde{g} &= \delta_s \mathbf{T}_I \,. \end{aligned} \tag{9.9}$$

Figure 9.8 shows the iteration course of the objective function, the area of the structure, during the optimisation. Here, the optimisation for the three different simulation times are printed, i.e. the red line demonstrates the iteration for structural optimisation after 1 d, the second, blue represents 5 d and finally the green line shows the iteration after 10 d. For all three examples, the optimisation solver stopped after six iterations because the predicted change in the objective function is less than a tolerance of 1×10^{-6}. However, the curves converge to different values: it becomes clear that with longer environmental influence the area can only be reduced to a lesser extent in order to fulfil the constraints, i.e. the solution converges for a simulation time including 1 d to area of $14.70\,\mathrm{m}^2$, 5 d to an area of $15.05\,\mathrm{m}^2$ and 15 d to a area of $15.78\,\mathrm{m}^2$. The corresponding design parameters follow with

$$\begin{aligned} &1\,\text{day} &&: \quad \tilde{\mathbf{s}} = \left[9.85 \times 10^{-1} \quad 1.00; \quad 1.18 \times 10^{-1} \quad 1.18 \times 10^{-1}\right]^{\mathrm{T}} \\ &5\,\text{days} &&: \quad \tilde{\mathbf{s}} = \left[9.01 \times 10^{-1} \quad 1.00 \quad 7.85 \times 10^{-2} \quad 7.85 \times 10^{-2}\right]^{\mathrm{T}} \\ &10\,\text{days} &&: \quad \tilde{\mathbf{s}} = \left[7.50 \times 10^{-1} \quad 1.00 \quad -1.95 \times 10^{-2} \quad -1.95 \times 10^{-2}\right]^{\mathrm{T}} , \end{aligned} \tag{9.10}$$

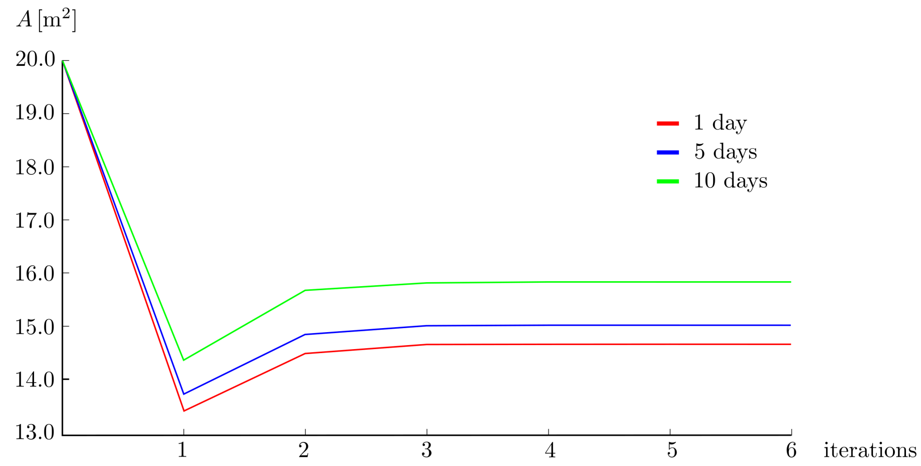

Figure 9.8.: Iteration of the optimisation solver, which records the decrease of the objective function, i.e. the area A. The red line refers to the simulations time after 1 d, the blue line after 5 d and the green line after 10 d.

and they are printed in Figure 9.9. The design parameters show that the greatest saving occurs in the area of the least stress, where neither compressive nor tensile stresses are present. As well as this, it is also noted that more material is needed in the centre of the beam to ensure load-bearing capacity. The calculation times for the mathematical optimisation are 285 s, 1365 s and 2731 s for the optimisation including 1 d, 5 d and 10 d. The contour plot in Figure 9.10 represents the first principal stress in the optimised and initial design, whereby the optimisation design taking into account 10 d is referred. With this example, the material is saved, yet a defined load capacity can still be guaranteed.

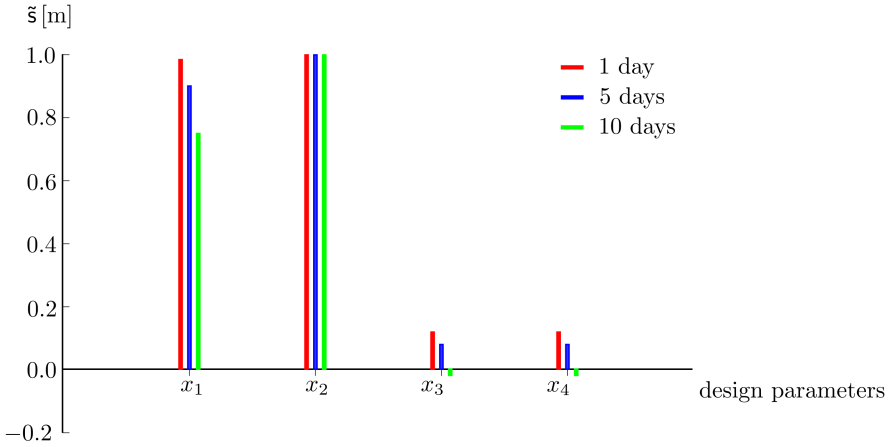

Figure 9.9.: Solution for the design parameters $\tilde{\mathbf{s}} = [x_1;\, x_2;\, x_3;\, x_4]$. The red line refers to the simulations time after 1 d, the blue line after 5 d and the green line after 10 d.

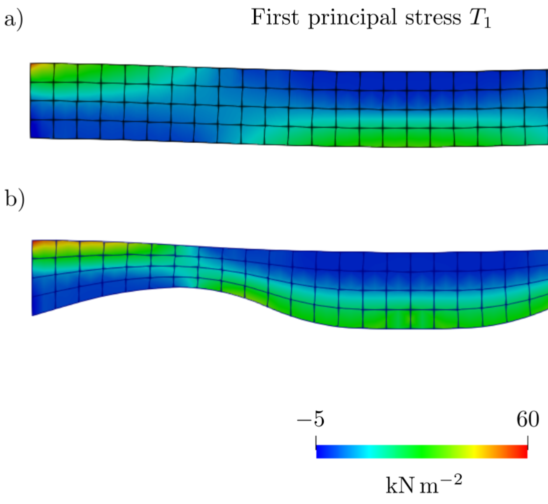

Figure 9.10.: Evaluation of the first principal stress in the Gauss points induced by mechanical load. a) Initial structure with $T_1^{\max} = 55.9\,\mathrm{kN\,m^{-2}}$ vs. b) optimal structure with $T_1^{\max} = 60\,\mathrm{kN\,m^{-2}}$.

Even the slightest penetration of chemical concentrations influences the stresses in the structure and thus, also the optimisation results. Without taking environmental influences into account, no reliable calculation of efficient shapes can be guaranteed. In particular, the simulation time and the exposure time must be taken into account. Figure 9.11 shows the development of the maximum first principal stress in the bridge over time. The curves refer to the evaluation using the initial design with a black line. In the evaluation, the three optimal solutions are marked by different colours depending on the simulation times taken into account; red refers to 1 d, blue to 5 d and green to 10 d. The desired load-bearing capacity of $T_1^{\max} = 60\,\mathrm{kN\,m^{-2}}$ can only be fulfilled by the optimal design evaluated with a simulation time of 10 d.

9.4. Concluding Remarks on the Shape Optimisation Examples

In this section, two examples of the application of the developed model of structural shape optimisation of diffusion-driven degradation processes are presented. The aim of these optimisation tasks is to improve the shape of the structures, yet not exceed the maximum possible stresses and ensure load-bearing capacity.

The first example is used for a closer analysis of the optimisation procedure. The optimisation criterion is explained in more detail and the different solution algorithms are compared. Furthermore, the efficiency of the analytically provided gradients is highlighted

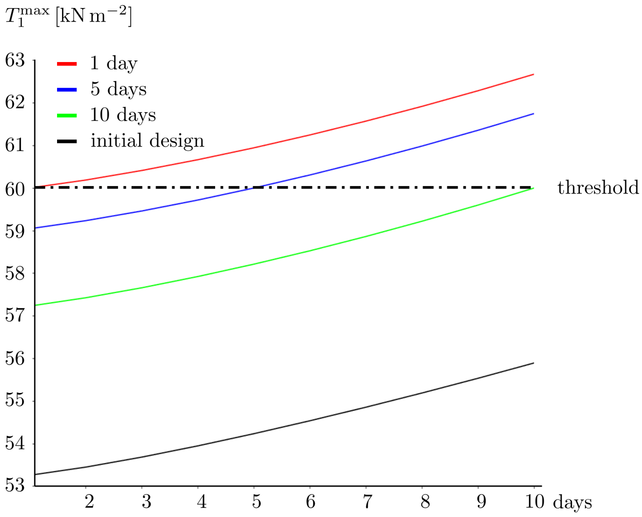

Figure 9.11.: Evaluation of the maximum first principal stress $T_1^{\max}$ over time induced by mechanical loads. The black line represents the maximum first principal stress evaluated with the initial design; the red, blue and green lines refer to the maximum first principal stress in the optimised design considering 1 d, 5 d and 10 d calculation time.

and compared with the numerical approach. A clear acceleration of the calculation time using the analytical approach becomes apparent.

In the second example, the practical reference focuses on simulating a bridge-like structure under harmful environmental influences. In particular, the influence of chemical concentrations is highlighted, whereby exposure time plays an essential role. It can be shown that influences from the environment, such as diffusion processes, must be taken into account; otherwise, the load-bearing capacity may be exceeded.

10. Examples of Material Parameter Optimisation

In the following sections, examples of the material parameter optimisation with the continuum mechanical-chemical-degradation model follow. The nonlinear least squares curve-fitting is applied to optimise material parameters and reduce material degradation.

10.1. Introduction to Examples of Material Parameter Optimisation

The previously presented shape optimisation enables efficient forms while taking mechanical requirements, such as stress restrictions, into account. However, the impact of the chemical substances cannot be prevented completely. For this reason, material parameter optimisation is implemented. The goal is to identify and adjust the parameters that lead to material degradation. In this section, first an example is given to illustrate the influence of the material parameters. The objective is to reduce material degradation caused by chemical concentrations. Moreover, the introduced example of a bridge-like structure is investigated in regards to optimised material parameters. The example shows how particularly high-risk areas can be protected from the attack of chemical concentrations.

10.2. Material Fitting

The nonlinear curve-fitting problem is demonstrated with the following example. This boundary value problem leads to a nonlinear concentration inflow $c_\gamma(\mathrm{t})$ on the left corner of the structure. The chemicals result in material degradation and thus, to an increase of displacement. The Dirichlet boundary conditions for the displacements and the applied concentrations as well as a contour plot of the concentration in the last time step, after 5 d, are shown in Figure 10.1. Table 10.1 provides the initial material parameters.

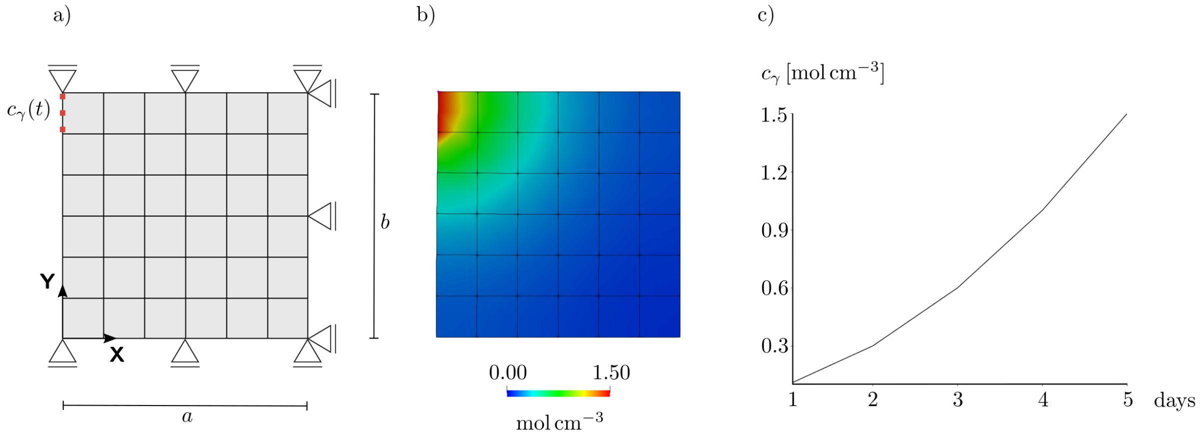

Figure 10.1.: a) Dirichlet boundary conditions and mesh. b) Contour plot of the concentrations in the last time step. c) Illustration of the concentrations over 5 d with a quadratic function of $c_\gamma(\mathrm{t}) = 0.05\,\mathrm{t}^2 + 0.05\,\mathrm{t}$ in the applied Dirichlet boundary conditions.

Table 10.1.: Initial material and geometry parameters for the boundary value problem.

$\mu = 0.833\,\mathrm{MN\,cm^{-2}}$
$\lambda = 0.556\,\mathrm{MN\,cm^{-2}}$
$\rho_0^* = 200\,\mathrm{kg\,cm^{-3}}$
$M_\gamma = 10\,\mathrm{kg\,mol^{-1}}$
$D = 0.1\,\mathrm{cm^2\,d^{-1}}$
$c_\gamma^0 = 0\,\mathrm{mol\,cm^{-3}}$
$a = 1\,\mathrm{cm}$
$b = 1\,\mathrm{cm}$

For the optimisation settings, defined displacements are the objective function, i.e. the objective function consists of a column matrix $\mathbf{u}^{max} \in \mathbb{R}^{13\times 1}$ containing the maximal x-displacements in the nodes on the left side of the structure, so that

$$\tilde{\mathbf{J}}(\mathbf{m}, \boldsymbol{\nu}(\mathbf{m})) = \mathbf{u}^{max} \,. \tag{10.1}$$

Furthermore, the material parameters represent the alterable design and the nonlinear least-square problem follows with

$$\min_{\mathbf{m} \in \mathbb{R}^{\mathrm{dofs}},\ \boldsymbol{\nu} \in \mathbb{R}^{\mathrm{dof}}} ||\tilde{\mathbf{J}}(\mathbf{m}, \boldsymbol{\nu}(\mathbf{m}))||_2^2 \quad : \quad \mathbf{m}^l \leq \mathbf{m} \leq \mathbf{m}^u \quad \text{limit values} \,. \tag{10.2}$$

In the application example, the parameter set $\mathbf{m}$ is fitted to minimise the deformation due to material degradation, wherein lower $\mathbf{m}^l$ and upper $\mathbf{m}^u$ material parameters are defined with

$$\mathbf{m} = \begin{bmatrix} \mu \\ \lambda \\ \rho_0^* \\ M_\gamma \\ D \end{bmatrix} \qquad \mathbf{m}^l = \begin{bmatrix} 0.733\,\mathrm{MN\,cm^{-2}} \\ 0.456\,\mathrm{MN\,cm^{-2}} \\ 100\,\mathrm{kg\,cm^{-3}} \\ 5\,\mathrm{kg\,mol^{-1}} \\ 0.05\,\mathrm{cm^2\,d^{-1}} \end{bmatrix} \qquad \mathbf{m}^u = \begin{bmatrix} 1.333\,\mathrm{MN\,cm^{-2}} \\ 0.856\,\mathrm{MN\,cm^{-2}} \\ 300\,\mathrm{kg\,cm^{-3}} \\ 15\,\mathrm{kg\,mol^{-1}} \\ 0.15\,\mathrm{cm^2\,d^{-1}} \end{bmatrix}. \tag{10.3}$$

The parameters are composed of the mechanical Lamé parameters μ and λ, the initial density ρ_0^*, the molar mass M_γ and the diffusion parameter D. The mathematical optimisation is performed with the MATLAB function lsqnonlin and the required gradient for the objective function is provided analytically, cf. Eq. (6.33). Figure 10.2 displays the iteration of the norm of residuals, wherein the residuals are the values of the objective function at the solution, thus the x-displacements on the left side of the structure. It becomes clear that the maximum displacement on the left side of the structure approaches zero. Within 355 s and six iterations, the algorithm leads to the optimised material parameters set, see Table 10.2. The material degradation triggers the maximum displacement at the upper entry point of the concentration. With the help of material optimisation, the parameters are adjusted and the displacement and material degradation are significantly reduced. The influence of the optimised parameters on the displacement is shown in Figure 10.3. The comparison of the evaluation using the

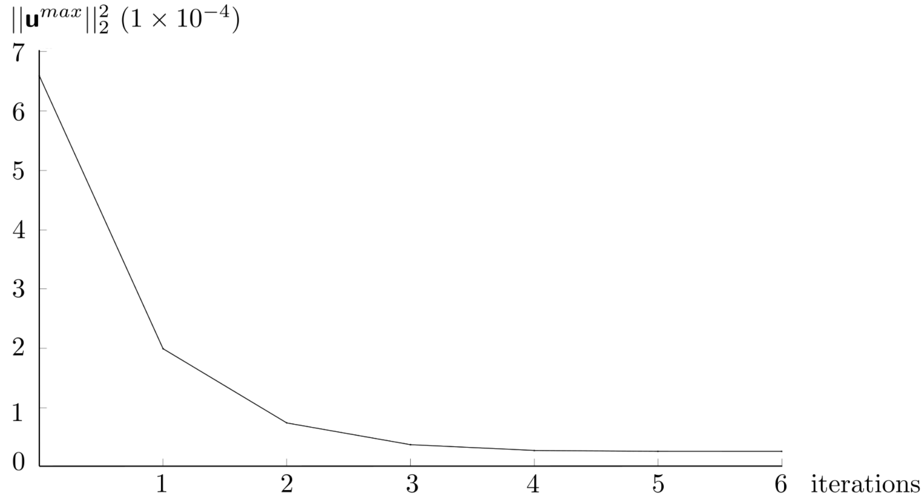

Figure 10.2.: Iteration of the optimisation solver, which records the decrease of the norm of residuals, i.e. the norm of the maximal x-displacements with a minimum value of $2.662\,48 \times 10^{-5}$.

Table 10.2.: Initial material parameters on the left vs. fitted material parameters on the right.

m	Initial material parameters	Fitted material parameters
μ	$0.833\,\mathrm{MN\,cm^{-2}}$	$1.333\,\mathrm{MN\,cm^{-2}}$
λ	$0.556\,\mathrm{MN\,cm^{-2}}$	$0.456\,\mathrm{MN\,cm^{-2}}$
ρ_0^*	$200\,\mathrm{kg\,cm^{-3}}$	$300\,\mathrm{kg\,cm^{-3}}$
M_γ	$10\,\mathrm{kg\,mol^{-1}}$	$5\,\mathrm{kg\,mol^{-1}}$
D	$0.1\,\mathrm{cm^2\,d^{-1}}$	$5\times10^{-2}\,\mathrm{cm^2\,d^{-1}}$

initial material parameters (black line) vs. the optimised material parameters (green line) is shown. The example shows that the nonlinear curve-fitting problem can be used to prevent the negative effects of chemical concentrations and the resulting material degradation.

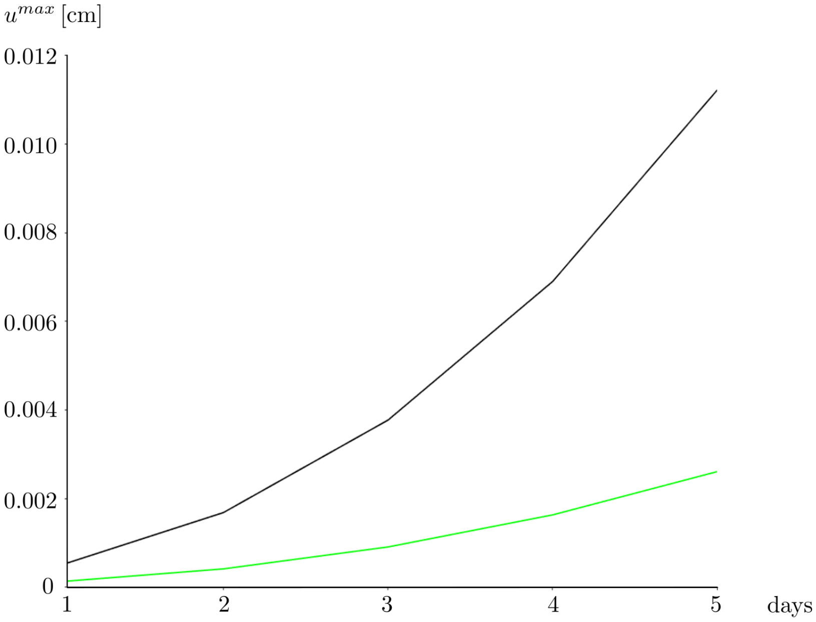

Figure 10.3.: Evaluation of the maximal displacement $u^{\max}$ over time with green line referred to the new material parameters and black line referred to the initial material parameters.

10.3. Material Fitting for a Bridge-like Structure

In this example, the influence of different material parameters on the directional and time-dependent diffusion of the concentrations is investigated. The suggestion is to protect, for example, a bridge from environmentally induced damage mechanisms. In practice, the penetration of harmful and diffusive carbon dioxide or chemical concentrations is reduced by using coatings. This can prevent the chemicals from reaching and attacking the reinforcements.

The boundary value problem is introduced in Figure 10.4a, whereby the same dimensions, as well as the time increment and spatial discretisation, are applied as outlined in Sec. 9.3. In Figure 10.4b is the applied Dirichlet boundary condition of the concentration depicted over time. The simulation runs over 10 d with a quadratic increase of the concentrations up to a value of 0.0056 mol m^{-3}. The bridge-like structure is intended to be attacked with concentrations on the underside as shown in Figure 10.4a. The objective is to reduce the diffusion of the concentrations so that the more damageable surface is protected. For this purpose, the material parameters in the lower part of the structure are to be optimised (material 1). Thus, the structure is divided into two sections with different sets of material parameters, as printed in Figure 10.5. In order to reduce the application of a more cost-intensive permeability-reducing material, the use is optimised and the still permissible amount of chemical concentrations that reach the surface is exhausted. The initial material and geometry parameters for the boundary value problem refer to Table 9.5. The optimisation follows with

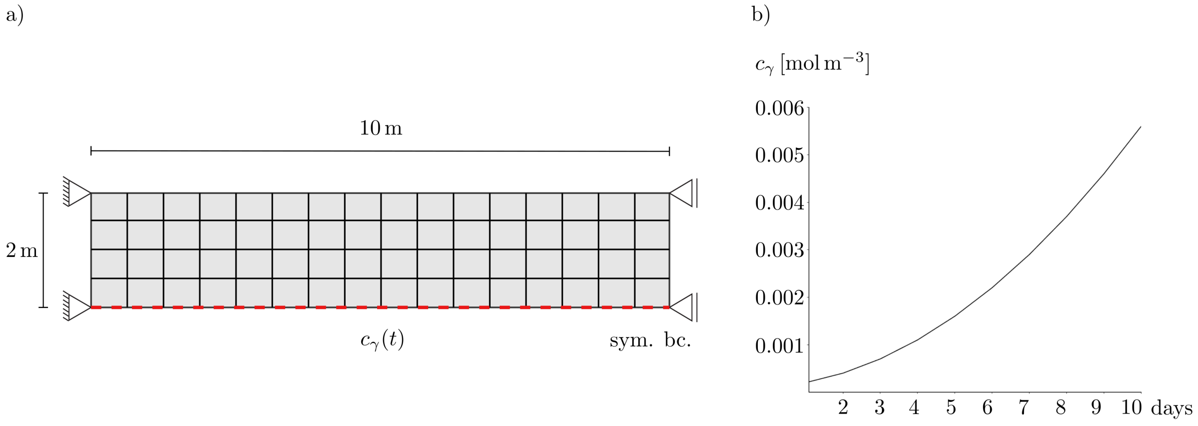

Figure 10.4.: a) Dirichlet boundary conditions and mesh of a bridge-like structure. b) Illustration of the concentrations over 10 d with a quadratic function of $c_\gamma(\mathrm{t}) = 5 \times 10^{-5}\,\mathrm{t}^2 + 5 \times 10^{-5}\,\mathrm{t}$ in the applied Dirichlet boundary conditions.

$$\tilde{\mathbf{J}}(\mathbf{m}, \boldsymbol{\nu}(\mathbf{m})) = (\mathbf{c}_\gamma - \bar{c}_\gamma\,\mathbf{1})\,, \tag{10.4}$$

wherein $\mathbf{c}_\gamma$ refers to the concentrations reaching the surface of the structure ($\mathrm{Y} = 2$), see the blue line in Figure 10.5, and a all-ones column matrix $\mathbf{1} \in \mathbb{R}^{33\times 1}$ connects to a defined

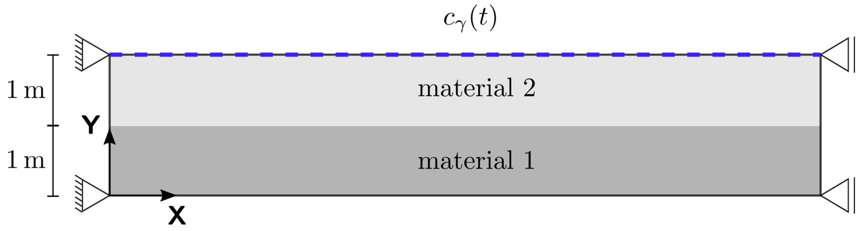

Figure 10.5.: Division of the bridge into two sections with different sets of material parameters to assess the concentrations $c_\gamma(t)$ arriving at the surface of the structure.

threshold of $\bar{c}_\gamma = 0.0003\,\mathrm{mol\,m^{-3}}$. The nonlinear least-square problem results in

$$\begin{aligned} &\min ||\tilde{\mathbf{J}}(\mathbf{m}, \boldsymbol{\nu}(\mathbf{m}))||_2^2 \quad : \quad \mathbf{m}^l \ \leq \ \mathbf{m} \leq \mathbf{m}^u \quad \text{limit values}\,, \\ &\mathbf{m} \in \mathbb{R}^{\text{dofs}},\ \boldsymbol{\nu} \in \mathbb{R}^{\text{dof}} \end{aligned} \tag{10.5}$$

whereby the parameters for material 1 are restricted to the lower $\mathbf{m}^l$ and upper $\mathbf{m}^u$ set with

$$\mathbf{m} = \begin{bmatrix} \mu \\ \lambda \\ \rho_0^* \\ M_\gamma \\ D \end{bmatrix} \qquad \mathbf{m}^l = \begin{bmatrix} 662.79\,\mathrm{kN\,m^{-2}} \\ 1105.75\,\mathrm{kN\,m^{-2}} \\ 500\,\mathrm{kg\,m^{-3}} \\ 5000\,\mathrm{kg\,mol^{-1}} \\ 0\,\mathrm{m^2\,d^{-1}} \end{bmatrix} \qquad \mathbf{m}^u = \begin{bmatrix} 1662.79\,\mathrm{kN\,m^{-2}} \\ 2105.75\,\mathrm{kN\,m^{-2}} \\ 1500\,\mathrm{kg\,m^{-3}} \\ 15\,000\,\mathrm{kg\,mol^{-1}} \\ 0.3\,\mathrm{m^2\,d^{-1}} \end{bmatrix}. \tag{10.6}$$

The iteration of the optimisation solver is shown in Figure 10.6, using the MATLAB function lsqnonlin with the analytically derived gradient for the objective function. The norm of the residuals refers to the concentrations on the top of the bridge-like structure and the iteration shows the fitting process for the concentrations to converge to the defined values. Thereby the norm converges to a value of $2.077\,85 \times 10^{-12}$. The fitted material parameters resulting from the optimisation process are compared with the initial parameters in Table 10.3. Figure 10.7 illustrates the influence of the diffusion parameter on the structure, demonstrating the increase in concentration over time at the surface.

Table 10.3.: Initial material parameters on the left vs. fitted material parameters on the right.

m	**Initial material parameters**	**Fitted material parameters**
μ	$1162.79\,\mathrm{kN\,m^{-2}}$	$1290.53\,\mathrm{kN\,m^{-2}}$
λ	$1605.75\,\mathrm{kN\,m^{-2}}$	$1455.76\,\mathrm{kN\,m^{-2}}$
ρ_0^*	$1000\,\mathrm{kg\,m^{-3}}$	$1138.55\,\mathrm{kg\,m^{-3}}$
M_γ	$10\,000\,\mathrm{kg\,mol^{-1}}$	$8614.51\,\mathrm{kg\,mol^{-1}}$
D	$0.1\,\mathrm{m^2\,d^{-1}}$	$0.068\,42\,\mathrm{m^2\,d^{-1}}$

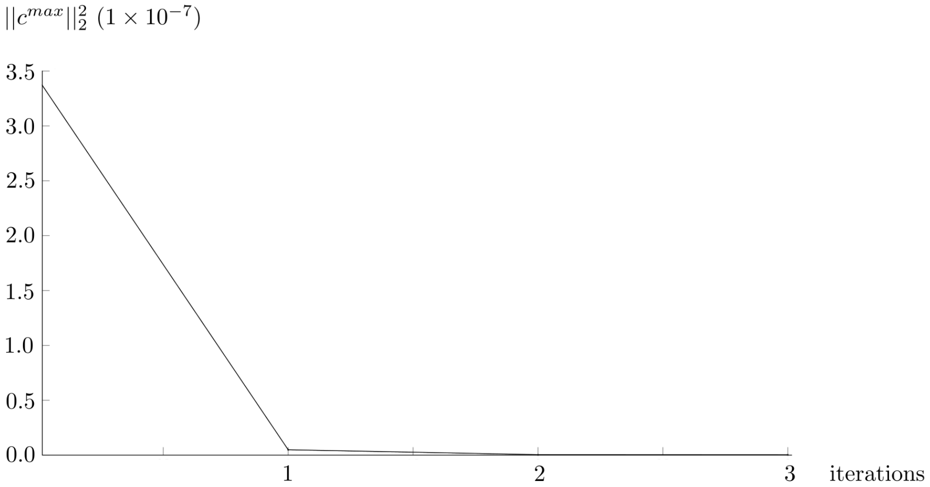

Figure 10.6.: Iteration of the optimisation solver, which records the decrease of the norm of residuals, i.e. the norm of the maximal concentrations on the surface, which converges to a minimum value of $2.077\,85 \times 10^{-12}$.

The evaluation is investigated for different diffusion parameters, especially using the optimised and initial parameter. This shows that a high diffusion parameter leads to a fast flow of the concentrations. Taking into account the optimised parameter, the required threshold $0.0003\,\mathrm{mol\,m^{-3}}$ can be fulfilled. This optimisation process ensures that even long-term effects of chemical substances can be controlled and predicted to prevent destructive effects on the building structure.

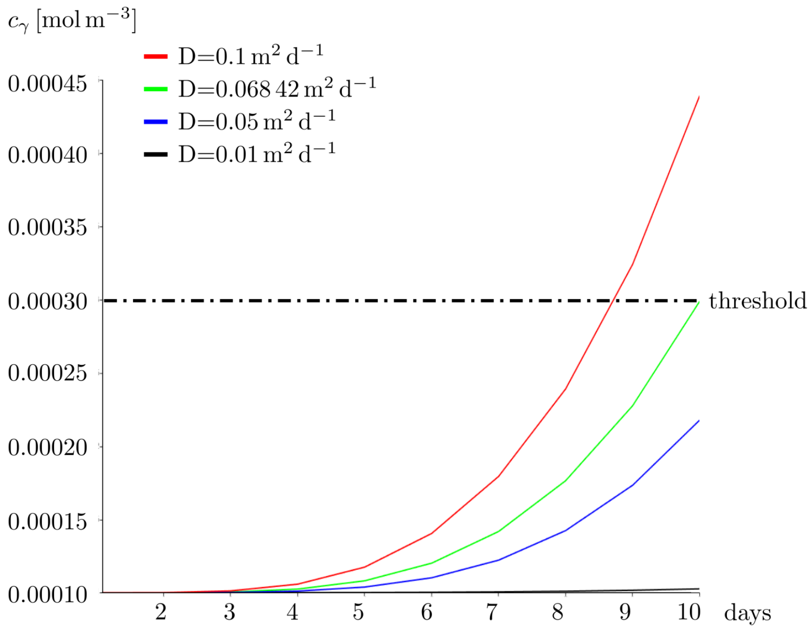

Figure 10.7.: Evaluation of the concentration c_γ on the surface of the bridge over time evaluated for different diffusion parameters.

10.4. Concluding Remarks on the Material Parameter Optimisation

Material optimisation is presented using two examples. In both, the fitting of material parameters is applied to reduce the harmful effect of chemical concentrations in a mechanical structure. Thus, the displacement resulting from chemically induced degradation processes can be reduced, or the distribution of concentrations can be controlled. For instance, more sensitive areas of structures can be protected from chemical attacks.

11. Conclusion and Outlook

In this section, the objectives of this work are briefly summarised and an outlook for future work is presented.

11.1. Conclusion

This thesis achieves the goal of implementing a simulation model that enables

„Structural Optimisation of Diffusion-Driven Degradation Processes“.

Providing a numerical model that can perform an efficient structural optimisation of chemically controlled degradation processes of a mechanical structure. Firstly, the thesis has proven that shape can be optimised by taking into account long-term chemical concentrations as well as maintaining load-bearing capacity. Further to this, the optimisation of material parameters can control the diffusion of concentrations and the associated degradation process. In this way, particularly exposed areas of structures can be preserved.

The sub-objectives include the development of the *structural analysis of the mechanical-chemical-degradation model* and *structural optimisation of the mechanical-chemical-degradation model* as well as the merging of both topics with the presentation of *examples*.

A complete derivation of the structural analysis of a mechanical-chemical-degradation for a permeable structure is provided. Based on solid mechanics, a continuum is proposed in Sec. 3 which allows the coupling of mechanical-chemical and degradation processes. The mechanical degradation process is realised with a combined kinematic and constitutive approach. For this, an extended kinematic formulation for the description of degradation is introduced, using a multiplicative decomposition of the deformation gradient, as shown in Figure 3.1. A consistent thermodynamic evaluation provides the necessary material equations for the sink term of mass exchange, the flux of the chemical concentrations and the mechanical stresses. Sec. 4 contains a detailed representation of the numerical implementation. In conclusion, the required variations of the continuum mechanical quantities are outlined and the discretisation in space and time is introduced. Thus, all necessary equations for the nonlinear numerical implementation are provided.

The achievement of the second sub-objectives is provided along with a general introduction to structural optimisation in Sec. 5. Therein, the mathematical basics for structural shape and material parameter optimisation are given with the evaluation of nonlinear constrained optimisation and least-square problems. The sensitivity analysis required within the optimisation framework is pursued in this work with a variational approach and is outlined in Sec. 6. As a result, the required variations of the continuum mechanical quantities for calculating the derivative of the objective function and constraints are integrated based on a differential geometric consideration. For this purpose, a local convective parameter space is considered in the kinematics; see Figure 3.1. This allows the variation to be split into parts of the displacement, the concentrations and the geometry. Analogous to continuum mechanics, the continuous equations are first varied and then discretised, see Sec. 4. Thus, the discretised tangential stiffness for solving the structural analysis and the tangential sensitivities for solving the sensitivity analysis are provided simultaneously. The analytical derived tangential sensitivities with respect to a change of geometrical design parameters and material design parameters are comprehensively verified in Sec. 7.3 and Sec. 7.4 with numerical comparisons to ensure correct implementation. Furthermore, the verification illustrates, in particular, the time efficiency of the applied variational approach. Finally, the requirements for the integration of history-dependent sensitivities, which have to be taken into account due to the time-dependent concentrations, are fulfilled by introducing a tangential sensitivity for the history field in Sec. 6.6.1.

The combination and programming implementation of the structural analysis and structural optimisation are presented in Sec. 2.0.3 at the beginning of the work to provide a better overview. A simulation tool is developed in MATLAB, which interfaces with a FORTRAN code and the Gmsh software. With this, the numerical fundamentals of the structural analysis of a mechanical-chemical-degradation model are integrated into a mathematical optimisation algorithm for shape and material parameter optimisation. Due to the provision of analytically derived variations and the exploitation of the program's technical advantage, a fast, efficient and at the same time reliable optimisation can be achieved. The CAGD-based features of the interface Gmsh provide a parameterised structural mesh for the automatic update of geometrical design parameters.

The last sub-objective is fulfilled at the end of the thesis. The numerical investigations listed in Sec. 7 serve to elaborate the coupling of the mechanical-chemical-degradation model and to give a state of proof. In particular, the implementation of the derived sensitivities with respect to design changes and material changes is checked through numerical comparative calculations. Convergence studies considering spatial and temporal approximation are presented to ensure sufficiently accurate results of the structural analysis. Finally, a practical reference of the developed mechanical-chemical-degradation model is presented in Sec. 8. Here, a boundary value problem is calculated, which reminds of a hollow concrete block suffering under chemical impact such as in calcium leaching processes. The examples show the time-dependent deterioration of the block due to material degradation triggered by concentration. Shape optimisation of the hollow block in Sec. 9 enables a reduction in the influence of the concentrations on the mechanical stresses. The optimisation task is evaluated in detail and compared with numerical calculations to prove the implementation of the analytical derived optimisation solution. Another example of shape optimisation is reminiscent of a bridge and the goal is a material saving that still maintains the maximum load-bearing capacity. However, chemical concentrations are taken into account in addition to mechanical loads. In particular, considering the time-dependent exposure of the concentrations is highlighted to illustrate that the influence of the concentrations occurs gradually over time and can lead to a serious loss of bearing capacity over a longer period. The presented optimisation algorithm takes the temporal degradation into account and enables a reliable optimisation. Sec. 10 gives examples of how to optimise the material parameters. The aim is to reduce and control chemical reactions and the associated material degradation by modifying the material parameters. In the first example, the displacement resulting from chemical concentrations is minimised. In the second example, the material parameters of the bridge-like structure are adjusted in such a way, where the more vulnerable area of the bridge is less affected by the diffusive chemical concentrations.

Both shape and material parameter optimisation are presented to control and optimise the harmful effects of chemicals and other long-term influences. In all examples, the numerical comparisons serve to validate the results and to illustrate the time efficiency of the provided variational (analytical) approach.

11.2. Outlook

This thesis presents a general model for the optimisation of diffusion-driven degradation processes. On a theoretical as well as on a practical level, the work offers further research aspects.

One open research topic is an alternative application of the introduced degradation space referred to the parameter vector space. Within the framework of this work, the degradation implementation is realised with a combined kinematic and constitutive approach. The kinematic representation using a split of the deformation gradient into an elastic and a degradation part is a well-established approach. However, this work still offers the possibility of an alternative approach to consider degradation on a kinematic level. In [8] this alternative approach is presented by separating all fundamental quantities on the kinematic level and taking into account the evolution of the body. Additionally, the growth/degradation space is pulled back to the parameter space. In this way, growth processes (analogous to degradation processes) can be integrated, taking into account the changing quantity of substances (such as atoms, molecules or ions). This means that the classical material body in the reference configuration is not dependent on a constant mass. To apply this approach, the gradient operators and tangent mappings are needed to guarantee transport between the configurations. Related to this work, the introduced local degradation gradient $\mathbf{G}$ can be applied to ensure the transformation from the parameter space to the degradation space. The decomposition of the deformation gradient can be illustrated with the local gradients as follows

$$\begin{aligned} \mathbf{F}_d &= \mathbf{G}\,\mathbf{K}^{-1} = (\boldsymbol{h}_i \otimes \boldsymbol{Z}^i)\,(\boldsymbol{Z}_j \otimes \boldsymbol{G}^j) = \boldsymbol{h}_i \otimes \boldsymbol{G}^i \\ \mathbf{F}_e &= \mathbf{M}\,\mathbf{G}^{-1} = (\boldsymbol{g}_i \otimes \boldsymbol{Z}^i)\,(\boldsymbol{Z}_j \otimes \boldsymbol{h}^j) = \boldsymbol{g}_i \otimes \boldsymbol{h}^i\,. \end{aligned} \tag{11.1}$$

Related to the practical application of the work, investigations can be carried out to compare and validate the structural analytical model with experimental data. Therefore, the model can be prepared to be used for problems such as calcium leaching or chemical attack in the context of problems in civil engineering structures. However, it must be taken into account that the complexity of the approximate value problems will increase with a closer connection to practical tasks. An alternative approach to the applied CAGD-based shape optimisation should be considered for more complex boundary value problems. For example, the mesh-based parameterisation approach manipulates an existing FE-mesh. As outlined in [73], the shape optimisation requires fewer design parameters and re-meshing is not necessary. In addition, a design exploration approach could be used to investigate design alternatives for complex tasks with a high number of design parameters and identify optimal performance parameters. A singular value decomposition (SVD) could provide insight into sensitivity analysis and identify the design parameters with the greatest influence on structural response, see e.g. [52, 84, 11].

A. Appendix

A.1. Variations of Certain Continuum Mechanical Quantities

The present model problem is a coupled nonlinear system of differential equations to be solved by numerical methods. For this reason, the required variations of the continuum mechanical values, which are needed in the framework of the structural analysis and the sensitivity analysis, are determined. The required variations are derived in this section and are used for the application of the following sections.

For the structural analysis and the structural optimisation, variations of continuum mechanical values are required. Within the structural analysis, the variation of the weak formula with respect to the state variables are applied. Therefore, the following parameters are introduced with $\boldsymbol{\nu}\{\boldsymbol{u}, c_\gamma\} \in \mathcal{V}$, wherein the displacements $\boldsymbol{u}$ and concentrations c_γ are the state variables of the structural problem. The total variation of an arbitrary function $f(\boldsymbol{\nu}) : \mathcal{V} \to \mathbb{R}$ reads,

$$\delta f \;=\; \delta_u J(\boldsymbol{u}, c_\gamma; \delta\boldsymbol{u}) \;+\; \delta_{c_\gamma} J(\boldsymbol{u}, c_\gamma; \delta c_\gamma)\,. \tag{A.1}$$

In the framework of the structural optimisation problem, the geometry $\boldsymbol{X}$ and furthermore, the material parameters $\boldsymbol{m}$ are considered as design parameters, which can change in order to optimise the solution. It must be noted that both state variables depend directly on the geometry of the structure $\boldsymbol{\nu}(\boldsymbol{X})$. Therefore, an exemplary total partial variation of an arbitrary function $J(\boldsymbol{\nu}, \boldsymbol{X}) \,:\, \mathcal{V} \times \mathcal{S} \to \mathbb{R}$ with respect to the geometry, respectively material, is composed of the following partial variations, i.e.

$$\begin{aligned} D_s f(\boldsymbol{\nu}(\boldsymbol{X}), \boldsymbol{X}) \quad &= \quad \frac{\partial f}{\partial \boldsymbol{X}} + \frac{\partial f}{\partial \boldsymbol{u}}\frac{\mathrm{d}\boldsymbol{u}}{\mathrm{d}\boldsymbol{X}} + \frac{\partial f}{\partial c_\gamma}\frac{\mathrm{d}c_\gamma}{\mathrm{d}\boldsymbol{X}} \\ D_m f(\boldsymbol{\nu}(\boldsymbol{m}), \boldsymbol{m}) \quad &= \quad \frac{\partial f}{\partial \boldsymbol{m}} + \frac{\partial f}{\partial \boldsymbol{u}}\frac{\mathrm{d}\boldsymbol{u}}{\mathrm{d}\boldsymbol{m}} + \frac{\partial f}{\partial c_\gamma}\frac{\mathrm{d}c_\gamma}{\mathrm{d}\boldsymbol{m}}\,. \end{aligned} \tag{A.2}$$

Thus, this section prepares the partial variations of the relevant quantities for both, the structural analysis and structural optimisation solution, i.e. $\delta_X(\bullet), \delta_u(\bullet), \delta_{c_\gamma}(\bullet)$ and $\delta_m(\bullet)$. The total variations follow as this work proceeds.

A.1.1. Partial Variations of the First Piola-Kirchhoff Stress

In the following, the partial variations of the first Piola-Kirchhoff tensor $\mathbf{P}$ from Eq. (3.69.1) with respect to the geometry $\delta_X \mathbf{P}$ and the displacement $\delta_u \mathbf{P}$ are introduced,

$$\begin{aligned} \delta_X \mathbf{P} &= \frac{\partial \mathbf{P}}{\partial \mathbf{F}} : \delta_X \mathbf{F} = \mathbb{P} : \delta_X \mathbf{F} \\ \delta_u \mathbf{P} &= \frac{\partial \mathbf{P}}{\partial \mathbf{F}} : \delta_X \mathbf{F} = \mathbb{P} : \delta_u \mathbf{F} \,, \end{aligned} \tag{A.3}$$

wherein the partial variations of the deformation gradient from Eq. (3.27.2) and (3.27.3) are applied. For the partial variation with respect to the deformation gradient a tensor of fourth-order $\mathbb{P}$ is applied with

$$\mathbb{P} := \frac{\partial \mathbf{P}}{\partial \mathbf{F}} \,, \tag{A.4}$$

which results in the component representation with

$$\mathrm{P}_{ijkl} = \frac{\partial \mathrm{P}_{ij}}{\partial \mathrm{F}_{kl}} = \frac{\rho_0}{\rho_0^*} \left[\mu \, \frac{\partial \mathrm{F}^e_{io}}{\partial \mathrm{F}_{kl}} \, (\mathrm{F}^d_{jo})^{-1} + \lambda \, \frac{\partial (J_e^2 - J_e)}{\partial \mathrm{F}_{kl}} \, \mathrm{F}^{-1}_{ji} + [-\mu + \lambda \, (J_e^2 - J_e)] \, \frac{\partial \mathrm{F}^{-1}_{ji}}{\partial \mathrm{F}_{kl}} \right] . \tag{A.5}$$

Therein the following connections are derived with

$$\begin{aligned} \frac{\partial \mathrm{F}^e_{io}}{\partial \mathrm{F}_{kl}} \, (\mathrm{F}^d_{jo})^{-1} &= 1_{ik} \, \mathrm{C}^{-1}_{lj} &&:= \mathbb{U}_{ijkl} \\ \frac{\partial \mathrm{F}^{-1}_{ji}}{\partial \mathrm{F}_{kl}} &= -\mathrm{F}^{-1}_{li} \, \mathrm{F}^{-1}_{jk} &&:= \mathbb{W}_{ijkl} \,. \end{aligned} \tag{A.6}$$

Furthermore, the partial variation of the determinant of the elastic part of the deformation gradient with respect to the deformation gradient results in

$$\frac{\partial J_e}{\partial \mathbf{F}} = J_e \, \mathbf{F}^{-\mathrm{T}} \,, \tag{A.7}$$

so that the fourth-order $\mathbb{P}$ follows with

$$\mathbb{P} = \frac{\rho_0}{\rho_0^*} \left[\mu \, \mathbb{U} + \lambda \, (2 \, J_e^2 - J_e) \, \mathbf{F}^{-\mathrm{T}} \otimes \mathbf{F}^{-\mathrm{T}} + [-\mu + \lambda \, (J_e^2 - J_e)] \, \mathbb{W} \right] . \tag{A.8}$$

Moreover, the partial variation of the first Piola-Kirchhoff is dependent on the chemicals, so that the partial derivative is introduced with $\delta_{c_\gamma}\mathbf{P}$. Dependencies on the concentrations, i.e. the referential density $\rho_0(c_\gamma)$, the elastic deformation gradient $\mathbf{F}_e(c_\gamma)$, the determinant of the elastic deformation gradient $J_e(c_\gamma)$ and the growth part of the right Cauchy Green tensor $\mathbf{C}_d(c_\gamma)$ become relevant with

$$\begin{aligned}
\frac{\partial \rho_0}{\partial c_\gamma} &= -M_\gamma\,, & \frac{\partial \mathbf{F}_e}{\partial c_\gamma} &= \frac{1}{3}\left(\frac{\rho_0}{\rho_0^*}\right)^{-4/3}\frac{M_\gamma}{\rho_0^*}\,\mathbf{F} \\
\frac{\partial J_e}{\partial c_\gamma} &= \frac{J_e}{\rho_0}\,M_\gamma \quad \text{and} & \frac{\partial \mathbf{C}_d^{-1}}{\partial c_\gamma} &= \frac{2}{3}\left(\frac{\rho_0}{\rho_0^*}\right)^{-5/3}\frac{M_\gamma}{\rho_0^*}\,\mathbf{1}\,.
\end{aligned} \tag{A.9}$$

Therefore, the partial variation follows with

$$\delta_{c_\gamma}\mathbf{P} = \frac{M_\gamma}{\rho_0^*}\left[-\,\mu\,\mathbf{F}_e\,\mathbf{F}_d^{-\mathrm{T}} + [\mu + \lambda\,J_e^2]\,\mathbf{1}\,\mathbf{F}^{-\mathrm{T}} + \frac{2}{3}\left(\frac{\rho_0}{\rho_0^*}\right)^{-2/3}\mu\,\mathbf{F}\,\mathbf{1}\right]\delta c_\gamma\,. \tag{A.10}$$

A.1.2. Partial Variations of the Second Piola-Kirchhoff Stress

The partial variations of the second Piola-Kirchhoff tensor $\mathbf{S}_K$ from Eq. (3.69.2) is introduced with respect to the geometry $\delta_X\mathbf{S}_K$ and displacement $\delta_u\mathbf{S}_K$,

$$\begin{aligned}
\delta_X\mathbf{S}_K &= \frac{\partial \mathbf{S}_K}{\partial \mathbf{E}} : \delta_X\mathbf{E} = 2\,\frac{\partial \mathbf{S}_K}{\partial \mathbf{C}} : \delta_X\mathbf{E} = \mathbb{C} : \delta_X\mathbf{E} \\
\delta_u\mathbf{S}_K &= \frac{\partial \mathbf{S}_K}{\partial \mathbf{E}} : \delta_u\mathbf{E} = 2\,\frac{\partial \mathbf{S}_K}{\partial \mathbf{C}} : \delta_u\mathbf{E} = \mathbb{C} : \delta_u\mathbf{E}\,.
\end{aligned} \tag{A.11}$$

Therein, the fourth-order tensor $\mathbb{C}$, which play an important role in continuum mechanics appearing as elasticity, can be introduced, i.e.

$$\mathbb{C} := \frac{\partial \mathbf{S}_K}{\partial \mathbf{E}} = 2\,\frac{\partial \mathbf{S}_K}{\partial \mathbf{C}}\,, \tag{A.12}$$

respectively, the component representation reads as

$$\mathrm{C}_{ijkl} = 2\,\frac{\partial \mathrm{S}_{ij}}{\partial \mathrm{C}_{kl}} = 2\,\frac{\rho_0}{\rho_0^*}\left[\lambda\,\frac{\partial(J_e^2 - J_e)}{\partial \mathrm{C}_{kl}}\,\mathrm{C}_{ij}^{-1} + [-\mu + \lambda\,(J_e^2 - J_e)]\,\frac{\partial \mathrm{C}_{ij}^{-1}}{\partial \mathrm{C}_{kl}}\right]. \tag{A.13}$$

Therein the following connections come into play

$$\begin{aligned}
\frac{\partial \mathrm{C}_{ij}}{\partial \mathrm{C}_{kl}} &= \frac{1}{2}\,(\delta_{ik}\,\delta_{jl} + \delta_{il}\,\delta_{jk}) \\
\frac{\partial \mathrm{C}_{ij}^{-1}}{\partial \mathrm{C}_{kl}} &= -\frac{1}{2}\,(\mathrm{C}_{ik}^{-1}\,\mathrm{C}_{jl}^{-1} + \mathrm{C}_{il}^{-1}\,\mathrm{C}_{jk}^{-1}) := \mathbb{V}_{ijkl}\,,
\end{aligned} \tag{A.14}$$

and the partial variation of the elastic deformation gradient J_e with respect to the right Cauchy Green tensor $\mathbf{C}$ is used with

$$\frac{\partial J_e}{\partial \mathbf{C}} = \frac{1}{2}\, J_e\, \mathbf{C}^{-\mathrm{T}} \,. \tag{A.15}$$

With this at hand, the elasticity tensor results in

$$\mathbb{C} = \frac{\rho_0}{\rho_0^*}\left[\lambda\,(2\,J_e^2 \,-\, J_e)\,\mathbf{C}^{-1}\otimes\mathbf{C}^{-\mathrm{T}} \,+\, 2\,[-\mu \,+\, \lambda\,(J_e^2 \,-\, J_e)]\,\mathbb{V}\right]. \tag{A.16}$$

Furthermore, the partial variation of the stress with respect to the concentrations $\delta_{c_\gamma}\mathbf{S}_K$ follows, applying the derivatives from Eq. (A.9), with

$$\delta_{c_\gamma}\mathbf{S}_K = \frac{M_\gamma}{\rho_0^*}\left[-\,\mu\,\mathbf{C}_d^{-1} \,+\, [\mu \,+\, \lambda\,J_e^2]\,\mathbf{C}^{-1} \,+\, \frac{2}{3}\left(\frac{\rho_0}{\rho_0^*}\right)^{-2/3}\mu\,\mathbf{1}\right]\delta c_\gamma\,, \tag{A.17}$$

wherein the second-order tensor $\mathbf{C}_\gamma$ is introduced, i.e.

$$\mathbf{C}_\gamma := \frac{M_\gamma}{\rho_0^*}\left[-\,\mu\,\mathbf{C}_d^{-1} \,+\, [\mu \,+\, \lambda\,J_e^2]\,\mathbf{C}^{-1} \,+\, \frac{2}{3}\left(\frac{\rho_0}{\rho_0^*}\right)^{-2/3}\mu\,\mathbf{1}\right]. \tag{A.18}$$

As the weak formulation is represented as a function of the second Piola-Kirchhoff stress, the sensitivity with respect to the material parameters $\delta_m\mathbf{S}_K$ is also calculated at this point. Therefore, the material vector $\boldsymbol{m}$, referred to Eq. (3.72), is utilised and a vector including the partial variations with respect to the material parameters $\delta_m\mathbf{S}_K$ is following with

$$\delta_m\mathbf{S}_K = \begin{bmatrix} \dfrac{\partial\mathbf{S}_K}{\partial\mu} & \dfrac{\partial\mathbf{S}_K}{\partial\lambda} & \dfrac{\partial\mathbf{S}_K}{\partial\rho_0^*} & \dfrac{\partial\mathbf{S}_K}{\partial M_\gamma} & \dfrac{\partial\mathbf{S}_K}{\partial c_\gamma^{\mathrm{t}=0}} & 0 \end{bmatrix}. \tag{A.19}$$

Therein, the second-order tensors $\mathbf{C}_1, \mathbf{C}_2, \mathbf{C}_3, \mathbf{C}_4$ and $\mathbf{C}_5$ are introduced as

$$\begin{aligned} \mathbf{C}_1 &:= \frac{\partial\mathbf{S}_K}{\partial\mu} = \frac{\rho_0}{\rho_0^*}\,[(\mathbf{C}_d)^{-1} \,-\, \mathbf{C}^{-1}] \\ \mathbf{C}_2 &:= \frac{\partial\mathbf{S}_K}{\partial\lambda} = \frac{\rho_0}{\rho_0^*}\,[(J_e^2 \,-\, J_e)\,\mathbf{C}^{-1}]\,, \end{aligned} \tag{A.20}$$

whereby the partial derivative of the first Lamé constant μ and of the second Lamé constant λ are illustrated. Furthermore, the stress is influenced by the initial density ρ_0^*, the molar mass M_γ and the initial concentration c_γ^0, i.e.

$$
\begin{aligned}
\mathbf{C}_3 \; := \; \frac{\partial \mathbf{S}_K}{\partial \rho_0^*} \; &= \; \frac{\rho_0}{\rho_0^*} \left[\frac{\rho_0^* - \rho_0}{\rho_0^* \, \rho_0} \left[\mu \, (\mathbf{C}_d)^{-1} - (\mu - \lambda \, (J_e - 1) \, J_e) \, \mathbf{C}^{-1} \right] \right. \\
&\quad \left. - \frac{2}{3} \, (\frac{\rho_0}{\rho_0^*})^{-5/3} \, \frac{\rho_0^* - \rho_0}{(\rho_0^*)^2} \, \mathbf{1} + \lambda \, (2 \, J_e - 1) \, J \, (\frac{\rho_0 - \rho_0^*}{\rho_0^2}) \, \mathbf{C}^{-1} \right] \\
\mathbf{C}_4 \; := \; \frac{\partial \mathbf{S}_K}{\partial M_\gamma} \; &= \; \frac{- \, c_\gamma}{\rho_0^*} \left[\mu \, (\mathbf{C}_d)^{-1} - [\mu - \lambda \, (J_e - 1) \, J_e] \, (\mathbf{C}^{-1}) \right] \\
&\quad + \frac{1}{\rho_0} \lambda \, (2 \, J_e - 1) \, J \, c_\gamma \, \mathbf{C}^{-1} + \mu \, \frac{2}{3} \, (\frac{\rho_0}{\rho_0^*})^{-2/3} \, \frac{c_\gamma}{\rho_0^*} \, \mathbf{1} \\
\mathbf{C}_5 \; := \; \frac{\partial \mathbf{S}_K}{\partial c_\gamma^{\mathrm{t}=0}} \; &= \; \mathbf{C}_\gamma \, \frac{\partial c_\gamma}{\partial c_\gamma^{\mathrm{t}=0}} \, .
\end{aligned}
\tag{A.21}
$$

A.1.3. Partial Variations of the Cauchy Stress

The Cauchy stress tensor $\mathbf{T}$ from Eq. (3.68) can be derived by the mapping $\mathbf{T} = J^{-1} \, \mathbf{P} \, \mathbf{F}^{\mathrm{T}}$. Thus, the partial variation with respect to the geometry $\delta_X \mathbf{T}$ results in

$$
\begin{aligned}
\delta_X \mathbf{T} \; &= \; \delta_X J^{-1} \, \mathbf{P} \, \mathbf{F}^{\mathrm{T}} + J^{-1} \, \delta_X \mathbf{P} \, \mathbf{F}^{\mathrm{T}} + J^{-1} \, \mathbf{P} \, \delta_X \mathbf{F}^{\mathrm{T}} \\
&= \; (-J^{-1} \, \mathbf{F}^{-\mathrm{T}} : \delta_X \mathbf{F}) \, \mathbf{P} \, \mathbf{F}^{\mathrm{T}} + J^{-1} \, \delta_X \mathbf{P} \, \mathbf{F}^{\mathrm{T}} + J^{-1} \, \mathbf{P} \, \delta_X \mathbf{F}^{\mathrm{T}} \, ,
\end{aligned}
\tag{A.22}
$$

and is composed of the partial variations $\delta_X \mathbf{F}$ and $\delta_X \mathbf{P}$, cf. Eq. (3.27.3) and (A.3.1). Moreover, the partial variation with respect to the displacement $\delta_u \mathbf{T}$ follows with

$$
\begin{aligned}
\delta_u \mathbf{T} \; &= \; \delta_u J^{-1} \, \mathbf{P} \, \mathbf{F}^{\mathrm{T}} + J^{-1} \, \delta_u \mathbf{P} \, \mathbf{F}^{\mathrm{T}} + J^{-1} \, \mathbf{P} \, \delta_u \mathbf{F}^{\mathrm{T}} \\
&= \; (-J^{-1} \, \mathbf{F}^{-\mathrm{T}} : \delta_u \mathbf{F}) \, \mathbf{P} \, \mathbf{F}^{\mathrm{T}} + J^{-1} \, \delta_u \mathbf{P} \, \mathbf{F}^{\mathrm{T}} + J^{-1} \, \mathbf{P} \, \delta_u \mathbf{F}^{\mathrm{T}} \, ,
\end{aligned}
\tag{A.23}
$$

with reference to the Eq. (3.27.2) and (A.3.2). Finally, the partial variation with respect to the concentration $\delta_{c_\gamma} \mathbf{T}$ results in

$$
\delta_{c_\gamma} \mathbf{T} \; = \; J^{-1} \, \delta_{c_\gamma} \mathbf{P} \, \mathbf{F}^{\mathrm{T}} \, ,
\tag{A.24}
$$

and $\delta_{c_\gamma} \mathbf{P}$ from Eq. (A.10).

A.1.4. Partial Variations of the Concentration Flux

In addition to the variations of the stresses, the concentration flux $\boldsymbol{J}_\gamma$ from Eq. (3.63) is a relevant vector that influences the structural analysis and optimisation solution. Therefore, the total partial variation with respect to the geometry $\delta_X \boldsymbol{J}_\gamma$ and the partial variation with dependency of the displacement $\delta_u \boldsymbol{J}_\gamma$ are derived as follows

$$\begin{aligned} \delta_X \boldsymbol{J}_\gamma &= \frac{\partial \boldsymbol{J}_\gamma}{\partial \boldsymbol{X}} + \frac{\partial \boldsymbol{J}_\gamma}{\partial \mathbf{E}} : \delta_X \mathbf{E} = \frac{\partial \boldsymbol{J}_\gamma}{\partial \boldsymbol{X}} + 2\,\frac{\partial \boldsymbol{J}_\gamma}{\partial \mathbf{C}} : \delta_X \mathbf{E} \\ \delta_u \boldsymbol{J}_\gamma &= \frac{\partial \boldsymbol{J}_\gamma}{\partial \mathbf{E}} : \delta_u \mathbf{E} = 2\,\frac{\partial \boldsymbol{J}_\gamma}{\partial \mathbf{C}} : \delta_u \mathbf{E}\,, \end{aligned} \tag{A.25}$$

again, the geometric variations $\delta_X \mathbf{E}$ and $\delta_u \mathbf{E}$ from Eq. (3.28) can be utilised. Moreover, the partial variation of the material flux with respect to the right Cauchy Green tensor $\mathbf{C}$ follows with

$$\mathbb{A} := 2\,\frac{\partial \boldsymbol{J}_\gamma}{\partial \mathbf{C}} = -2\,D\,\mathrm{Grad}\;c_\gamma\,\frac{\partial J}{\partial \mathbf{C}}\,\mathbf{C}^{-1} - 2\,D\,\mathrm{Grad}\;c_\gamma\,J\,\frac{\partial \mathbf{C}^{-1}}{\partial \mathbf{C}}\,. \tag{A.26}$$

The third-order tensor $\mathbb{A}$ is introduced. Under consideration of the partial variation of the deformation gradient J with respect to the right Cauchy Green tensor as

$$\frac{\partial J}{\partial \mathbf{C}} = \frac{1}{2}\,J\,\mathbf{C}^{-\mathrm{T}}\,, \tag{A.27}$$

and the connection from Eq. (A.14.2), the component illustration follows, i.e.

$$\mathbb{A}_{jkl} = -J\,D\,(\mathrm{Grad}\;c_\gamma)_i \left[\mathrm{C}^{-1}_{lk}\,\mathrm{C}^{-1}_{ij} - \mathrm{C}^{-1}_{ik}\,\mathrm{C}^{-1}_{jl} - \mathrm{C}^{-1}_{il}\,\mathrm{C}^{-1}_{jk} \right]. \tag{A.28}$$

Due to the direct dependency of the flux on the geometry, the partial variation $\dfrac{\partial \boldsymbol{J}_\gamma}{\partial \boldsymbol{X}}$ is derived via the following second-order tensor $\mathbf{A}_\gamma$,

$$\mathbf{A}_\gamma := \frac{\partial \boldsymbol{J}_\gamma}{\partial \boldsymbol{X}} = D\,\mathrm{Grad}\;c_\gamma\,\mathrm{Grad}\;\delta \boldsymbol{X}\,J\,\mathbf{C}^{-1}\,. \tag{A.29}$$

The partial variations of the concentration flux can be summarised as follows

$$\delta_X \boldsymbol{J}_\gamma = \mathbf{A}_\gamma + \mathbb{A} : \delta_X \mathbf{E} \qquad \text{and} \qquad \delta_u \boldsymbol{J}_\gamma = \mathbb{A} : \delta_u \mathbf{E}\,. \tag{A.30}$$

Moreover, the partial variation of the concentration flux with respect to the concentration $\delta_{c_\gamma} \boldsymbol{J}_\gamma$ is derived as

$$\delta_{c_\gamma} \boldsymbol{J}_\gamma = -\,J\,D\,\mathrm{Grad}\;\delta c_\gamma\,\mathbf{C}^{-1}\,. \tag{A.31}$$

Finally, the partial variations with respect to the material parameters $\delta_m \boldsymbol{J}_\gamma$ are required, whereby only the partial variation of the flux according to the diffusion parameter D becomes relevant, i.e.

$$\delta_m \boldsymbol{J}_\gamma = \begin{bmatrix} 0 & 0 & 0 & 0 & 0 & \dfrac{\partial \boldsymbol{J}_\gamma}{\partial D} \end{bmatrix} , \tag{A.32}$$

wherein the following vector $\boldsymbol{C}_6$ is introduced as follows

$$\boldsymbol{C}_6 := \frac{\partial \boldsymbol{J}_\gamma}{\partial D} = - J \,\mathrm{Grad}\, c_\gamma \, \mathbf{C}^{-1} . \tag{A.33}$$

Bibliography

[1] Welcome to the home of GNU Fortran. `https://gcc.gnu.org/fortran/`.

[2] H. Altenbach. *Kontinuumsmechanik*. Springer, 2012. `http://dx.doi.org/10.1007/978-3-662-47070-1`.

[3] D. Ambrosi and F. Mollica. On the mechanics of a growing tumor. *International Journal of Engineering Science*, 40(12):1297–1316, 2002. `https://doi.org/10.1016/S0020-7225(02)00014-9`.

[4] M. V. O. Araujo, E. N. Lages, and M. A. A. Cavalcante. Checkerboard free topology optimization for compliance minimization applying the finite–volume theory. *Mechanics Research Communications*, 108:103581, 2020. `http://dx.doi.org/https://doi.org/10.1016/j.mechrescom.2020.103581`.

[5] N. Bakhtiary, P. Allinger, M. Friedrich, F. Mulfinger, J. Sauter, O. Müller, and M. Puchinger. A new approach for sizing, shape and topology optimization. *SAE Technical Paper 960814*, 105:745–761, 1996. `https://doi.org/10.4271/960814`.

[6] F.-J. Barthold. *Zur Kontinuumsmechanik inverser Geometrieprobleme*. TU Braunschweig, 2002. `http://dx.doi.org/10.17877/DE290R-13502`.

[7] F.-J. Barthold. Remarks on variational shape sensitivity analysis based on local coordinates. *Engineering Analysis with Boundary Elements*, 32:971–985, 2008. `https://doi.org/10.1016/j.enganabound.2007.09.007`.

[8] F.-J. Barthold. A structural optimisation viewpoint on growth phenomena. *Bulletin of the Polish Academy of Sciences: Technical Sciences*, pages 247–252, 2012. `https://doi.org/10.2478/v10175-012-0033-6`.

[9] F.-J. Barthold. *Theorie und Numerik zur Berechnung und Optimierung von Strukturen aus isotropen, hyperelastischen Materialien*. Universität Hannover, PhD thesis, 1993. `http://dx.doi.org/10.17877/DE290R-7352`.

[10] F.-J. Barthold, N. Gerzen, W. Kijanski, and D. Materna. Efficient Variational Design Sensitivity Analysis. In *Mathematical Modeling and Optimization of Complex Structures*, pages 229–257. Springer, 2016. `https://doi.org/10.1007/978-3-319-23564-6_14`.

[11] F.-J. Barthold and J. Liedmann. Remarks on variational sensitivity analysis of elastoplastic deformations. In *AIP Conference Proceedings*, volume 1896, page 100007. AIP Publishing LLC, 2017. `http://dx.doi.org/10.1063/1.5008125`.

[12] F.-J. Barthold and D. Materna. Remarks on Different Strategies for Variational Design Sensitivity Analysis. In *7th world congress on structural and multidisciplinary optimization. Paper*, pages 1348–1357, 2007.

[13] F.-J. Barthold and E. Stein. A continuum mechanical–based formulation of the variational sensitivity analysis in structural optimization. Part 1: Analysis. *Structural Optimization*, 11(1–2):29–42, 1996. `https://doi.org/10.1007/BF01279652`.

[14] K.-J. Bathe. *Finite–Elemente–Methoden.* Springer, 2002. `https://doi.org/10.1007/978-3-322-83108-8_16`.

[15] E. Becker and W. Bürger. *Kontinuumsmechanik: eine Einführung in die Grundlagen und einfache Anwendungen.* Springer, 2013. `https://doi.org/10.1007/978-3-663-12198-5`.

[16] C. L. Bellégo, B. Gérard, and G. Pijaudier-Cabot. Chemo–Mechanical Effects in Mortar Beams Subjected to Water Hydrolysis. *Journal of engineering mechanics*, 126(3):266–272, 2000. `https://doi.org/10.1061/(ASCE)0733-9399(2000)126:3(266)`.

[17] M. P. Bendsøe. *Optimization of Structural Topology, Shape, and Material.* Springer, 1995. `http://dx.doi.org/10.1007/978-3-662-03115-5`.

[18] M. P. Bendsøe and O. Sigmund. *Topology Optimization: Theory, Methods, and Applications.* Springer, 2004. `http://dx.doi.org/10.1007/978-3-662-05086-6`.

[19] A. Bertram. *Axiomatische Einführung in die Kontinuumsmechanik.* BI–Wiss.–Verlag, 1989. `https://d-nb.info/891051260/04`.

[20] J. Betten. *Kontinuumsmechanik: Elasto–, Plasto–und Kriechmechanik.* Springer, 1993. `https://doi.org/10.1007/978-3-662-08168-6`.

[21] J. Betten. *Finite Elemente für Ingenieure 1: Grundlagen, Matrixmethoden, Elastisches Kontinuum.* Springer, 2003. `https://doi.org/10.1007/978-3-642-55536-7`.

[22] K.-U. Bletzinger, M. Firl, J. Linhard, and R. Wüchner. Optimal shapes of mechanically motivated surfaces. *Computer Methods in Applied Mechanics and Engineering*, 199(5–8):324–333, 2010. `https://doi.org/10.1016/j.cma.2008.09.009`.

[23] J. Bonet and R. D. Wood. *Nonlinear Continuum Mechanics for Finite Element Analysis.* Cambridge University Press, 2008. `https://doi.org/10.1017/CBO9780511755446`.

[24] R. M. Bowen. Porous Media Model Formulations by the Theory of Mixtures. *Fundamentals of Transport Phenomena in Porous Media*, 82:63–119, 1984. `https://doi.org/10.1007/978-94-009-6175-3_2`.

[25] V. Braibant and C. Fleury. Shape optimal design using B–splines. *Computer Methods in Applied Mechanics and Engineering*, 44(3):247–267, 1984. `https://doi.org/10.1016/0045-7825(84)90132-4`.

[26] U. Cella, C. Groth, and M. E. Biancolini. Geometric Parameterization Strategies for shape Optimization Using RBF Mesh Morphing. In *Advances on Mechanics, Design Engineering and Manufacturing*, pages 537–545. Springer, 2017. `https://doi.org/10.1007/978-3-319-45781-9_54`.

[27] Y. Chen, J. Cheng, Y. Jiang, and K. Liu. A time delay dynamical model for outbreak of 2019–nCoV and the parameter identification. *Journal of Inverse and Ill–posed Problems*, 28(2):243–250, 2020. `https://doi.org/10.1515/jiip-2020-0010`.

[28] Y.-C. Chen and A. Hoger. Constitutive Functions of Elastic Materials in Finite Growth and Deformation. In *Advances in Continuum Mechanics and Thermodynamics of Material Behavior*, pages 175–193. Springer, 2000. `https://doi.org/10.1023/A:1011061400438`.

[29] S. A. Chester and L. Anand. A coupled theory of fluid permeation and large deformations for elastomeric materials. *Journal of the Mechanics and Physics of Solids*, 58(11):1879–1906, 2010. `https://doi.org/10.1016/j.jmps.2010.07.020`.

[30] K. K. Choi and E. J. Haug. Shape Design Sensitivity Analysis of Elastic Structures. *Journal of Structural Mechanics*, 11(2):231–269, 1983. `https://doi.org/10.1080/03601218308907443`.

[31] K. K. Choi and N.-H. Kim. *Structural Sensitivity Analysis and Optimization 2: Nonlinear Systems and Applications*. Springer-Verlag New York, 2005. `https://doi.org/10.1007/b138895`.

[32] Y. S. Choi and E. I. Yang. Effect of calcium leaching on the pore structure, strength, and chloride penetration resistance in concrete specimens. *Nuclear Engineering and Design*, 259:126–136, 2013. `https://doi.org/10.1016/j.nucengdes.2013.02.049`.

[33] P. W. Christensen and A. Klarbring. *An Introduction to Structural Optimization*, volume 153 of *Solid Mechanics and Its Applications*. Springer, 2008. `https://doi.org/10.1007/978-1-4020-8666-3`.

[34] B. D. Coleman and W. Noll. The thermodynamics of elastic materials with heat conduction and viscosity. *Archive for Rational Mechanics and Analysis*, 13:167–178, 1963. `https://doi.org/10.1007/BF01262690`.

[35] S. Cowin and D. Hegedus. Bone remodeling 1: theory of adaptive elasticity. *Journal of Elasticity*, 6(3):313–326, 1976. `https://doi.org/10.1007/BF00041724`.

[36] H. L. Cox. *The Design of Structures of Least Weight*. Elsevier, 1965. `https://doi.org/10.1016/C2013-0-07840-1`.

[37] L. De Windt and P. Devillers. Modeling the degradation of Portland cement pastes by biogenic organic acids. *Cement and Concrete Research*, 40(8):1165–1174, 2010. `https://doi.org/10.1016/j.cemconres.2010.03.005`.

[38] S. Degertekin and M. Hayalioglu. Sizing truss structures using teaching–learning–based optimization. *Computers & Structures*, 119:177–188, 2013. `https://doi.org/10.1016/j.compstruc.2012.12.011`.

[39] D. J. Docimo, Z. Kang, K. A. James, and A. G. Alleyne. A Novel Framework for Simultaneous Topology and Sizing Optimization of Complex, Multi–Domain Systems–of–Systems. *Journal of Mechanical Design*, 142(9), 2020. `https://doi.org/10.1115/1.4046066`.

[40] T. Elguedj and T. J. Hughes. Isogeometric analysis of nearly incompressible large strain plasticity. *Computer Methods in Applied Mechanics and Engineering*, 268:388–416, 2014. `https://doi.org/10.1016/j.cma.2013.09.024`.

[41] M. Epstein and G. A. Maugin. Material evolution in plasticity and growth. In *Continuum Thermomechanics*, pages 153–162. Springer, 2000. `https://doi.org/10.1007/0-306-46946-4_11`.

[42] G. Farin. *Curves and surfaces for CAGD: a practical guide.* Morgan Kaufmann, 2002. `https://doi.org/10.1016/B978-1-55860-737-8.X5000-5`.

[43] M. Firl, R. Wüchner, and K.-U. Bletzinger. Regularization of shape optimization problems using FE-based parametrization. *Structural and Multidisciplinary Optimization*, 47(4):507–521, 2013. `https://doi.org/10.1007/s00158-012-0843-z`.

[44] F. Flager, A. Adya, J. Haymaker, and M. Fischer. A bi–level hierarchical method for shape and member sizing optimization of steel truss structures. *Computers & Structures*, 131:1–11, 2014. `https://doi.org/10.1016/j.compstruc.2013.10.004`.

[45] J.-F. Ganghoffer. Mechanical modeling of growth considering domain variation–Part II: Volumetric and surface growth involving Eshelby tensors. *Journal of the Mechanics and Physics of Solids*, 58(9):1434–1459, 2010. `https://doi.org/10.1016/j.jmps.2010.05.003`.

[46] J.-F. Ganghoffer and B. Haussy. Mechanical modeling of growth considering domain variation. Part I: constitutive framework. *International Journal of Solids and Structures*, 42(15):4311–4337, 2005. `https://doi.org/10.1016/j.ijsolstr.2005.01.011`.

[47] J.-F. Ganghoffer, P. I. Plotnikov, and J. Sokołowski. Mathematical Modeling of Volumetric Material Growth in Thermoelasticity. *Journal of Elasticity*, 117(1):111–138, 2014. `https://doi.org/10.1007/s10659-014-9467-4`.

[48] C. Geiger and C. Kanzow. *Theorie und Numerik restringierter Optimierungsaufgaben.* Springer, 2002. `http://dx.doi.org/10.1007/978-3-642-56004-0`.

[49] B. Gérard, C. Le Bellego, and O. Bernard. Simplified modelling of calcium leaching of concrete in various environments. *Materials and Structures*, 35(10):632–640, 2002. `https://doi.org/10.1007/BF02480356`.

[50] B. Gerard, G. Pijaudier-Cabot, and C. Laborderie. Coupled diffusion–damage modelling and the implications on failure due to strain localisation. *International Journal of Solids and Structures*, 35(31–32):4107–4120, 1998. `https://doi.org/10.1016/S0020-7683(97)00304-1`.

[51] B. Gerard, G. Pijaudier-Cabot, and C. Le Bellego. *Mechanical Stability Analysis of Cement–Based Materials Submitted to Calcium Leaching: A Review.* IASMiRT, 1999. `http://www.lib.ncsu.edu/resolver/1840.20/30158`.

[52] N. Gerzen. *Analysis and Applications of Variational Sensitivity Information in Structural Optimisation.* Shaker Verlag, 2014. `https://doi.org/10.2370/9783844029376`.

[53] N. Gerzen, D. Materna, and F.-J. Barthold. The inner structure of sensitivities in nodal based shape optimisation. *Computational Mechanics*, 49(3):379–396, 2012. `https://doi.org/10.1007/s00466-011-0648-8`.

[54] C. Geuzaine and J.-F. Remacle. Gmsh: A 3–D finite element mesh generator with built–in pre–and post–processing facilities. *International Journal for Numerical Methods in Engineering*, 79(11):1309–1331, 2009. `https://doi.org/10.1002/nme.2579`.

[55] R. Gleason and J. Humphrey. Effects of a sustained extension on arterial growth and remodeling: a theoretical study. *Journal of Biomechanics*, 38(6):1255–1261, 2005. `https:`

//doi.org/10.1016/j.jbiomech.2004.06.017.

[56] R. Greve. *Kontinuumsmechanik: Ein Grundkurs für Ingenieure und Physiker*. Springer, 2013. `http://dx.doi.org/10.1007/978-3-642-55485-8`.

[57] F. Guhr, L. Sprave, F.-J. Barthold, and A. Menzel. Computational shape optimisation for a gradient–enhanced continuum damage model. *Computational Mechanics*, 65(4):1105–1124, 2020. `https://doi.org/10.1007/s00466-019-01810-3`.

[58] R. B. Haber. A New Variational Approach to Structural Shape Design Sensitivity Analysis. In *Computer Aided Optimal Design: Structural and Mechanical Systems*, pages 573–587. Springer, 1987. `https://doi.org/10.1007/978-3-642-83051-8_16`.

[59] F. Häfner, D. Sames, and H.-D. Voigt. Parameteridentifikation. In *Wärme–und Stofftransport*, pages 546–564. Springer, 1992. `http://dx.doi.org/https://doi.org/10.1007/978-3-662-00982-6_11`.

[60] R. T. Haftka and R. V. Grandhi. Structural shape optimization–A survey. *Computer Methods in Applied Mechanics and Engineering*, 57(1):91–106, 1986. `https://doi.org/10.1016/0045-7825(86)90072-1`.

[61] T. P. Harrigan and J. J. Hamilton. An analytical and numerical study of the stability of bone remodelling theories: Dependence on microstructural stimulus. *Journal of Biomechanics*, 25(5):477–488, 1992. `https://doi.org/10.1016/0021-9290(92)90088-I`.

[62] E. J. Haug and J. S. Arora. Design sensitivity analysis of elastic mechanical systems. *Computer Methods in Applied Mechanics and Engineering*, 15(1):35–62, 1978. `https://doi.org/10.1016/0045-7825(78)90004-X`.

[63] E. J. Haug and J. Cea. *Optimization of Distributed Parameter Structures–Volume II*, volume 50. Springer, 1981.

[64] W. S. Hemp. Theory of structural design. 1958. `http://dspace.lib.cranfield.ac.uk/handle/1826/8688`.

[65] F. H. Heukamp, F.-J. Ulm, and J. T. Germaine. Poroplastic properties of calcium–leached cement–based materials. *Cement and concrete research*, 33(8):1155–1173, 2003. `https://doi.org/10.1016/S0008-8846(03)00024-3`.

[66] M. Hojjat, E. Stavropoulou, and K.-U. Bletzinger. The Vertex Morphing method for node–based shape optimization. *Computer Methods in Applied Mechanics and Engineering*, 268:494–513, 2014. `https://doi.org/10.1016/j.cma.2013.10.015`.

[67] A. G. Holzapfel. Nonlinear Solid Mechanics: A Continuum Approach for Engineering Science. *Meccanica*, 37:489–490, 2002. `https://doi.org/10.1023/A:1020843529530`.

[68] T. J. Hughes. *The Finite Element Method: Linear Static and Dynamic Finite Element Analysis*. Courier Corporation, 2000. `https://doi.org/10.1111/j.1467-8667.1989.tb00025.x`.

[69] N. Ismail, T. Nonaka, S. Noda, and T. Mori. Effect of Carbonation on Microbial Corrosion of Concretes. *Doboku Gakkai Ronbunshu*, 1993(474):133–138, 1993. `https://doi.org/10.2208/jscej.1993.474_133`.

[70] C. Kafadar and A. C. Eringen. Micropolar media–I the classical theory. *International Journal of Engineering Science*, 9(3):271–305, 1971. `https://doi.org/10.1016/0020-7225(71)90040-1`.

[71] G. Karadere, Y. Düzcan, and A. R. Yıldız. Light–weight design of automobile suspension components using topology and shape optimization techniques. *Materials Testing*, 62(5):454–458, 2020. `https://doi.org/10.3139/120.111503`.

[72] S. Kibsgaard. Sensitivity analysis–the basis for optimization. *International Journal for Numerical Methods in Engineering*, 34(3):901–932, 1992. `https://doi.org/10.1002/nme.1620340315`.

[73] W. Kijanski. *Optimal Material Design based on Variational Sensitivity Analysis*. Shaker Verlag, 2019.

[74] T.-H. Kim and J.-I. Byun. Truss Sizing Optimization with a Diversity–Enhanced Cyclic Neighborhood Network Topology Particle Swarm Optimizer. *Mathematics*, 8(7):1087, 2020. `https://doi.org/10.3390/math8071087`.

[75] U. Kirsch. *Structural Optimization: Fundamentals and Applications*. Springer, 1993. `http://dx.doi.org/10.1007/978-3-642-84845-2`.

[76] S. Klinge and P. Steinmann. Inverse analysis for heterogeneous materials and its application to viscoelastic curing polymers. *Computational Mechanics*, 55(3):603–615, 2015. `https://doi.org/10.1007/s00466-015-1126-5`.

[77] M. Knez, M. Peternell, and J. G. Alcázar. From theoretical to applied geometry–recent developments. *Computer Aided Geometric Design*, 2020. `https://doi.org/10.1016/j.cagd.2020.101912`.

[78] D. Kuhl. *Modellierung und Simulation von Mehrfeldproblemen der Strukturmechanik*. Shaker Verlag, 2005.

[79] D. Kuhl, F. Bangert, and G. Meschke. Coupled chemo–mechanical deterioration of cementitious materials. Part I: Modeling. *International Journal of Solids and Structures*, 41:15–40, 2004. `https://doi.org/10.1016/j.ijsolstr.2003.08.005`.

[80] E. Kuhl, A. Menzel, and P. Steinmann. Computational modeling of growth. *Computational Mechanics*, 32(1–2):71–88, 2003. `https://doi.org/10.1007/s00466-003-0463-y`.

[81] E. Kuhl and P. Steinmann. Mass–and volume–specific views on thermodynamics for open systems. *Proceedings of the Royal Society of London. Series A: Mathematical, Physical and Engineering Sciences*, 459(2038):2547–2568, 2003. `https://doi.org/10.1098/rspa.2003.1119`.

[82] C. Le, T. Bruns, and D. Tortorelli. A gradient–based, parameter–free approach to shape optimization. *Computer Methods in Applied Mechanics and Engineering*, 200(9-12):985–996, 2011. `https://doi.org/10.1016/j.cma.2010.10.004`.

[83] C. Le Bellégo, G. Pijaudier-Cabot, B. Gérard, J.-F. Dubé, and L. Molez. Coupled Mechanical and Chemical Damage in Calcium Leached Cementitious Structures. *Journal of Engineering Mechanics*, 129(3):333–341, 2003. `https://doi.org/10.1061/(ASCE)0733-9399(2003)129:3(333)`.

[84] J. Liedmann and F.-J. Barthold. Exploration of Internal Response Sensitivities of Materially Nonlinear Structures. *PAMM*, 17(1):745–746, 2017. `https://doi.org/10.1002/pamm.201710340`.

[85] J. Liedmann and F.-J. Barthold. Variational sensitivity analysis of elastoplastic structures applied to optimal shape of specimens. *Structural and Multidisciplinary Optimization*, 61(6):2237–2251, 2020. `https://doi.org/10.1007/s00158-020-02492-9`.

[86] K. Loeffel and L. Anand. A chemo–thermo–mechanically coupled theory for elastic–viscoplastic deformation, diffusion, and volumetric swelling due to a chemical reaction. *International Journal of Plasticity*, 27(9):1409–1431, 2011. `https://doi.org/10.1016/j.ijplas.2011.04.001`.

[87] V. A. Lubarda and A. Hoger. On the mechanics of solids with a growing mass. *International Journal of Solids and Structures*, 39:4627–4664, 2002. `https://doi.org/10.1016/S0020-7683(02)00352-9`.

[88] Z. Lyu and J. R. Martins. Aerodynamic Shape Optimization of an Adaptive Morphing Trailing–Edge Wing. *Journal of Aircraft*, 52(6):1951–1970, 2015. `https://doi.org/10.2514/1.C033116`.

[89] R. Mahnken and E. Stein. Parameter identification for viscoplastic models based on analytical derivatives of a least–squares functional and stability investigations. *International Journal of Plasticity*, 12(4):451–479, 1996. `https://doi.org/10.1016/S0749-6419(95)00016-X`.

[90] R. Mahnken and E. Stein. A unified approach for parameter identification of inelastic material models in the frame of the finite element method. *Computer Methods in Applied Mechanics and Engineering*, 136(3–4):225–258, 1996. `https://doi.org/10.1016/0045-7825(96)00991-7`.

[91] D. Materna. *Structural and Sensitivity Analysis for the Primal and Dual Problems in the Physical and Material Spaces.* 2010.

[92] MathWorks. Global Optimization Toolbox: User's Guide (R2019b). `https://www.mathworks.com/help/releases/R2019b/pdf_doc/optim/optim_tb.pdf`, 2019.

[93] A. M. M.C.E. LVIII. The limits of economy of material in frame–structures. *The London, Edinburgh, and Dublin Philosophical Magazine and Journal of Science*, 8(47):589–597, 1904. `https://doi.org/10.1080/14786440409463229`.

[94] A. Menzel. Modelling of anisotropic growth in biological tissues. *Biomechanics and Modeling in Mechanobiology*, 3(3):147–171, 2005. `https://doi.org/10.1007/s10237-004-0047-6`.

[95] A. Menzel. A fibre reorientation model for orthotropic multiplicative growth. *Biomechanics and Modeling in Mechanobiology*, 6(5):303–320, 2007. `https://doi.org/10.1007/s10237-006-0061-y`.

[96] A. Menzel, M. Ekh, K. Runesson, and P. Steinmann. A framework for multiplicative elastoplasticity with kinematic hardening coupled to anisotropic damage. *International Journal of Plasticity*, 21(3):397–434, 2005. `https://doi.org/10.1016/j.ijplas.2003.12.006`.

[97] A. Menzel and E. Kuhl. Frontiers in growth and remodeling. *Mechanics Research Communications*, 42:1–14, 2012. `https://doi.org/10.1016/j.mechrescom.2012.02.007`.

[98] A. Menzel and P. Steinmann. A theoretical and computational framework for anisotropic continuum damage mechanics at large strains. *International Journal of Solids and Structures*, 38(52):9505–9523, 2001. `https://doi.org/10.1016/S0020-7683(01)00136-6`.

[99] T. Mori, M. Koga, Y. Hikosaka, T. Nonaka, F. Mishina, Y. Sakai, and J. Koizumi. Microbial Corrosion of Concrete Sewer Pipes, H_2S Production from Sediments and Determination of Corrosion Rate. *Water Science and Technology*, 23(7–9):1275–1282, 1991. `https://doi.org/10.2166/wst.1991.0579`.

[100] J. Nocedal and S. Wright. Numerical Optimization. In *Springer Series in Operations Research and Financial Engineering*. Springer, 2006. `https://doi.org/10.1007/978-0-387-40065-5`.

[101] L. Noël, P. Duysinx, and K. Maute. Level set topology optimization considering damage. *Structural and Multidisciplinary Optimization*, 56(4):737–753, 2017. `https://doi.org/10.1007/s00158-017-1724-2`.

[102] W. Noll. A new mathematical theory of simple materials. *Archive for Rational Mechanics and Analysis*, 48:1–50, 1972. `https://doi.org/10.1007/BF00253367`.

[103] S. A. Odhano, P. Pescetto, H. A. A. Awan, M. Hinkkanen, G. Pellegrino, and R. Bojoi. Parameter Identification and Self–Commissioning in AC Motor Drives: A Technology Status Review. *IEEE Transactions on Power Electronics*, 34(4):3603–3614, 2018. `http://dx.doi.org/https://doi.org/10.1109/TPEL.2018.2856589`.

[104] R. Ortigosa, J. Martínez-Frutos, A. J. Gil, and D. Herrero-Pérez. A new stabilisation approach for level-set based topology optimisation of hyperelastic materials. *Structural and Multidisciplinary Optimization*, 60(6):2343–2371, 2019. `https://doi.org/10.1007/s00158-019-02324-5`.

[105] ParaView. Paraview documentation. `https://docs.paraview.org/en/latest/`, 2020.

[106] C. Parker. The Corrosion of Concrete: 1. The Isolation of a Species of Bacterium Associated with the Corrosion of Concrete Exposed to Atmospheres Containing Hydrogen Sulphide. *Australian Journal of Experimental Biology & Medical Science*, 23(2), 1945. `https://doi.org/10.1038/icb.1945.13`.

[107] E. Perry, R. Balling, and M. Landon. A new morphing method for shape optimization. In *7th AIAA/USAF/NASA/ISSMO Symposium on Multidisciplinary Analysis and Optimization*, page 4907, 1998. `https://doi.org/10.2514/6.1998-4907`.

[108] J. E. Peter and R. P. Dwight. Numerical sensitivity analysis for aerodynamic optimization: A survey of approaches. *Computers & Fluids*, 39(3):373–391, 2010. `https://doi.org/10.1016/j.compfluid.2009.09.013`.

[109] V. N. Pokrovskii. *Thermodynamics of Complex Systems.* Institute of Physics Publishing, 2020.

[110] W. Prager. *Einführung in die Kontinuumsmechanik*, volume 20. Springer, 1961. `http://dx.doi.org/10.1007/978-3-0348-6848-8`.

[111] W. Prager. A note on discretized michell structures. *Computer Methods in Applied Mechanics and Engineering*, 3(3):349–355, 1974. `https://doi.org/10.1016/0045-7825(74)90019-X`.

[112] L. Qie, S. Jing, and R. Lian. Heaviside–Based Morphological Filters for Topology Optimization. In *IOP Conference Series: Materials Science and Engineering*, volume 472, page 012034, 2019.

[113] T. Ricken, N. Waschinsky, and D. Werner. Simulation of Steatosis Zonation in Liver Lobule–A Continuummechanical Bi–Scale, Tri–Phasic, Multi–Component Approach. In *Biomedical Technology. Lecture Notes in Applied and Computational Mechanics*, volume 84, pages 15–33. Springer, 2017. `https://doi.org/10.1007/978-3-319-59548-1_2`.

[114] E. K. Rodriguez, A. Hoger, and A. D. McCulloch. Stress–dependent finite growth in soft elastic tissues. *Journal of Biomechanics*, 27(4):455–467, 1994. `https://doi.org/10.1016/0021-9290(94)90021-3`.

[115] Y. Rousseau, I. MEN'SHOV, and Y. Nakamura. Morphing–Based Shape Optimization in Computational Fluid Dynamics. *Transactions of the Japan Society for Aeronautical and Space Sciences*, 50(167):41–47, 2007. `https://doi.org/10.2322/tjsass.50.41`.

[116] S. Sarkar, S. Mahadevan, J. Meeussen, H. van der Sloot, and D. Kosson. Numerical simulation of cementitious materials degradation under external sulfate attack. *Cement and Concrete Composites*, 32(3):241–252, 2010. `https://doi.org/10.1016/j.cemconcomp.2009.12.005`.

[117] S. Sarkar, S. Mahadevan, J. Meeussen, H. van der Sloot, and D. Kosson. Sensitivity Analysis of Damage in Cement Materials under Sulfate Attack and Calcium Leaching. *Journal of materials in civil engineering*, 24(4):430–440, 2012. `https://doi.org/10.1061/(ASCE)MT.1943-5533.0000407`.

[118] M. Scherer, R. Denzer, and P. Steinmann. A fictitious energy approach for shape optimization. *International Journal for Numerical Methods in Engineering*, 82(3):269–302, 2009. `https://doi.org/10.1002/nme.2764`.

[119] A. Schumacher. *Optimierung mechanischer Strukturen: Grundlagen und industrielle Anwendungen.* Springer, 2013. `https://doi.org/10.1007/978-3-642-34700-9`.

[120] D. F. Shanno. Conditioning of quasi-Newton methods for function minimization. *Mathematics of Computation*, 24(111):647–656, 1970. `https://doi.org/10.2307/2004840`.

[121] O. Sigmund and J. Petersson. Numerical instabilities in topology optimization: A survey on procedures dealing with checkerboards, mesh–dependencies and local minima. *Structural optimization*, 16(1):68–75, 1998. `https://doi.org/10.1007/BF01214002`.

[122] J. C. Simo and T. J. Hughes. *Computational Inelasticity*, volume 7. Springer, 2006. `https://doi.org/10.1007/b98904`.

[123] D. Simon. *Evolutionary Optimization Algorithms.* John Wiley & Sons, 2013.

[124] J. Sokolowski and J.-P. Zolésio. Introduction to Shape Optimization. In *Introduction to Shape Optimization*, pages 5–12. Springer, 1992. `https://doi.org/10.1007/978-3-642-58106-9`.

[125] L. Sprave and A. Menzel. A large strain gradient-enhanced ductile damage model: finite element formulation, experiment and parameter identification. *Acta Mechanica*, 231:5159–5192, 2020. `https://doi.org/10.1007/s00707-020-02786-5`.

[126] J. Stark and B. Wicht. *Zement und Kalk: Der Baustoff als Werkstoff.* Springer, 2013. `https://doi.org/10.1007/978-3-0348-8382-5`.

[127] M. L. Staten, S. J. Owen, S. M. Shontz, A. G. Salinger, and T. S. Coffey. A Comparison of Mesh Morphing Methods for 3D Shape Optimization. In *Proceedings of the 20th International Meshing Roundtable*, pages 293–311, 2010. `https://doi.org/10.1007/978-3-642-24734-7_16`.

[128] P. Steinke. *Finite–Elemente–Methode.* Springer, 2015. `https://doi.org/10.1007/978-3-642-53937-4`.

[129] E. Stora, B. Bary, Q.-C. He, E. Deville, and P. Montarnal. Modelling and simulations of the chemo–mechanical behaviour of leached cement–based materials: Interactions between damage and leaching. *Cement and concrete research*, 40(8):1226–1236, 2010. `https://doi.org/10.1016/j.cemconres.2010.04.002`.

[130] S. Suresh, S. B. Lindström, C.-J. Thore, B. Torstenfelt, and A. Klarbring. An Evolution–Based High–Cycle Fatigue Constraint in Topology Optimization. In *International Conference on Engineering Optimization*, pages 844–854. Springer, 2018. `https://doi.org/10.1007/978-3-319-97773-7_73`.

[131] B. Szabó et al. *Introduction to Finite Element Analysis: Formulation, Verification and Validation*, volume 35. John Wiley & Sons, 2011.

[132] D. W. Thompson. *On Growth and Form.* Canto. Cambridge University Press, 1992. `https://doi.org/10.1017/CBO9781107325852`.

[133] C. Truesdell and R. Toupin. The Classical Field Theories. In *Principles of Classical Mechanics and Field Theory / Prinzipien der Klassischen Mechanik und Feldtheorie*, pages 226–858. Springer, 1960. `https://doi.org/10.1007/978-3-642-45943-6_2`.

[134] F.-J. Ulm, J.-M. Torrenti, and F. Adenot. Chemoporoplasticity of Calcium Leaching in Concrete. *Journal of Engineering Mechanics*, 125(10):1200–1211, 1999. `https://doi.org/10.1061/(ASCE)0733-9399(1999)125:10(1200)`.

[135] F. Van Keulen, R. Haftka, and N. Kim. Review of options for structural design sensitivity analysis. Part 1: Linear systems. *Computer Methods in Applied Mechanics and Engineering*, 194(30–33):3213–3243, 2005. `https://doi.org/10.1016/j.cma.2005.02.002`.

[136] J. A. Vrugt and B. A. Robinson. Improved evolutionary optimization from genetically adaptive multimethod search. *Proceedings of the National Academy of Sciences*, 104(3):708–711, 2007. `https://doi.org/10.1073/pnas.0610471104`.

[137] D. Vucina, Z. Lozina, and I. Pehnec. A Compact Parameterization for Shape Optimization of Aerofoils. In *Proceedings of the World Congress on Engineering*, volume 1, pages 111–116, 2008.

[138] K. Wiechmann. *Theorie und Numerik zur Berechnung und Optimierung von Strukturen mit elastoplastischen Deformationen.* Forschungs- und Seminarberichte aus dem Institut

für Baumechanik und Numerische Mathematik, Universität Hannover. 2001.

[139] G. Wolberg. Image morphing: a survey. *The visual computer*, 14(8):360–372, 1998. `https://doi.org/10.1007/s003710050148`.

[140] P. Wriggers. *Nichtlineare Finite–Element–Methoden.* Springer, 2001. `https://doi.org/10.1007/978-3-642-56865-7`.

[141] B. S. Yıldız, A. R. Yıldız, E. İ. Albak, H. Abderazek, S. M. Sait, and S. Bureerat. Butterfly optimization algorithm for optimum shape design of automobile suspension components. *Materials Testing*, 62(4):365–370, 2020.

[142] B. G. Yoon and A. D. Belegundu. Iterative methods for design sensitivity analysis. *AIAA journal*, 26(11):1413–1415, 2012. `https://doi.org/10.2514/3.10058`.

[143] H. Yuan, P. Dangla, P. Chatellier, and T. Chaussadent. Degradation modelling of concrete submitted to sulfuric acid attack. *Cement and Concrete Research*, 53:267–277, 2013. `https://doi.org/10.1016/j.cemconres.2013.08.002`.

[144] H. Zhonghua, X. Chenzhou, L. Zhang, Y. Zhang, K. Zhang, and S. Wenping. Efficient aerodynamic shape optimization using variable–fidelity surrogate models and multilevel computational grids. *Chinese Journal of Aeronautics*, 33(1):31–47, 2020. `https://doi.org/10.1016/j.cja.2019.05.001`.

[145] O. C. Zienkiewicz, R. L. Taylor, and J. Z. Zhu. *The Finite Element Method: Its Basis and Fundamentals.* Elsevier, 2013. `https://doi.org/10.1016/C2009-0-24909-9`.

[146] Z. Zuo. *The coupled chemo–mechanical degradation of cement–based materials.* PhD thesis, School of Civil, Environmental and Mining Engineering, 2020. `http://hdl.handle.net/2440/125013`.